Development of a High Dynamic Velocity Range Processing Scheme for Time-Resolved Particle Image Velocimetry Measurements

by

R. Harris Haynes

A thesis submitted to the Graduate Faculty of
Auburn University
in partial fulfillment of the
requirements for the Degree of
Master of Science

Auburn, Alabama
August 3, 2013

Keywords: experimental fluids, time-resolved measurements, particle image velocimetry, high dynamic velocity range, supersonic jet flow

Approved by

Brian S. Thurow, Chair, Associate Professor of Aerospace Engineering
Roy J. Hartfield, Jr., Professor of Aerospace Engineering
Anwar Ahmed, Professor of Aerospace Engineering

Abstract

The development, validation, and demonstration of a novel computational procedure to supplementally process time-resolved particle image velocimetry (TR PIV) measurements are described. The motivation for such work stems from an experimental investigation to characterize the near-nozzle velocity field in a high-temperature, shock-containing jet. The computational procedure, termed dynamic evaluation via ordinary least squares (DEVOLS), offers substantial improvements over conventional processing methods for its ability to increase the dynamic velocity range. Unique to DEVOLS is an iterative validation scheme that enables a variable number of displacement results to be utilized in the determination of a single velocity vector. This approach is significant since it provides enhanced robustness in the presence of significant image noise. Validation of the procedure is provided through the use of temporally resolved, synthetically generated particle images simulating the fluid dynamics of a Hamel-Oseen vortex. Following such validation, the experimental investigation is described wherein TR PIV measurements were acquired for a flow field centered axially at the end of the jet potential core and radially along the lower half of the shear layer. For all cases the nozzle was operated at over-expanded conditions, and images were acquired through the combined use of a pulse burst laser and a high-speed, gated intensified CCD framing camera. Results achieved by the DEVOLS processing scheme are presented for both the experimental jet as well as a synthetic jet derived from computational fluid dynamics. Estimations of the measurement errors associated with these results are also given. Finally, steps for improving the quality of the experimental data as well as the analysis procedure are offered as suggestions for future investigations.

Acknowledgments

The work presented in this thesis would not have been possible without the help and support of many people. For this reason I would like to acknowledge and offer my sincerest gratitude to the following:

Dr. Brian Thurow, for his guidance and patience throughout my graduate education. The quality of my master's degree is directly attributable to his steadfast dedication to the development of graduate students, the advancement of academic research, and the betterment of aerospace engineering at Auburn University.

Dr. Roy Hartfield and Dr. Anwar Ahmed, for their invaluable contributions to my academic and research career. The advice and encouragement they provided on numerous course assignments, research projects, and conference publications proved paramount in the development of this thesis.

Dr. Nathan Murray and the aeroacoustics group at the Jamie Whitten National Center for Physical Acoustics (NCPA), for their time and assistance on my thesis work at the University of Mississippi. An acknowledgment is truly not enough for the hospitality and help they extended during my stay in Oxford, Mississippi.

My colleagues in the Advanced Laser Diagnostics Laboratory (ALDL), for the professional and progressive environment they created on a daily basis. The balance that existed between competitiveness and friendliness not only pushed me to work harder but also allowed me to enjoy my work more as I strove to accomplish my goals.

My father Randy Haynes, my mother Charlotte Haynes, my sister Hannah Nader, and my brother Hamp Haynes, for the unconditional love and unwavering support they have shown throughout my academic journey. I look forward to wherever the road leads next knowing I will always have them with me.

Table of Contents

List of Figures

List of Tables

List of Abbreviations

AJL	Anechoic Jet Laboratory
ALDL	Advanced Laser Diagnostics Laboratory
AMEC	Adaptive multi-step ensemble correlation
AMF PIV	Adaptive multi-frame PIV
AO	Acousto-optic
AOM	Acousto-optic modulator
ASE	Amplified spontaneous emission
C-D	Converging-diverging
CCD	Charge-coupled device
CFD	Computational fluid dynamics
CRAFT	Combustion Research and Flow Technology, Inc.
CW	Continuous-wave
DEVOLS	Dynamic evaluation via ordinary least squares
DVR	Dynamic velocity range
HDR	High dynamic velocity range
IA	Interrogation area
JDSU	JDS Uniphase Corporation
JNR	Jet Noise Reduction
KTP	Potassium titanyl phosphate ($KTiOPO_4$)
LES	Large eddy simulation
LSV	Laser speckle velocimetry

MAD	Median absolute deviation
MCP	Microchannel plate
MF PIV	Multi-frame PIV
MHz	Megahertz
MPS PIV	Multiple pulse separation PIV
NASA	National Aeronautics and Space Administration
NCPA	National Center for Physical Acoustics
Nd:YAG	Neodymium-doped yttrium aluminum garnet ($Nd:Y_3Al_5O_{12}$)
NPRO	Nonplanar ring oscillator
OLS	Ordinary least squares
ONR	Office of Naval Research
PIV	Particle image velocimetry
PTV	Particle tracking velocimetry
SAJF	Small Anechoic Jet Facility
SCFM	Standard cubic feet per minute
TR PIV	Time-resolved PIV

Symbols

a_∞	Ambient sound speed, m/s
D_{jet}	Nozzle exit diameter, m
I	Acoustic intensity, W/m^2
n	Multiplying coefficient
N_{vec}	Total vector number
p	Pressure, Pa
$\boldsymbol{r}$	Radiation vector, where $\boldsymbol{r} = (r_1, r_2, r_3)$, m
R^2	Coefficient of determination
S_n	Robust scale estimator

t	Time, s
T_0	Time period, s
T_{ij}	Lighthill stress tensor, Pa
$\boldsymbol{u}$	Velocity vector, where $\boldsymbol{u} = (u_1, u_2, u_3)$, m/s
u	Velocity component, m/s
$\tilde{u}$	Instantaneous (chapter 3) or median (chapter 6) velocity component, m/s
$\bar{u}$	Mean velocity component, m/s
v	Velocity component, m/s
$\boldsymbol{x}$	Position vector, where $\boldsymbol{x} = (x_1, x_2, x_3)$, m
x	Position component, m
$\boldsymbol{y}$	Position vector, where $\boldsymbol{y} = (y_1, y_2, y_3)$, m
y	Position component, m
z	Modified statistical z-score

Greek Symbols

δ_{ij}	Kronecker delta
δt	Interframe time, s
$\Delta\boldsymbol{x}$	Displacement magnitude, m
Δx	Displacement in the x-direction, m
Δy	Displacement in the y-direction, m
λ	Electromagnetic radiation wavelength, m
μ	Mean of a Gaussian distribution
ν	Kinematic viscosity, m^2/s
ρ	Density, kg/m^3
ρ_0	Total density, kg/m^3
ρ_{IA}	Particle density, particles per IA
ρ_{noise}	Noise density, noise per pixel

$\sigma_{\boldsymbol{u}}$	Minimum resolvable velocity, m/s
$\sigma_{\Delta \boldsymbol{x}}$	Minimum resolvable displacement, m
$\sigma^2_{\mu=0}$	Variance of a zero-mean, Gaussian distribution
τ	Pulse separation time, s (chapter 2); retarded time coefficient (chapter 3)
τ_{ij}	Viscous stress tensor, Pa

Subscripts

$i,\ j,\ k,\ l,\ n$	Tensor notation, where repeated indices are summed
max	Maximum resolvable parameter

Chapter 1

Introduction

Throughout history humans have been interested in studying the natural world, from describing their surroundings to analyzing how the universe behaves. In addition to recording physical appearances, characterizing the way matter moves has always been one of the most trivial yet significant observations a person can make. Such observations are important because understanding the motions of objects through space and time is critical to understanding the physics behind naturally occurring phenomena. If a pattern produced by or related to a physical process can be observed through visual inspection, then insight into that particular process can be greatly improved. This point is especially true in fluid-mechanical processes where motions can be complex in space as well as variable in time. Unfortunately most fluids are transparent media such that their motions remain hidden to the human eye. Thus methods must be developed to make fluid patterns visible, and these methods are known as flow-visualization techniques. At present the application of visualization techniques comprises an enormous field in engineering sciences and experimental physics for its role in understanding fluid-mechanical problems.

This introductory chapter is designed to provide an overview of flow visualization by considering the background and subsequent evolution of different visualization techniques. In addition to purely qualitative methods, modern techniques employing tracer particles are discussed that can provide quantitative measurements in highly complex flows. One particular method, known as particle image velocimetry (PIV), is described in detail for its widespread use in experimental investigations and the central role it played in the development of this thesis. The basic principles of PIV are presented along with key attributes

that render the method advantageous compared to probes and other single-point measurement techniques. The chapter is ultimately concluded by outlining the topics covered in the remainder of this thesis.

1.1 Early methods of flow visualization

Without considering the passive observations or artistic drawings of naturally occurring flows (many of which can be traced back to the days of Leonardo Da Vinci), some of the earliest recorded examples of how flow visualization has been utilized in experimental applications involve Ludwig Prandtl. In the early 1900s Prandtl conducted simple flow-visualization experiments using an open-surface water tunnel with suspended mica particles acting as fluid markers.[1] By forcing the mixture to flow past two-dimensional models, Prandtl studied the basic features present in both steady and unsteady flow environments. From the motions of the mica particles he was able to discern a variety of flow behaviors including separation as well as vorticity. Despite the ability to vary nearly all of the experimental parameters (flow speed, model geometry, angle of incidence, etc.) though, only qualitative descriptions were possible for any given flow.

In the time since these experiments were conducted, a number of other purely qualitative methods have been developed to help visualize fluid-mechanical processes. Similarly to Prandtl's technique, such methods generally involve introducing a foreign substance into a fluid and observing its subsequent motions. Dyes are most commonly used in liquid flows, whereas smoke[1] is primarily utilized in air. Regardless of the fluid, the substance chosen as the fluid marker is expected to fulfill a number of requirements including being neutrally buoyant, nontoxic, stable against mixing, and highly visible.[2] These criteria ensure that a technique remains non-intrusive and that fluid markers accurately depict the motions of a fluid. To better illustrate the variety of options available in experimental applications, several flow-visualization methods are presented for which air is the working fluid. These

[1]The term *smoke* as used in this thesis is not strictly limited to combustion products but also includes aerosols, mists, vapors, and tracer gases.

methods offer enormous diversity when it comes to analyzing different flow regimes and observing specific flow features. For the purposes of this thesis it should be noted that only applications involving the addition of fluid markers are considered. Thus techniques such as shadowgraph and schlieren photography are not discussed.

One of the oldest techniques to aid in the visualization of boundary layer motions is surface tufting. Tufts are small, inexpensive lengths of string that are frayed at one end and attached to a model's surface with the other. By tufting an entire model, insight into the behavior of boundary layer flows is possible depending on the manner in which tufts are blown. Regions of cross flow, reverse flow, and separated flow are indicated by the directions that tufts may point. Likewise steady and unsteady flow environments can be inferred from the varying motions of tufts with time. Despite these advantages, tufting is a tedious visualization procedure since the properties (dimensions, weight, stiffness, etc.) of tufts must be carefully chosen to minimize flow disturbances.

Surface oils provide an alternative method for visualizing boundary layer motions. In oil applications a solution is applied at several upstream locations such that downstream streaks illustrate the paths taken by different fluid elements. When applied correctly, surface oils are quite adept at detecting flow separation since the oil droplets do not penetrate separation boundaries. Because oils are also effective at marking transition points, they are used extensively to signalize transitions between laminar and turbulent boundary layers. One of the major disadvantages with surface oils is the preparation time required before each experimental application. Oil dabs must be positioned properly and with correct thicknesses if meaningful streaks are to be obtained. The clean-ups following oil investigations also present a major downside to the method.

Modern forms of flow visualization involve the use of smoke as a fluid marker. Unlike the previous two methods, smoke is primarily used to visualize patterns away from the surfaces of models. As such it is especially effective at detecting regions of vorticity and separated flow. In addition to being inexpensive to produce, the use of smoke is advantageous because

it can be injected into flows at a variety of locations including upstream of a test section or directly from a model's surface. Like all forms of flow visualization though, care must be taken to ensure that the addition of smoke does not alter the physics of the underlying flow.

Following advancements in laser technology, many state-of-the-art visualization techniques now incorporate laser sheets to further enhance the visibility of smoke or seed particles embedded in a flow. Lasers provide ideal light sources for particle illumination due to the high-intensity, short-duration pulses that can be achieved. In most applications a laser sheet is directed into a flow such that a planar region is illuminated. The features located within this plane are made visible by the light scattered from the particles. Obviously one drawback to such techniques is the restriction of a laser sheet to a single, two-dimensional plane. Even for methods allowing multiple planes in a flow to be illuminated, visualization of features moving orthogonally to these regions remains very limited.

Although methods like the ones described offer insight into the behavior of a variety of flows, a complete understanding of fluid-mechanical processes is not possible without complementary, quantitative information. The following section discusses several particle-based techniques that allow velocity-field data to be obtained. Through subsequent differentiation of the data, additional flow quantities can also be determined.

1.2 Quantitative visualization with tracer particles

Scientific and technical achievements over the last 50 years in optics, lasers, electronics, and computing have revolutionized the field of experimental fluid mechanics. In particular, advancements made in optical imaging, most notably the development of the charge-coupled device (CCD), have played a pivotal role in extracting velocity measurements from flows seeded with tracer particles. Similarly to the smoke-visualization technique described previously, these methods utilize laser sheets to illuminate planar regions of flow. By imaging the light scattered from particles within these regions, fluid displacements can be recorded

over specified time intervals. In this way velocity fields on the largest scales of a flow can be determined with sufficient spatial resolution to resolve microstructures on the smallest.[3]

Depending on the concentration of particles in the recorded images, three distinct methods have been established for characterizing and processing data. Techniques employing images with low particle densities are referred to as particle tracking velocimetry (PTV). In PTV, the average distance between particles in a single image is much larger than the average displacement of particles between subsequent images. Thus individual particles can easily be tracked from one image to the next, and local velocities can be determined from their measured displacements. Unfortunately only random samplings of velocity fields can be achieved in this way since measurements are not possible at positions lacking tracer particles. As a result, other techniques have been developed that provide increased spatial resolution.

Images containing intermediate particle densities are utilized in techniques known as particle image velocimetry. An intermediate density refers to the fact that the average particle spacing within each image is much smaller than the average particle displacement between subsequent images. Although individual particles can still be discerned, the same particles cannot be definitively identified in subsequent images due to their relative motions over the specified time intervals. For this reason statistical methods must be used to calculate the most probable displacements occurring at different image locations. Unlike PTV, the increased particle densities associated with PIV enable local velocity determinations to be made across all regions of a flow field.

Methods requiring even higher particle densities are known as laser speckle velocimetry (LSV). Although the processing steps for this technique are the same as PIV, the idea behind the two approaches is very different. In LSV, the concentration of seed particles is so high that individual particles cannot be distinguished in recorded images. Instead, a speckle pattern is observed based on the interference generated from the use of a coherent light source (laser) to illuminate a flow field. Local velocities are able to be determined by measuring the displacements of speckle patterns, rather than particles, between the images.

Due to undesired effects associated with such high particle densities though, LSV remains a less attractive option than PIV.

For its widespread popularity in experimental applications and the central role it played in the development of this thesis, a more comprehensive review of PIV is given in the following section. In addition to its underlying principles, particular emphasis is placed on the technology required to achieve most modern-day results.

1.3 Particle image velocimetry (PIV)

Particle image velocimetry refers to the variety of measurement techniques utilized in experimental fluid mechanics whereby instantaneous velocity fields are determined from the measured displacements of particles in a flow. The technique is based on the fundamental assumption that particles seeded in a flow accurately follow the motions of the fluid and thus are representative of the fluid's motions at any point in time. By recording images of the particles at two or more distinctly defined times and calculating their image displacements, the actual displacements of the particles can be determined. Using these displacements and the time increments between subsequent images, flow velocity can be evaluated directly from its fundamental definition, $\boldsymbol{u} = d\boldsymbol{x}/dt$. In this way PIV is able to make accurate, simultaneous measurements at multiple points over an entire flow field. This ability to combine the quantitative nature of single-point measurements with the whole-field nature of flow visualization makes the technique a unique and valuable tool for gaining insight into the behavior of a variety of flows.[4, 5]

The application of PIV is advantageous compared to probes and other single-point measurement techniques because it offers a way to non-intrusively obtain flow velocity fields. This characteristic is significant because it means PIV can be applied to a variety of flows that might easily be disturbed by the presence of measuring devices, such as transonic and supersonic flows with shocks as well as boundary layer flows. Furthermore, the whole-field nature of the technique and the high spatial resolution it provides allow the detection of

spatial structures even in the most unsteady flow environments. The high spatial resolution is a direct result of the fact that particle motions can be effectively frozen at two or more distinctly defined times by capturing instantaneous particle images. As long as the particles follow the motions of fluid elements to within some acceptable degree of error, flow velocity information can be extracted from the images albeit with limited temporal resolution in most cases. In describing the basic requirements for PIV applications, a simple system similar to the one shown in figure 1.1 is considered.

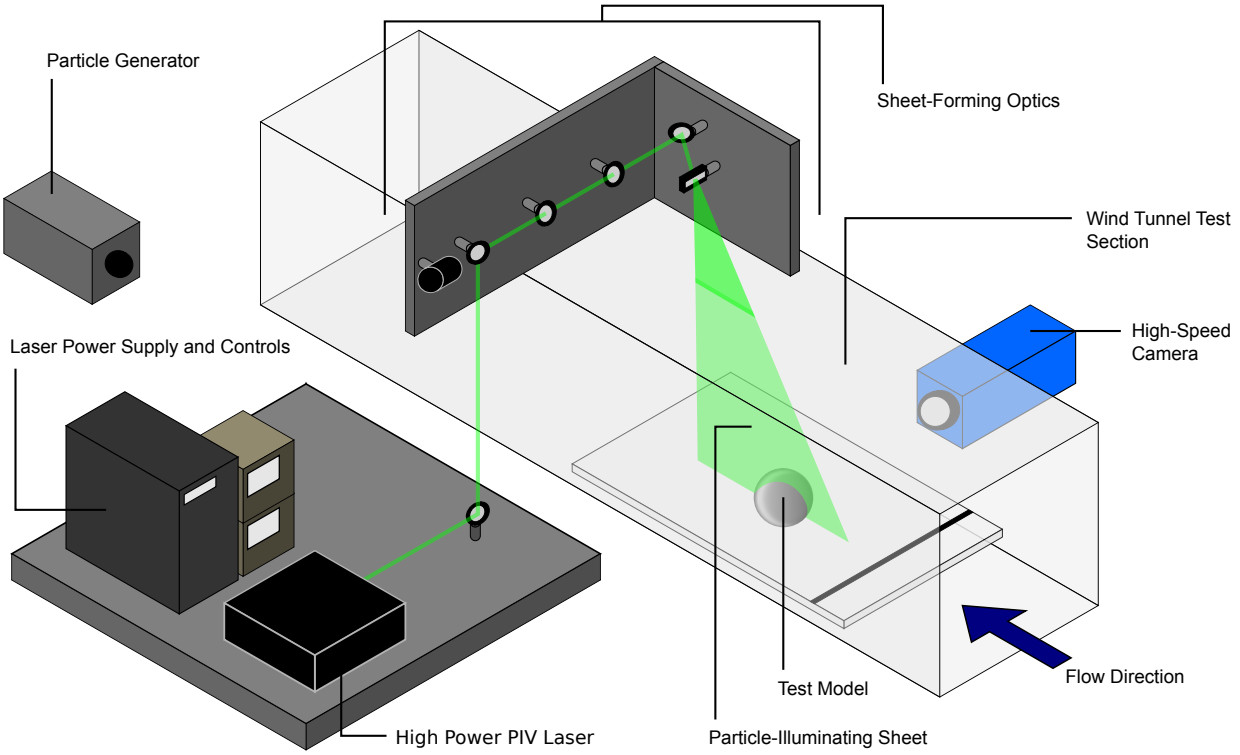

Figure 1.1: Standard particle image velocimetry (PIV) setup consisting of a high-power laser and a high-speed camera.

The selection of tracer particles represents one of the most important aspects in PIV analyses since the desired velocity fields are entirely dependent on how well these particles emulate a given flow.[6] To ensure that particles faithfully follow the motions of a fluid, particle sizes as small as possible are typically chosen. This characteristic is especially true for applications involving high-speed gas flows. As a result, high-power light sources play an essential role in most PIV setups in order to well expose a recording device with scattered

light from the particles. In practice, the physical plane in a fluid where measurements are desired is illuminated by at least two light pulses of limited duration to avoid image blurring or streaking. Lasers are almost always employed for this reason and because they allow subsequent illuminations to be made with the same, constant energy. As may be apparent, in most applications a compromise has to be made between utilizing large particles to more effectively scatter light and using small particles to more accurately trace the motions of fluid elements.

In addition to high-power light sources, high-speed imaging devices are also required in PIV applications due to the necessary rates at which particle images must be recorded. In general, time delays between subsequent images must be long enough to discern particle displacements with high resolution but short enough to avoid significant, out-of-plane particle motion. Although no metric exists for determining specific time delays in various PIV analyses, a widely accepted rule, known as the *one-quarter rule*, suggests that fewer than one-quarter of the particles should fail to produce two images.[7] It should be noted that although an analytical justification exists for this rule, such detail is unimportant in the context of this introduction. Instead, the significance in mentioning this rule resides in the fact that time delays between subsequent images must decrease as flow speed increases if particle motions and thus flow velocities are to be accurately obtained. For these reasons the temporal resolution in most PIV applications depends on and is also limited by the present capabilities of high-speed lasers and cameras. Further discussion regarding the general theory and design rules of PIV is given by Keane and Adrian [8, 9, 10].

1.4 Thesis overview

The aim of the work described in this thesis is the development and application of a unique processing technique that increases the dynamic velocity range of time-resolved particle image velocimetry measurements. For such measurements the dynamic velocity range is determined by the ratio of maximum to minimum resolvable particle displacements

that exists between images. By increasing this range, substantial improvements can be made in terms of spatial resolution and measurement accuracy over conventional PIV results. Consequently this technique is ideally suited for flows containing a wide velocity range, such as high-speed jets.

The following chapter explains the significance of temporal resolution in relation to PIV measurements. Computational procedures capable of increasing the dynamic velocity range of such measurements are presented along with applications that successfully demonstrate the concept. Chapter 3 transitions to the work actually performed in this thesis. As such it introduces the problem of jet noise and discusses the necessary resources for studying it with high fidelity. Included are detailed descriptions of the experimental facility where measurements were performed as well as the unique PIV system that was used. Chapter 4 proposes a novel, high dynamic velocity range processing scheme designed specifically for the experiments of interest. Validation for the approach is provided through the use of temporally resolved, synthetically generated particle images. Chapters 5 and 6 contain the results of the experimental investigation and the corresponding error analysis, respectively. Concluding remarks are offered in chapter 7 as suggestions for future investigations.

Chapter 2

High Dynamic Velocity Range PIV

In addition to the lack of three-dimensionality available in PIV, the limited dynamic velocity range represents one of the largest problems currently plaguing the technique.[11] Although several methods have been developed to extend this range, flows containing a wide velocity distribution still present a major challenge to PIV algorithms. Because particle displacements in these flows can differ drastically depending on the local velocity, computational procedures must be designed to account for temporal variations in particle-image patterns. This chapter describes a few such approaches that aim to increase the dynamic velocity range of time-resolved PIV measurements. The need for temporal resolution in acquired image sequences is explained first, and various strategies for evaluating these sequences are then presented. Notable techniques included in the discussion are multi-frame PIV, adaptive multi-frame PIV, and adaptive multi-step ensemble correlation. A method known as multiple pulse separation PIV is also mentioned for its ability to improve the dynamic velocity range, however this technique can only provide time-averaged results.

2.1 Temporal resolution in PIV applications

Because of the high spatial resolution inherent in PIV images, information about a number of useful fluid-mechanical properties can be obtained. Such properties include but are not limited to vorticity, rate of strain, and viscous dissipation.[12] Despite providing a means of acquiring instantaneous spatial derivatives though, until recently it has not been practical to use PIV to measure fluid velocity time derivatives except in low-speed flows. This lack of temporal resolution is unfortunate because velocity time derivatives, or accelerations, are a fundamental component in fluid mechanics since they represent the sum of all forces

present within a flow. Thus the need to accurately measure instantaneous and full-field accelerations has resulted in the development of several ways to acquire PIV measurements with significantly greater temporal resolution than has previously been possible. For these reasons time-resolved PIV, or TR PIV, has become an increasingly useful measurement technique in experimental fluid mechanics.

Unlike advanced forms of PIV that involve complex setups and tedious calibration procedures, TR PIV applications in general do not require any supplementary components beyond what is necessary to achieve standard PIV results. Furthermore, the only additional image and data processing steps are those needed to compute the fluid velocity time derivatives or acceleration fields. On these grounds TR PIV is for all purposes an extension or specialized case of conventional PIV and can therefore be theoretically utilized in all flows where the standard PIV technique is applicable. For completion it should be noted that TR PIV measurements can also be made in conjunction with advanced PIV methods, but such topics are beyond the scope of this thesis. More specifics on the basic requirements for TR PIV applications are given in the paragraph below.

As mentioned, frame rates have traditionally been too low to achieve time-resolved measurements except in liquid and low-speed aerodynamic flows. Continued development in high-speed laser and camera technology has recently, however, enabled PIV data to be acquired with greater temporal resolution than ever before. Such developments have especially benefited applications in unsteady flow environments including turbulent and higher-Mach-number flow regimes. For all cases though, measurements of fluid velocity time derivatives are desirable because they reflect the sum of all forces, namely pressure and viscous, present within a flow. This relationship between forces and the temporal derivatives of flow velocity can easily be seen in the incompressible form of the Navier-Stokes equation shown below.

$$\frac{\partial u_i}{\partial t} = -u_j \frac{\partial u_i}{\partial x_j} - \frac{1}{\rho}\frac{\partial p}{\partial x_i} + \nu \frac{\partial^2 u_i}{\partial x_j \partial x_j} \tag{2.1}$$

Presented in this way, equation 2.1 relates the local rate of change of velocity to the convective

acceleration and the net pressure and viscous forces, respectively.[13] By combining the acceleration terms into a single value as follows,

$$\frac{Du_i}{Dt} \equiv \frac{\partial u_i}{\partial t} + u_j \frac{\partial u_i}{\partial x_j} \tag{2.2}$$

the fluid-particle acceleration can be determined. This value, represented as Du_i/Dt in equation 2.2, is typically referred to as the Lagrangian acceleration and is a desirable quantity in fluid mechanics since it provides a means of directly measuring the net pressure and viscous forces.[14] Reports on Lagrangian accelerations are sparse, however, because the extraction of gradients in the convective term contributes significantly to the error.[15] Nevertheless, from these definitions it is apparent that acceleration fields can be experimentally evaluated from PIV by using subsequently measured velocity fields with finite-difference methods. It should be noted, however, that this approach is only valid if the acquisition rate of velocity fields is compatible with the characteristic time scales of a flow. Consequently in order to accurately determine acceleration fields, particularly ones pertaining to high-speed flows, temporally resolved measurements significantly greater than what conventional PIV offers are necessary.

2.2 Techniques for increasing the dynamic velocity range

From the previous section it should be clear that the current interest in TR PIV arises from the need to obtain local accelerations and thus instantaneous pressure fields in unsteady flow environments. Accurate measurements of velocity time derivatives are required in order to evaluate the Lagrangian accelerations of fluid particles and in turn integrate the spatial field of the pressure gradient.[16] For the experiments of interest and other applications involving aeroacoustics, the accuracy of such measurements is even more important since double temporal derivatives are required to use the PIV data with corresponding aeroacoustic analogies.[17] Specific information regarding the aeroacoustic motivation behind this thesis is

given in the following chapter. Nevertheless, the takeaway point from this discussion is that reliable temporal derivatives must be achieved in PIV measurements if accurate, subsequent flow quantities are to be obtained.

One approach for improving the accuracy of PIV results is to increase the dynamic velocity range of the data. According to Adrian [18], this range is defined as the ratio of the maximum velocity to the minimum resolvable velocity. Likewise it can also be expressed in terms of the maximum and minimum resolvable particle displacements. Mathematically these relationships can be written as follows.

$$\text{DVR} \equiv \frac{\boldsymbol{u}_{max}}{\sigma_{\boldsymbol{u}}} = \frac{[\,\Delta\boldsymbol{x}_{max} \,/\, \delta t\,]}{[\,\sigma_{\Delta\boldsymbol{x}} \,/\, \delta t\,]} = \frac{\Delta\boldsymbol{x}_{max}}{\sigma_{\Delta\boldsymbol{x}}} \tag{2.3}$$

In equation 2.3, the dynamic velocity range is represented by DVR, and the maximum and minimum resolvable particle displacements are shown as $\Delta\boldsymbol{x}_{max}$ and $\sigma_{\Delta\boldsymbol{x}}$, respectively. It should be noted that only velocity magnitudes are assumed in this definition. Thus if negative velocities occur, then $\boldsymbol{u}_{max}$ is defined as the larger of the maximum positive velocity or the maximum magnitude of the negative velocity. At present a DVR of approximately 200:1 is the standard for two-dimensional PIV measurements.[19] In applications where ranges begin to exceed this value, the accuracy of vectors in the low-velocity regions starts to deteriorate. For this reason data acquisition rates are generally chosen such that only flow phenomena of interest are properly sampled. Unfortunately this mode of imaging means that vectors calculated in other flow regimes have the potential of being highly inaccurate. Consequently high dynamic velocity range (HDR) techniques have been developed to improve the evaluation of time-resolved image sequences.

2.2.1 Multi-frame PIV

Although increasing the time interval between subsequent frames is not a preferred method for improving the DVR, a few studies have managed to achieve satisfactory results

by applying this approach locally. The problem with using larger temporal separations is the reduction one experiences in the signal-to-noise ratio. A greater pulse separation leads to increased losses between in-plane and out-of-plane particle pairs. To overcome this limitation, procedures known as multi-frame (MF) PIV have been developed that utilize temporally resolved, single-frame image sequences to locally optimize particle-image displacements. Several variations of this approach are described in the paragraphs below.

One of the first MF methods designed to improve the performance of TR PIV is suggested by Fincham and Delerce [20]. The approach revolves around a hierarchical processing scheme that considers the effects of local fluid deformation calculated during successive passes. Critical to the implementation of this technique is the ability to transform a discrete image into a continuous function that can be deformed and resampled at arbitrary resolution. Following an initial correlation of two frames with a temporal separation of δt, displacement estimates can be made for the deformation and correlation of frames separated by larger time intervals ($2\,\delta t$, $3\,\delta t$, etc.). Considering a sequence with only three images, frames one and two are correlated in an initial pass such that the results can assist with the processing of frames one and three. By utilizing larger time intervals in subsequent correlations, average pixel displacements can be increased and thus the overall DVR enhanced.

Pereira et al. [21] present an alternative method for dealing with temporally resolved image sequences. Termed adaptive multi-frame (AMF) PIV, the technique aims at the minimization of errors found in low-velocity regions by adjusting locally and dynamically the interframe time between particle-image pairs. As before, the algorithm operates strictly on a local basis such that a constant level of accuracy is achieved for all velocity ranges. AMF PIV differs from the previous approach, however, in that it allows an initial correlation to be performed on a central pair. Thus for an image pair located near the middle of a sequence, subsequent pairs can be selected forward or backward in time (i.e., forward or backward in the same sequence) without affecting the algorithm. By not restricting the procedure to only forward-type correlations, increased accuracy can be attained through the use of centralized

processing schemes. Compared to conventional PIV, AMF PIV has achieved superior results in both synthetic and real flow cases, especially those containing a wide velocity range.

Hain and Kähler [22] propose a further development of this technique by taking higher-order effects into account. Using additional constraints to validate each local displacement measurement, an optimum temporal separation can be chosen at each vector location that minimizes the relative measurement error. Similarly as before, a final displacement field is obtained by combining the optimum correlation results. To ensure that all correlations correspond to the same displacement field, only images symmetrically straddling a shared, central frame are considered. The actual processing scheme is performed hierarchically as was first outlined in Kähler [23]. For a sequence containing images with the following temporal distribution $\{t-n\,\delta t,\, \ldots,\, t-2\,\delta t,\, t-\delta t,\, t,\, t+\delta t,\, t+2\,\delta t,\, \ldots,\, t+n\,\delta t\}$, an initial correlation is made between frames $t-\delta t$ and $t+\delta t$. Based on the characteristics of this initial evaluation, optimum particle displacements are estimated across the full DVR of a flow. Using these estimations and considering the effects due to in-plane and out-of-plane loss-of-pairs, velocity gradients, and local accelerations, optimum temporal separations are calculated for any number of specific regions of interest (interrogation areas or IA). Local correlations are then performed at each region using the image pair providing the optimum separation. Because a final vector field is constructed entirely from local evaluations, the minimum possible measurement error is achieved.

2.2.2 Adaptive multi-step ensemble correlation

A final method designed to enhance the precision and robustness of TR PIV measurements is introduced by Sciacchitano et al. [24]. The technique, referred to as adaptive multi-step ensemble correlation (AMEC), includes aspects of the MF approaches described previously as well as a method known as correlation ensemble averaging [25]. Without going into detail, correlation ensemble averaging is a procedure by which correlation functions computed at different temporal separations are averaged to build an ensemble-averaged map

with higher signal-to-noise ratio. This approach is desirable in PIV measurements because the information built from larger temporal separations allows higher measurement precision to be achieved. Moreover, the correlation averaging obtained from shorter temporal separations contributes to the robustness of the processing. For input the AMEC algorithm requires a short series of recordings separated by a constant time interval. Optimum temporal separations are then locally evaluated based on error-minimization criteria. Unique to this approach is the ability to match correlation planes using homothetic transformations. This step is necessary to linearly combine the correlation signals acquired at different temporal spacings. From comparisons with state-of-the-art PIV processing techniques, the AMEC method has proven to increase the reliability of measured vectors and to significantly reduce both precision and acceleration errors.

2.2.3 Multiple pulse separation PIV

Until recently it has not been practical to use MF methods in high-speed flows due to limitations imposed by laser and camera repetition rates. To avoid the use of excessive temporal separations in TR PIV applications, a multiple pulse separation (MPS) technique is proposed by Persoons and O'Donovan [26]. In this technique a series of double-frame images with different pulse separations is recorded such that a sequence with the following temporal distribution is obtained $\{[t,\ t + n_1\tau],\ [t + \delta t,\ t + \delta t + n_2\tau],\ ...\}$. The interframe time ($\delta t$) remains constant, whereas the pulse separation time (τ) grows according to a monotonically increasing multiplier (n_1, n_2, etc.). Once a desired sequence has been acquired, vector fields for all pulse separation values are evaluated using standard PIV algorithms. A pulse separation optimality criterion is then applied locally to compute a final displacement field. Because the results encompass multiple pulse separation values, the DVR is dramatically increased compared to velocity fields achieved by conventional methods. Despite this improvement, the MPS technique applies only to mean flow and subsequent turbulence quantities since it is unable to provide temporally resolved results.

Chapter 3

Experimental Overview

The work presented in this thesis is part of a larger, collaborative effort to investigate the turbulence associated with jet noise generation. In addition to PIV, synchronous near-field and far-field acoustic measurements were obtained to better quantify the noise generated by supersonic flows emanating from converging-diverging (C-D) nozzles. Such noise is associated with typical variable-area nozzles found on modern, high-performance, military aircrafts and consequently is of interest due to concerns over noise-induced hearing loss as well as degraded operational awareness. The cumulative data from these studies provides temporally resolved, synchronous characterization of the near-nozzle velocity field, the hydrodynamic pressure field, and the acoustic far field. By studying the noise-generating features of high-temperature, shock-containing jets using several measurement techniques, the hope is that a better understanding of near-nozzle flow conditions and their impacts on jet noise radiation can be obtained.

The following sections provide a comprehensive overview of the experimental research that was performed for this thesis, namely the acquisition and processing of TR PIV data for the near-nozzle flow field encompassing the collapse of the jet potential core (descriptions and preliminary results for the near-field and far-field acoustic investigations are available in Murray et al. [27]). An initial section supplies the aeroacoustic motivation for the work. The problem of jet noise is introduced along with the theoretical justification for acquiring synchronized measurements. In addition to such background information, accompanying sections are given that depict the experimental setup and the corresponding, operational parameters. The specialized facility where measurements were performed is described in

conjunction with the unique PIV system that was used. Results obtained from the experimental investigation are presented in chapter 5.

3.1 Jet noise background

Despite over 60 years of research in jet aeroacoustics, a limited understanding persists in regards to turbulent jets and the mechanisms responsible for turbulent noise generation. Not only has a universal definition of turbulent noise sources eluded theorists, but what constitutes a source mechanism and how such mechanisms can be rendered less efficient (as it pertains to sound generation) remain unknown. From an experimental standpoint attempts to model, measure, and control turbulent jets have been thwarted by instrumental constraints. More often than not, such constraints have resulted from inadequate sensitivities and insufficient frequencies to accurately capture or noticeably influence phenomena of interest. Until a better understanding of source mechanisms is achieved, efforts designed to eliminate or even minimize jet noise radiation will continue to be at the forefront of aeroacoustic research.

For the purposes of this thesis in connection with the Jet Noise Reduction (JNR) program of the Office of Naval Research (ONR), jet noise corresponds to the high-amplitude sound generated by air-breathing propulsion systems, namely low-bypass turbine engines. At present it represents one of the most acute noise sources for the Department of Navy and has been linked to adverse biological, mechanical, and environmental effects. Such effects include but are not limited to the noise-induced hearing loss of Navy personnel, the structural degradation of Naval airframes, and the restriction of maintenance, testing, and training schedules due to noise pollution in communities surrounding Naval installations.[28] To counteract these issues and combat the problem of jet noise, attempts are being made to realize and establish jet noise reduction technologies through coordinated science efforts. The multitude of experiments undertaken in this investigation represents one such effort.

As mentioned, while the research presented in this thesis is solely concerned with the characterization of the near-nozzle velocity field, the overall project goal is to obtain a benchmark-quality data set that includes time-dependent, velocity-field measurements along with synchronized near-field and far-field pressure signals. The theoretical justification and motivation for such work is given by the analysis below. It should be noted that the format of this procedure is similar to that contained in the technical proposal by Murray et al. [28].

In the 1950s Lighthill [29, 30] developed an expression to describe the sound generated aerodynamically by subtracting the divergence of the momentum equation from the time derivative of the continuity equation.

$$\frac{\partial^2 \rho}{\partial t^2} - a_\infty^2 \frac{\partial^2 \rho}{\partial x_i \partial x_i} = \frac{\partial^2 T_{ij}}{\partial x_i \partial x_j} \tag{3.1}$$

The source term he obtained, generally referred to as the Lighthill stress tensor, is given in the expanded form below.

$$T_{ij} = \rho \tilde{u}_i \tilde{u}_j + (p - \rho a_\infty^2)\delta_{ij} - \tau_{ij} \tag{3.2}$$

Here, ρ is the density, $\tilde{u_i}$ and $\tilde{u_j}$ are instantaneous components of velocity, p is the pressure, a_∞ is the ambient speed of sound, δ_{ij} is the *Kronecker delta* (1 for $i = j$ and 0 for $i \neq j$), and τ_{ij} is the viscous stress tensor (where repeated indices are summed over). To calculate the sound generated aerodynamically, a conventional method involves solving equation 3.1 for an analytical solution to the density field. For unbounded flow a solution with the following form can be achieved.

$$\rho(\boldsymbol{y}, t) \approx \frac{1}{4\pi a_\infty^2} \iiint_V \frac{1}{\mid \boldsymbol{y} - \boldsymbol{x} \mid} \frac{\partial^2 T_{ij}(\boldsymbol{x}, \tau)}{\partial x_i \partial x_j} \, d\boldsymbol{x} \tag{3.3}$$

In equation 3.3, the far-field density is determined by a volume integral over the double divergence of the Lighthill stress tensor. Not to be confused with the viscous stress tensor

mentioned previously, the symbol τ is a retarded time coefficient associated with the propagation of sound. The terms $\boldsymbol{x}$ and $\boldsymbol{y}$ correspond to the position of the acoustic source and the position of the observation point, respectively. By rewriting this equation using a directional cosine (x_i/x), a more useful formula can be obtained.

$$\rho(\boldsymbol{y}, t) \approx \frac{1}{4\pi a_\infty^4} \frac{x_i x_j}{x^3} \iiint_V \frac{\partial^2 T_{ij}(\boldsymbol{x}, \tau)}{\partial \tau^2} \, d\boldsymbol{x} \tag{3.4}$$

Because direct measurements of the density field are not practical at this time, experimental applications are typically concerned with evaluating the acoustic intensity. Considering the solution below, the intensity field can be expressed as a function of the far-field density.

$$I(\boldsymbol{y}) = \frac{a_\infty^3}{\rho_0} \langle \rho(\boldsymbol{y}, t)^2 \rangle \tag{3.5}$$

By substituting the density field from equation 3.4 into equation 3.5, the far-field acoustic intensity can be rewritten as follows.

$$I(\boldsymbol{y}) = \frac{x_i x_j x_k x_l}{16\pi^2 a_\infty^5 \rho_0 x^4} \int_V \int_{V'} \left\langle \frac{\partial^2 T_{ij}}{\partial \tau^2} \frac{\partial^2 T'_{kl}}{\partial \tau^2} \right\rangle d\boldsymbol{x} \, d\boldsymbol{x}' \tag{3.6}$$

The first and second terms inside the brackets are evaluated at $(\boldsymbol{x}, \tau)$ and $(\boldsymbol{x}', \tau')$, respectively, which are suitable retarded times from the observation point. By following the analysis detailed in several works [31, 32, 33] and applying various assumptions including homogeneity of the turbulence field, a modified version of the preceding expression can be obtained.

$$I(\boldsymbol{y}) = \frac{x_i x_j x_k x_l}{16\pi^2 a_\infty^5 \rho_0 x^4} \int_V \frac{\partial^4}{\partial \tau^4} \langle T_{ij} T'_{kl} \rangle \, d\boldsymbol{r} \tag{3.7}$$

In this form it is apparent that the far-field intensity depends on space-time correlations of the Lighthill stress tensor. If one assumes that the only important term in this tensor is the

first (i.e., $T_{ij} = \rho\tilde{u}_i\tilde{u}_j$), then equation 3.7 can be simplified to the following.

$$I(\boldsymbol{y}) = \frac{x_i x_j x_k x_l}{16\pi^2 a_\infty^5 \rho_0 x^4} \int_V \frac{\partial^4}{\partial\tau^4} \langle \tilde{u}_i \tilde{u}_j \tilde{u}'_k \tilde{u}'_l \rangle \, d\boldsymbol{r} \tag{3.8}$$

The bracketed term is of significant importance to the work in this thesis since it comprises fourth-order, two-point, space-time correlations of the velocity field.[33] Under the assumption of inviscid flow, the near-field pressure can also be examined using velocity data.

$$\frac{\partial p}{\partial x_i} = -\rho \left(\frac{\partial \tilde{u}_i}{\partial t} + \tilde{u}_j \frac{\partial \tilde{u}_i}{\partial x_j} \right) \tag{3.9}$$

As both the far-field intensity and the near-field pressure can be derived from velocity terms, time-resolved measurements of the near-nozzle velocity field performed synchronously with the near-field and far-field pressures offer valuable insight. To date, no such measurements are known to exist for high-temperature, supersonic, shock-containing jets. The following sections describe in great detail the experimental arrangement that enabled such velocity-field measurements to be obtained. Future work will utilize these measurements to characterize the space-time correlations presented in equation 3.8.

3.2 Anechoic Jet Laboratory

Experiments were conducted in the Anechoic Jet Laboratory (AJL) at the Jamie Whitten National Center for Physical Acoustics (NCPA) on the campus of the University of Mississippi. The AJL is a small facility purpose built for the study of high-temperature, supersonic jet noise.[34] To overcome the shortcomings of previous facilities, specifically the NASA Langley Small Anechoic Jet Facility (SAJF), the AJL is designed to allow for aspiration of the test chamber. Using a 10,000 standard cubic feet per minute (SCFM) fan, ambient air can be pulled through the facility at speeds of approximately 1 ft/s (measured without jet flow in the anechoic section). Because of upstream and downstream stagnation

chambers, the air actually percolates into the 19-by-20-by-8 ft test chamber (measured between the wedge tips) through 50% porosity sliding panels in the upstream and downstream walls. This mode of operation results in a very even temperature distribution throughout the room while maintaining an acoustically anechoic environment. By aspirating the entire chamber, problems associated with localized heating can be minimized along with adverse effects on the jet entrainment due to the enclosed space. Figure 3.1 provides a view of the test chamber in the AJL with various measurement systems in place.

Figure 3.1: Experimental setup in the test chamber of the Anechoic Jet Laboratory (AJL).

The jet rig visible in figure 3.1 and shown specifically in figure 3.2 is supplied air from an 1100 hp Ingersoll-Rand Centac compressor through a desiccant dryer system. A maximum volumetric flow rate of 5000 SCFM of dry ($-40°$F) air at 125 psia enables continuous

operation of the facility at desired test conditions. Control valves operated in a closed-loop system allow the exit Mach number to be maintained within 1% of a specified value. Heat can be added to the flow through the use of a gaseous propane burner system as shown in figure 3.2(b). The actual propane combustor is housed well upstream of the nozzle assembly and is followed by a ceramic flow straightener and settling chamber. Although multiple nozzle assemblies exist for this system, only the configuration shown in the schematic that includes the centerbody section was utilized for the work in this thesis.

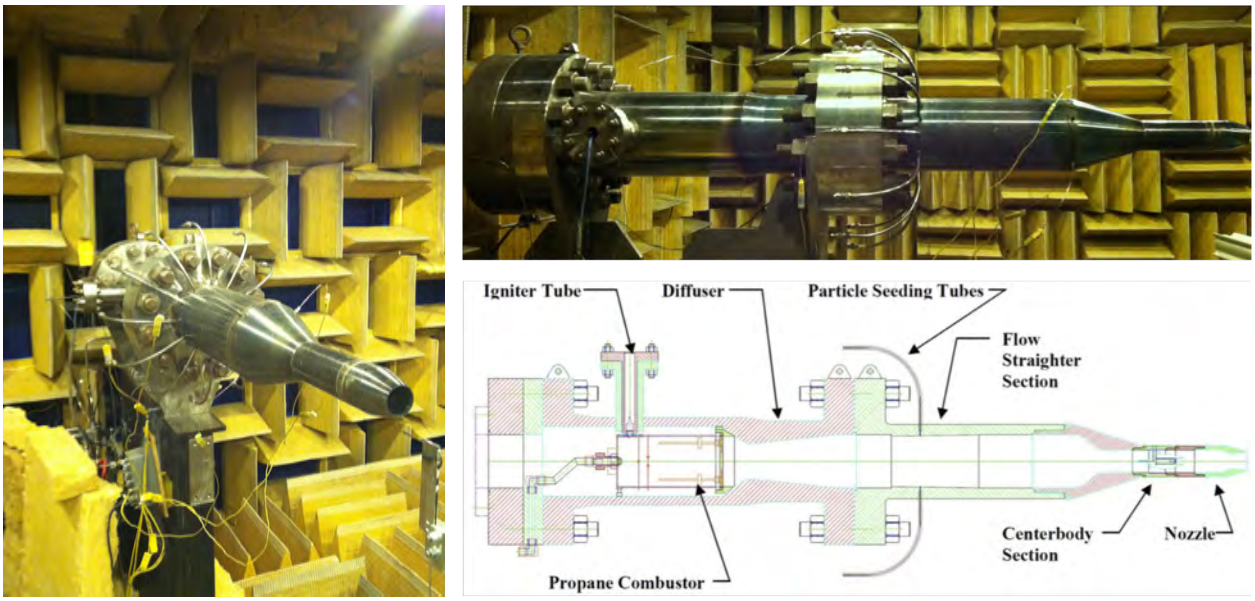

(a) Jet rig in the AJL

(b) Jet rig schematic (Murray et al. [27])

Figure 3.2: AJL propane burner system and nozzle assembly.

3.3 Megahertz frame rate PIV system

A megahertz (MHz) frame rate PIV system was developed through the combined use of a pulse burst laser and a high-speed, gated intensified CCD framing camera. For its ability to acquire sequences of 16 images at MHz frame rates, the system allowed temporally resolved velocity-field measurements to be obtained for a high-temperature, supersonic jet. Each component of the unique PIV system is explained in detail along with the experimental setup. Although this system was synchronized with both near-field and far-field pressure measurement devices, only the PIV system is considered for the purposes of this thesis.

3.3.1 Pulse burst laser

As has been described in previous publications [35, 36, 37], a pulse burst laser system developed at Auburn University allows a specified number of high-energy, MHz rate laser pulses to be formed for a given burst of low-energy, short-duration pulses. It should be noted that several upgrades have been made to this system since these publications including a new JDSU NPRO 126 continuous-wave (CW) Nd:YAG laser to enhance the pulse-to-pulse stability of each burst. This component in particular results in more consistent illuminations between images and thus better results in the PIV cross-correlations. In addition to the CW laser, three supplementary amplification stages have been incorporated into the system (for a total of six amplification stages) to increase the overall energy available for each burst and consequently each individual laser pulse. A schematic of the upgraded pulse burst laser system is shown in figure 3.3.

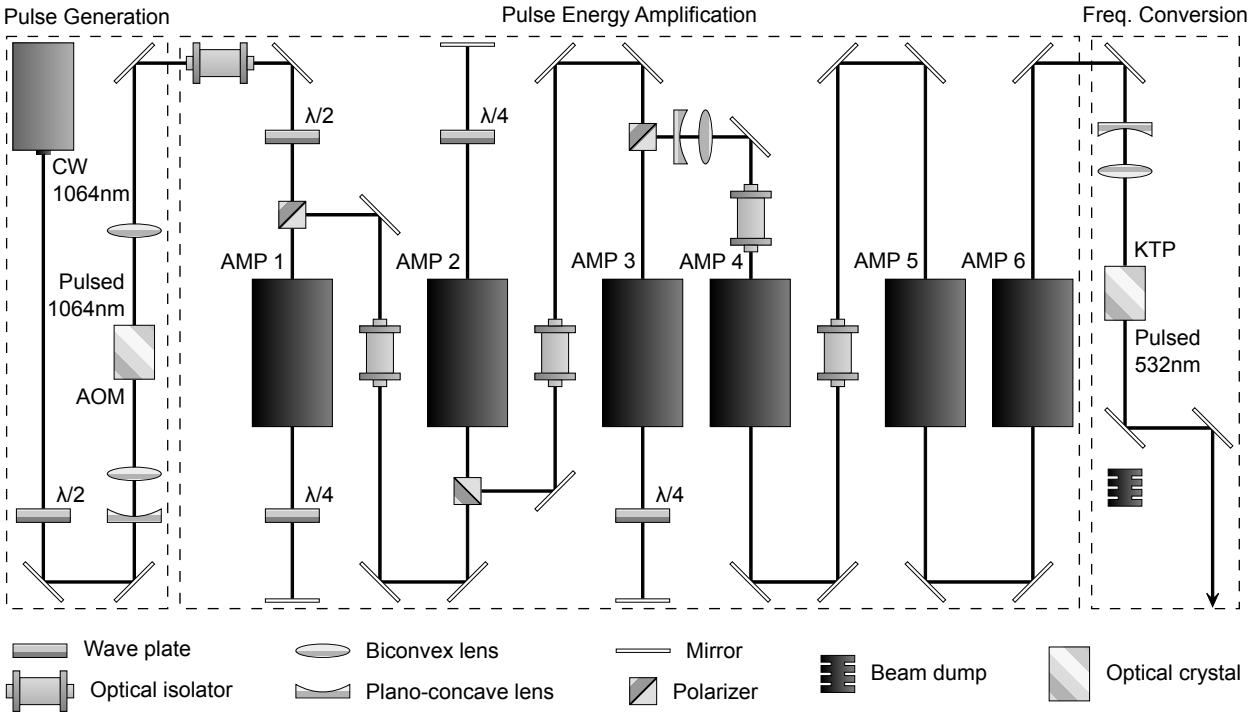

Figure 3.3: Pulse burst laser system utilized for time-resolved (TR) PIV (top view).

The design of the pulse burst laser system can be divided into three fundamental parts as indicated in the schematic: the pulse generation, the pulse energy amplification, and the

frequency conversion. As the name suggests, the function of the pulse generation stage is to slice the output of the CW laser into a burst of low-energy, short-duration pulses. Slicing is achieved through the use of an acousto-optic modulator (AOM) that relies on the principles of the acousto-optic (AO) effect. In particular, a piezoelectric transducer is used to produce acoustic waves inside an optical crystal such that the traveling waves cause variations in the index of refraction of the crystal. To an optical beam, these variations appear as a sinusoidal grating in which the wavelength is equal to the acoustic wavelength. By controlling when and how frequently acoustic waves are produced inside the crystal, the generation of a specified number of short-duration pulses is possible depending on how often the CW input beam is disturbed. As with most AO devices, the AOM operates in the Bragg regime where most of the incident light can be diffracted into the first-order beam fairly efficiently. This diffracted beam constitutes the desired burst of pulses utilized in experimental applications.

Following the formation of low-energy (nanojoule order), short-duration pulses, the remaining stages of the pulse burst laser consist of pulse energy amplification and frequency conversion. Amplification is provided by six flashlamp-pumped Nd:YAG rod amplifiers of increasing diameter and is necessary if the pulses are to be used for fluid-mechanical measurements. The first three amplifiers are used in a double-pass arrangement, whereas the final three allow only for single passes. Without going into detail, wave plates and polarizers provide the necessary means for achieving double passes through the first three amplifiers. Optical isolators between each of the first five amplification stages prevent problems associated with parasitic lasing and amplified spontaneous emission (ASE). By the end of the amplification chain, pulse energies have increased by a factor of more than 10^7–10^8 and generally reach levels in excess of 50 millijoules per pulse[1].

The final stage of the pulse burst laser system is the conversion of the beam's wavelength from 1064 nm to 532 nm. This conversion is achieved via a nonlinear process inside a KTP crystal and results in an unavoidable loss of pulse energy. Nevertheless the beam, now in the

[1]This value is measured after the frequency conversion stage and thus accounts for the loss in energy associated with doubling the frequency of the Nd:YAG laser beam via a KTP crystal.

visible spectrum, can be used for fluid-mechanical measurements including PIV and other flow visualization applications.

3.3.2 Cordin 222-4G high-speed camera

Images are acquired using a Cordin 222-4G gated intensified CCD framing camera that is capable of recording 16 images at a maximum, equally spaced rate of 2,500,000 frames per second[2]. Such images are captured with a 2048×2048 square pixel (px^2) resolution, although the true resolution is less due to the inherent intensification process. The camera is able to achieve extremely high acquisition rates because it contains eight independently controlled optical pathways, each incorporating a microchannel plate (MCP) for signal intensification and ultimately terminating with a Kodak KAI-4022 CCD sensor. Schematics of

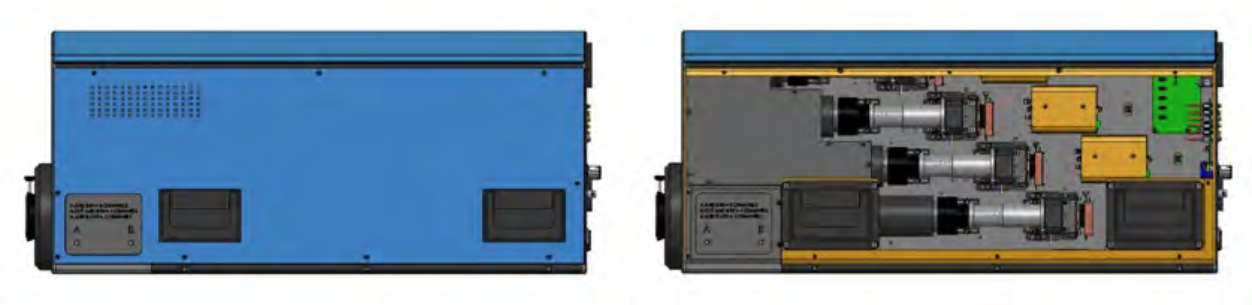

(a) Exterior view (courtesy of Cordin Company) (b) Interior view (courtesy of Cordin Company)

Figure 3.4: Side profiles of the Cordin 222-4G camera utilized for TR PIV.

the camera, including an interior view that illustrates four of the optical pathways, are shown in figure 3.4. By allowing each CCD to record 2 images, 16 total images can be acquired over a user-specified time period. Furthermore, because each pathway is independently operated, temporal spacing between frames is variable and can be set in an asynchronous fashion. Such flexibility even allows eight simultaneous exposures to be made. This feature is desirable since it enables eight theoretically identical particle images to be obtained, with any differences being directly attributable to error. More discussion on this topic is given in chapter 6.

[2]This rate assumes a necessary CCD transfer time of 3.2 μs (specified by Cordin Company) to ensure that the second exposure does not include images from the first exposure.

For the experiments of interest it is sufficient to note that because the camera can acquire 16 images over a user-specified, extremely short time period, temporal resolution is possible for all captured fluid motions. Additionally, the ability to obtain several particle images at varying time intervals relative to one another provides the means of performing HDR PIV. As described, such measurements offer significant improvements over conventional PIV results since optimum temporal separations can be selected for different particle locations depending on the local velocity.

3.4 Experimental arrangement

The combined use of the pulse burst laser and the Cordin high-speed camera allowed time-resolved PIV measurements to be made on a high-temperature (1350°F), supersonic jet. For all cases only a smooth bore conical C-D nozzle with an upstream centerbody section (shown in figures 3.5(a) and 3.5(b)) was considered at over-expanded conditions (Mach 1.55). Such conditions are typical of aircraft exhaust during takeoff and low-altitude operation. The actual nozzle consisted of two conic sections, one contracting and the other expanding, joined together to form a supersonic nozzle with a very sharp radius of curvature at the throat. This near discontinuity at the throat is significant since it allows shocks to exist even when the nozzle is operated at fully expanded conditions (Mach 1.74). To illustrate this effect, a mean profile of the near-nozzle velocity field determined by computational fluid dynamics (CFD) is shown in figure 3.5(c). As indicated in the profile, the streamlined centerbody was positioned well upstream of the nozzle contraction section. It should be noted that this nozzle assembly without the centerbody piece represents a $1/10^{\text{th}}$ scale model of the military power setting for the General Electric F414 engine.

The field of view for this work was chosen along the bottom shear layer of the jet and was centered at a distance 14 inches (7 jet diameters) downstream of the nozzle exit. This distance was selected based on previous measurements indicating the collapse of the jet potential core. The region imaged was slightly less than 16 square inches and was illuminated by a laser

(a) Nozzle centerbody (upstream view)

(b) Nozzle centerbody (downstream view)

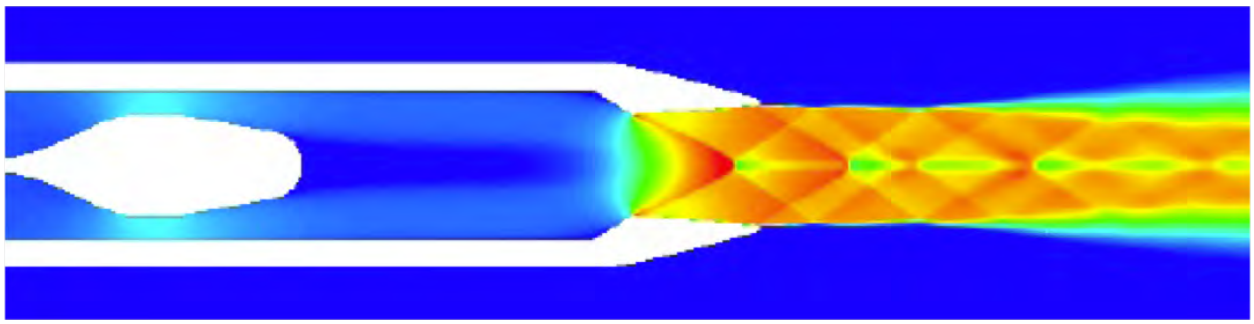

(c) Mean velocity field determined by computational fluid dynamics for the centerbody configuration at fully expanded conditions (Murray et al. [27])

Figure 3.5: The centerbody section included in the nozzle assembly is shown in (a) and (b). The shock structures existing at fully expanded conditions are evident in (c).

sheet directed vertically upwards and spanning axially along the centerline of the jet. This particular orientation was chosen for a variety of reasons including both the need to minimize disruptions in the anechoic environment as well as to ensure the most direct observation of any shear layer without passing the light sheet through the jet prior to imaging. This last point was especially important to prevent problems associated with aero-optical distortions. Figure 3.6 illustrates the position of the imaged region relative to the nozzle exit and the jet centerline (drawing not to scale).

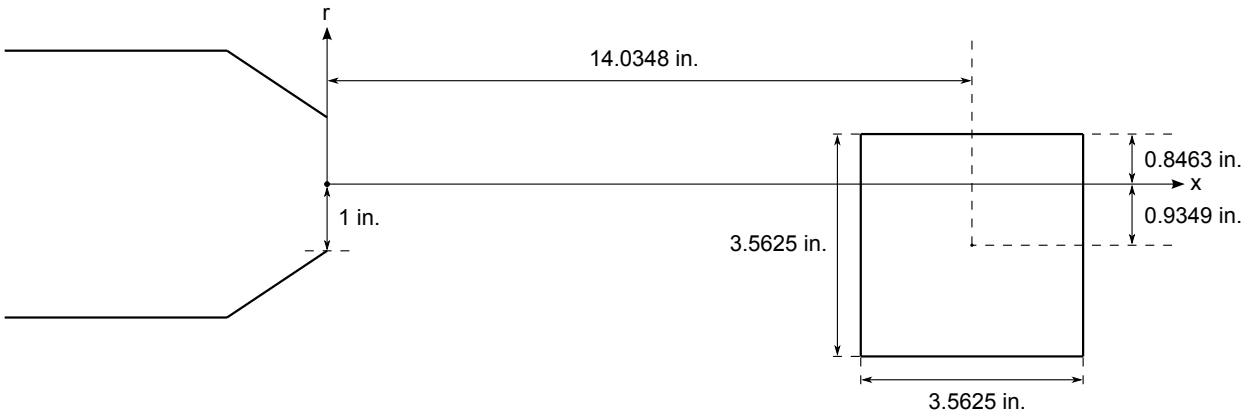

Figure 3.6: Position of the imaged region in the TR PIV application relative to the nozzle exit and the jet centerline (side view). The square region indicates the camera's field of view.

Particle seeding for light scattering was achieved using aluminum oxide (Al_2O_3) particles nominally 0.3 μm in diameter. A nitrogen-pressurized reservoir filled with these particles was connected to the burner system upstream of the nozzle assembly and immediately following the propane combustor and diffuser, respectively. Four seeding tubes were attached around the burner system symmetrically to provide a uniform seeding density throughout the jet. To alleviate particle clumping, a spinning propeller inside the reservoir formed a cloud of aluminum oxide particles that was subsequently dispersed into the particle seeding tubes. Each connection between the reservoir and a tube was made in the supersonic portion of a miniature de Laval nozzle located at the entrance to each tube. This arrangement ensured that any surviving particle clumps were sheared apart before being injected into the burner system.

A schematic of the experimental setup is shown in figure 3.7. The 532 nm wavelength beam from the pulse burst laser was passed into the anechoic chamber perpendicularly to the jet axis and opposite the location of the camera. A turning mirror attached to the stand for the burner system allowed the beam to be directed downstream of the nozzle exit before encountering a 1000 mm biconvex spherical lens and a second turning mirror. The beam was then redirected vertically upwards through a cylindrical lens to form the laser sheet required for light scattering. Extreme care was taken to ensure that this light sheet was oriented both

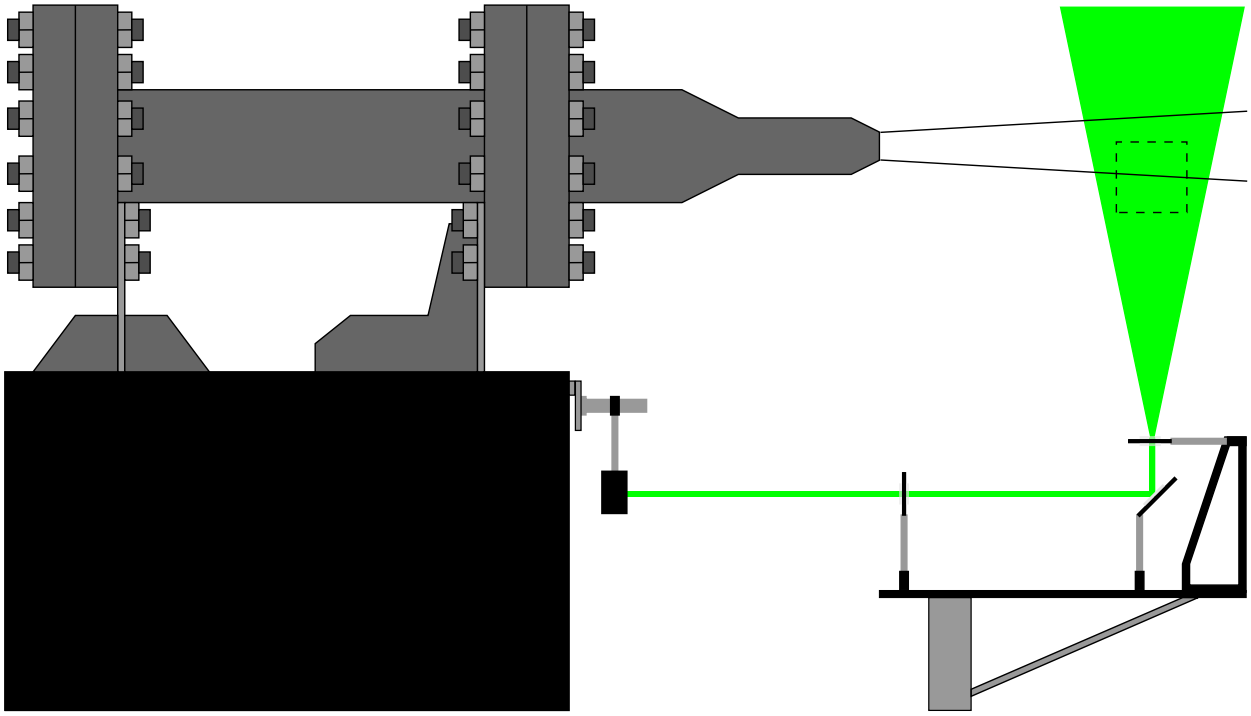

Figure 3.7: Experimental arrangement for the TR PIV application (side view). The square region enclosed by the dashed line indicates the camera's field of view.

orthogonally to the axis of the camera lens as well as to the nozzle exit plane. Additionally, the placement of the spherical lens allowed the thinnest portion of the light sheet to persist across the camera's field of view.

PIV measurements were obtained by synchronizing the framing rate of the camera with the pulse-generating rate of the pulse burst laser system. The chosen rate for all cases was 1 MHz, meaning the 16 images acquired by the camera enclosed a temporal window spanning 15 μs. To achieve the most consistent pulse-to-pulse intensity within each burst, 60 laser pulses were generated for a given burst, and the most stable 16 pulses were selected for synchronization with the 16 camera frames. The duration of each laser pulse was approximately 20 ns such that no image streaking was observed. A Nikon Nikkor F-mount 70-300 mm objective zoom lens (f/4-5.6G) was used with the Cordin camera to acquire all image sequences. Further information regarding the operational parameters and timing settings used during the experiments is given in appendix A.

Chapter 4

Dynamic Evaluation via Ordinary Least Squares (DEVOLS)

As noted in chapter 2, flows containing a wide velocity distribution present a major challenge to PIV algorithms. The reason is because particle motions in these flows (i.e., particle displacements in recorded images of these flows) can vary greatly depending on the local velocity. Since the entire range of flow velocities and thus particle motions cannot be adequately captured in a single interframe time, the temporal spacing in conventional PIV applications must be chosen such that only flow phenomena of interest are properly sampled. To overcome this problem and others related to temporal variations in particle-image patterns, HDR techniques like the ones described previously are currently being developed.

This chapter presents a novel HDR approach designed specifically for the experiments of interest, that is, the characterization of the near-nozzle velocity field in a supersonic jet using TR PIV measurements. The conceptual idea for the approach is based largely on the MF method developed by Hain and Kähler [22]. Using the correlation results of symmetrically centered image pairs with increasing temporal separations, a single velocity field can be constructed entirely from local evaluations. This approach differs from the previous ones, however, in that individual vectors are determined from the combined influence of measurements achieved at multiple interframe times. By considering the results of several image pairs during each local evaluation, significant improvements can be made regarding measurement accuracy and individual vector quality. The following sections discuss the proposed HDR processing scheme, termed dynamic evaluation via ordinary least squares (DEVOLS), and its implementation into the experimental analysis. Validation for the procedure is also given by using synthetically generated images with known particle displacements. The effects that particle density and image noise have on the algorithm are specifically addressed.

4.1 DEVOLS overview

In the experiments of interest the ability to obtain 16 particle images at varying time intervals with respect to one another has provided the means of performing HDR PIV. Unlike conventional PIV where only one temporal spacing is available for all velocity determinations, the multiple combinations of image pairs in this investigation enable a single velocity field to be constructed from the results of several different local evaluations. In spatial regions where little or no particle motions are observed between subsequent frames, the results of image pairs spanning greater temporal distances are also considered. Thus it is entirely possible for vectors in the low-velocity regions of a flow field to be determined using the results of all available image pairs. In this way the DVR is dramatically improved because velocity ranges corresponding to a variety of interframe times are properly and simultaneously sampled.

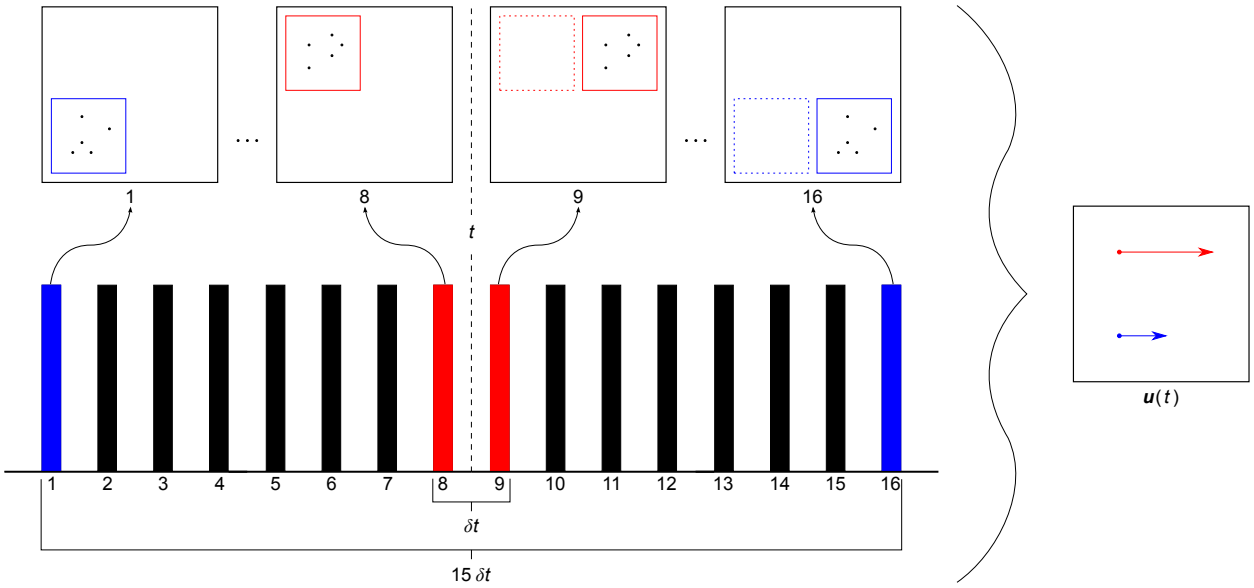

Figure 4.1: Basic principle of high dynamic velocity range (HDR) PIV in relation to the experiments of interest. A single velocity field at t is determined by combining the local evaluations of symmetrically centered image pairs. Depending on the local velocity, the number of image pairs used for a single vector evaluation is variable. The increased dynamic velocity range compared to conventional PIV allows improved measurements to be obtained.

A schematic illustrating the basic principle of HDR PIV in relation to the experimental investigation is shown in figure 4.1. As mentioned, sequences of 16 images were able to be

obtained in which the δt between subsequent frames was specified to be 1 μs. This particular interval was chosen such that the maximum flow velocities and their corresponding particle-image displacements would produce optimum results in the correlation analyses between consecutive frames. By setting the data acquisition rate to properly sample the maximum flow velocities, the slower velocity ranges were inherently over-sampled and thus all image pairs could be used. Considering the temporal arrangement of all 16 frames in the schematic, the velocity field located between frames 8 and 9 is determined by considering the local results of all image pairs symmetrically straddling the point designated t. It should be noted that velocity fields at other points in time could also be computed, however this particular position allows the maximum number of image pairs to be used with central finite differencing. As is evident, for regions of the velocity field containing the highest local velocities, that is, the largest particle displacements between consecutive images, only the image pair shown in red is considered for analysis. Contrarily for regions containing little or no particle motions, multiple image pairs spanning larger temporal distances are considered. The image pair shown in blue represents the case of maximum temporal spacing and spans the entire sequence window of $15\,\delta t$ or 15 μs. By using the information available across all 16 frames instead of only consecutive images, significant improvements in desired flow measurements can be made. Revisiting the mathematical relation discussed previously (equation 2.3), the reason is because the DVR is increased by a factor of 15 compared to conventional PIV methods. The following equations demonstrate this effect by combining the individual correlation results for the minimum (δt) and maximum ($15\,\delta t$) interframe times.

δt :

$$\boxed{\boldsymbol{u}_{max,1} = \frac{\Delta \boldsymbol{x}_{max}}{\delta t}} \qquad (4.1)$$

$$\sigma_{\boldsymbol{u},1} = \frac{\sigma_{\Delta \boldsymbol{x}}}{\delta t} \qquad (4.2)$$

$15\,\delta t$:

$$\boldsymbol{u}_{max,15} = \frac{\Delta \boldsymbol{x}_{max}}{15\,\delta t} \qquad (4.3)$$

$$\boxed{\sigma_{\boldsymbol{u},15} = \frac{\sigma_{\Delta \boldsymbol{x}}}{15\,\delta t}} \qquad (4.4)$$

Considering only the relations denoted by the rectangular boxes above (equations 4.1 and 4.4),

an improved DVR is obtained (equation 4.5). The computational procedure that enables this desired solution to be achieved is described in the section below.

$$\mathrm{DVR} \equiv \frac{\boldsymbol{u}_{max,1}}{\sigma_{\boldsymbol{u},15}} = \frac{[\,\Delta\boldsymbol{x}_{max}\,/\,\delta t\,]}{[\,\sigma_{\Delta\boldsymbol{x}}\,/\,(15\,\delta t)\,]} = 15\,\frac{\Delta\boldsymbol{x}_{max}}{\sigma_{\Delta\boldsymbol{x}}} \tag{4.5}$$

4.2 DEVOLS processing scheme

To begin the DEVOLS processing scheme, each of the symmetrically centered image pairs is first correlated in an initial step. This step represents the most computationally expensive and time-consuming portion of the procedure since each correlation utilizes multiple passes along with several of the latest PIV processing techniques (window deformation and subpixel refinement schemes). Dantec Dynamics software (DynamicStudio v3.31: Smart Software for Imaging Solutions) is used to perform all cross-correlation analyses. In order for a final velocity field to be accurately constructed from the local results, it is imperative that the same number of interrogation windows be used in each of the eight correlations. This requirement ensures that the vector spatial locations comprising each displacement field are positioned and scaled in a 1:1 ratio.

Following the eight correlation analyses, error-minimization criteria are employed to select the most accurate vectors determined at each spatial location. Such criteria are user-specified to allow for increased processing flexibility. To avoid errors stemming from particle accelerations, displacement measurements are first restricted by a maximum displacement limit. This upper bound ensures that high velocity regions are only assessed by image pairs spanning the smallest temporal separations. Contrarily it enables low velocity regions to be evaluated by the maximum number of image pairs. In most cases the highest accuracies are achieved when particle displacements are required to satisfy the one-quarter rule. This rule suggests that in-plane displacements should not exceed one-quarter of the interrogation window size used in the correlation analyses.[8] Although this rule is rendered obsolete by the use of multi-pass/multi-grid algorithms (except for the initial coarse grid), it provides

a reasonable albeit rudimentary condition for the current processing scheme. As will be described, the algorithm at present requires valid particle-image displacements to increase linearly over increasing temporal separations. Modifications to the program in the near future will remove this linear assumption by inherently accounting for local accelerations. More discussion on this topic is given in chapter 7 along with other concluding remarks.

In addition to the particle displacement limit, a specified level of sensitivity is applied by the DEVOLS algorithm when considering the validity of vectors. This criterion is based on the notion that for negligible particle accelerations, all image pairs should in principle provide the same velocity measurement for a given spatial location. Because particle motions under a zero-acceleration condition remain constant with time, a linear trend is observed if their displacements are plotted over time. Considering only the measurements at a single spatial location satisfying the maximum displacement restriction, a linear trend should be observed if they are plotted against their corresponding interframe times. Therefore using ordinary least squares (OLS) statistics, a linear regression line can be fit to the data in which the slope is indicative of the local velocity. A measure of how well this regression line fits the displacement measurements is provided by the coefficient of determination, denoted R^2. Depending on the user-specified sensitivity level, i.e., the minimum-allowable R^2 value, displacement measurements with the largest residuals are simply rejected until either the R^2 value exceeds the required tolerance or only a single measurement remains. In either case the slope of the final OLS regression line serves as the velocity measurement for that particular spatial location.

A final albeit optional feature available to the DEVOLS algorithm is a second pass through the data that utilizes relaxed values of the error-minimization criteria. This feature is designed to further improve the accuracy of vectors in spatial locations where the velocity does not appear to be changing by some appreciable amount. Depending on the user-specified sensitivity level, the entire processing scheme is repeated at such locations although with an increased maximum displacement limit (a modified R^2 tolerance can also be specified but is

not required). In this way an increased number of displacement measurements can be used to achieve a new, more accurate velocity measurement. As mentioned, this feature is only designed to impact spatial locations where the velocity gradients (estimated from the pass one results) appear small. Nevertheless, to avoid potential errors due to local acceleration effects, a velocity measurement from the second pass is rejected if a significant difference between the pass one and pass two results is observed (the user specifies the maximum allowable percent difference). The MATLAB code comprising the proposed DEVOLS processing scheme is included in appendix B.

To better explain the DEVOLS processing scheme, the plots shown in figure 4.2 are considered. In each case the eight displacement measurements for a given spatial location are plotted against their corresponding interframe times. Plots 4.2(a) and 4.2(b) represent the first and second passes of an ideal situation in which the trend of displacement measurements is almost perfectly linear. Contrarily plots 4.2(c) and 4.2(d) correspond to a non-ideal situation in which various outlying measurements are rejected to obtain a higher R^2 value. Because 32×32 px^2 interrogation windows were specified during the correlation analyses, a maximum displacement limit of 12 pixels is imposed for the initial pass (slightly larger than the one-quarter rule would suggest). Based on this restriction (depicted by the dashed red line in plots 4.2(a) and 4.2(c)), five of the eight measurements are immediately rejected in the ideal case, and four measurements are similarly rejected in the non-ideal one. As mentioned, imposing a displacement restriction serves to minimize errors caused by particle accelerations. Such errors become increasingly pronounced over excessive particle displacements since the algorithm currently assumes only linear trends. Considering the remaining three measurements in the ideal case, a linear regression line is computed using OLS statistics with the added constraint that the line pass through the origin (since the limit of $\Delta \boldsymbol{x} = 0$ as $\delta t \to 0$). Because the minimum R^2 tolerance is specified to be 0.975, this line satisfies the sensitivity criterion, and its slope represents the local velocity measurement for pass one. Considering the remaining four measurements in the non-ideal case, the R^2 value of the

first regression line does not exceed the required tolerance. Consequently the measurement with the largest residual (depicted by the red **x** in plot 4.2(c)) is rejected. After computing a second OLS regression line, the new R^2 value is found to exceed the specified tolerance. Thus the slope of this line is indicative of the local velocity at the conclusion of pass one.

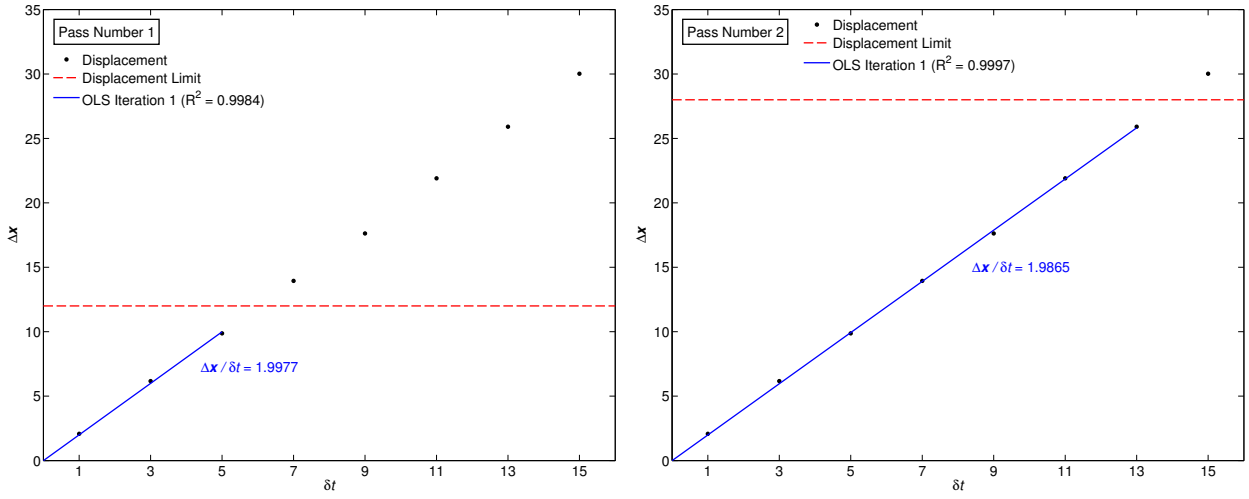

(a) DEVOLS pass 1 (ideal case)

(b) DEVOLS pass 2 (ideal case)

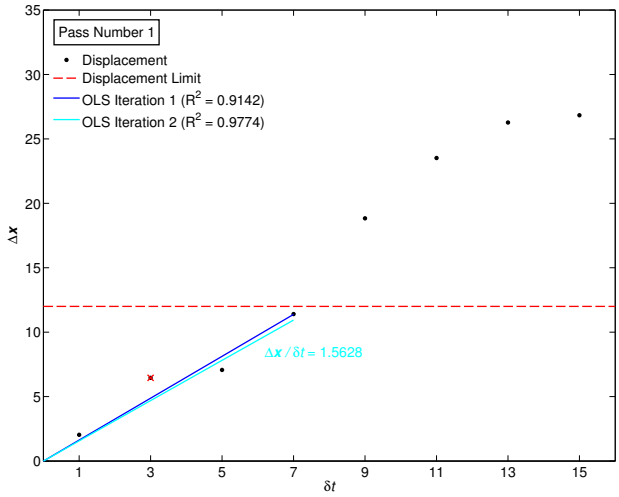

(c) DEVOLS pass 1 (non-ideal case)

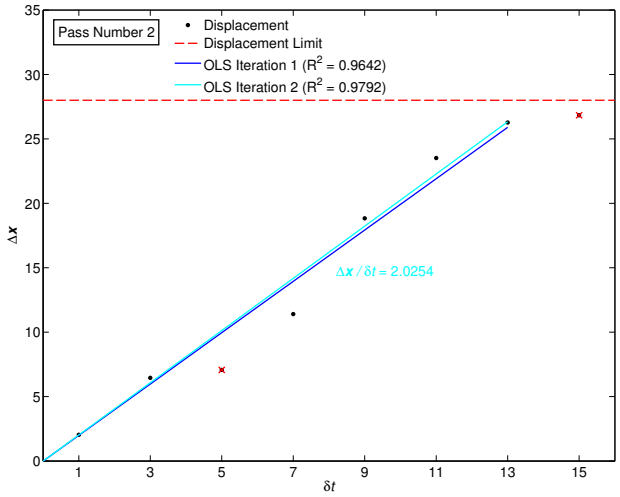

(d) DEVOLS pass 2 (non-ideal case)

Figure 4.2: Graphical explanations of the DEVOLS processing scheme applied at different spatial locations. An ideal case with no outlying measurements is shown in (a) and (b). Plots (c) and (d) illustrate the algorithm's effectiveness at dealing with a non-ideal trend. In all cases measurements are deemed invalid based on a maximum displacement limit and a minimum R^2 tolerance of 0.975 imposed during each pass. The slope of the final OLS regression line is indicative of the local velocity. For the locations shown, $\Delta\boldsymbol{x}/\delta t = 1.9915$ and $\Delta\boldsymbol{x}/\delta t = 2.0355$ are the analytical solutions, respectively, in terms of pixel-velocity.

Because the neighboring velocity measurements (not shown) in both the ideal and non-ideal cases signify regions of low-velocity gradient, the DEVOLS algorithm deems it acceptable to perform a second pass at each location using an increased maximum displacement limit of 28 pixels (slightly less than the dimensions of the interrogation windows employed during the correlation analyses). Although the R^2 tolerance could also be modified, its value is held constant at 0.975 for the cases shown. By repeating the procedure described previously albeit with the larger displacement limit, new velocity measurements are able to be achieved. Furthermore, because of the increased number of displacement measurements considered at each spatial location, a higher accuracy is obtained. The second pass is especially beneficial to the non-ideal case since one of the displacements initially included in the OLS analysis of pass one is actually an outlier. Consequently by removing this measurement and including others, the relative error at this location decreases from over 23.2% to less than 0.5%. As a final note it should be mentioned that although only two spatial locations are considered in the examples shown, the actual processing scheme is performed at all vector positions until a final velocity field is achieved.

4.3 DEVOLS validation

To validate the DEVOLS processing scheme, a time-resolved sequence containing 16 synthetically generated particle images was considered. The particle density (ρ_{IA}) in each image was chosen such that on average each interrogation window would contain 24 particles. The particle diameters were allowed to vary at most by 1 pixel from a nominally specified value of 5 pixels[1]. In addition, the particles were allowed to exit the field of view based solely on their in-plane motions. The particles could also vary in depth within the light sheet (sheet thickness for the range [0 1] was set at 0.3), although such positions were fixed since no out-of-plane motion was permitted. For the initial case only zero-noise conditions were

[1]Large particle-image diameters were specified to better resemble the particles found in the experimental images. As mentioned, the resolution in these images is inherently reduced due to the intensification process associated with the camera. Thus the minimum resolvable particle-image diameter associated with this camera is larger than would be expected for a non-intensified CCD camera with a comparable sensor size.

simulated. To maintain consistency with the Cordin CCD sensors, the image sizes were specified to be 2048×2048 px^2. The program used to generate all images was a modified version of the synthetic particle-image generator in PIVlab, the time-resolved digital particle image velocimetry tool for MATLAB.[38] Sample particle images are shown in figure 4.3.

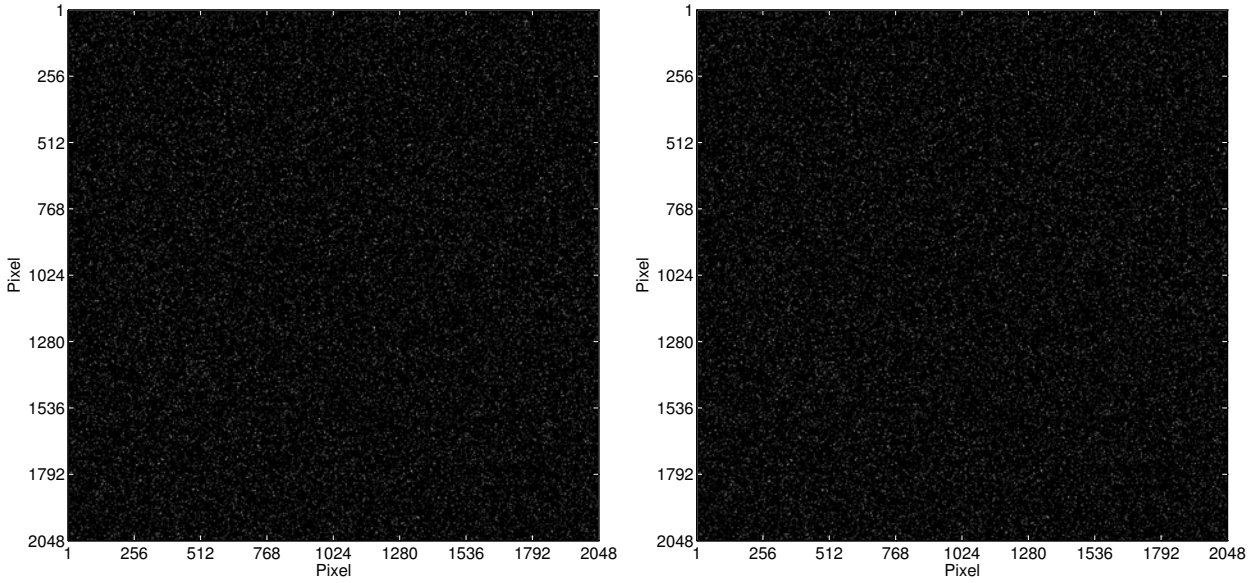

(a) Synthetic image 2 of 16

(b) Synthetic image 4 of 16

Figure 4.3: Synthetically generated particle images for a Hamel-Oseen vortex. Each image contains zero noise and slightly less than 100,000 particles.

The flow field simulated in the synthetic image sequence was a Hamel-Oseen vortex centered at the position (1024.5, 1024.5). The maximum circulation in terms of maximum particle displacement between consecutive, subsequent frames was limited to 8 pixels. This value was chosen such that the one-quarter rule would be satisfied for 32×32 px^2 interrogation windows over a single interframe time. A 50% overlap was specified for these windows during the correlation analyses. A vortex was chosen to validate the DEVOLS processing scheme because it provides a geometrically simple case of flow containing a wide velocity range. Thus depending on the interframe time, portions of the flow field are inherently under-sampled or drastically over-sampled when investigated by conventional PIV.

The inability of conventional PIV to resolve the full DVR of the Hamel-Oseen vortex is evident in the correlation results presented in figure 4.4. A small interframe time (δt)

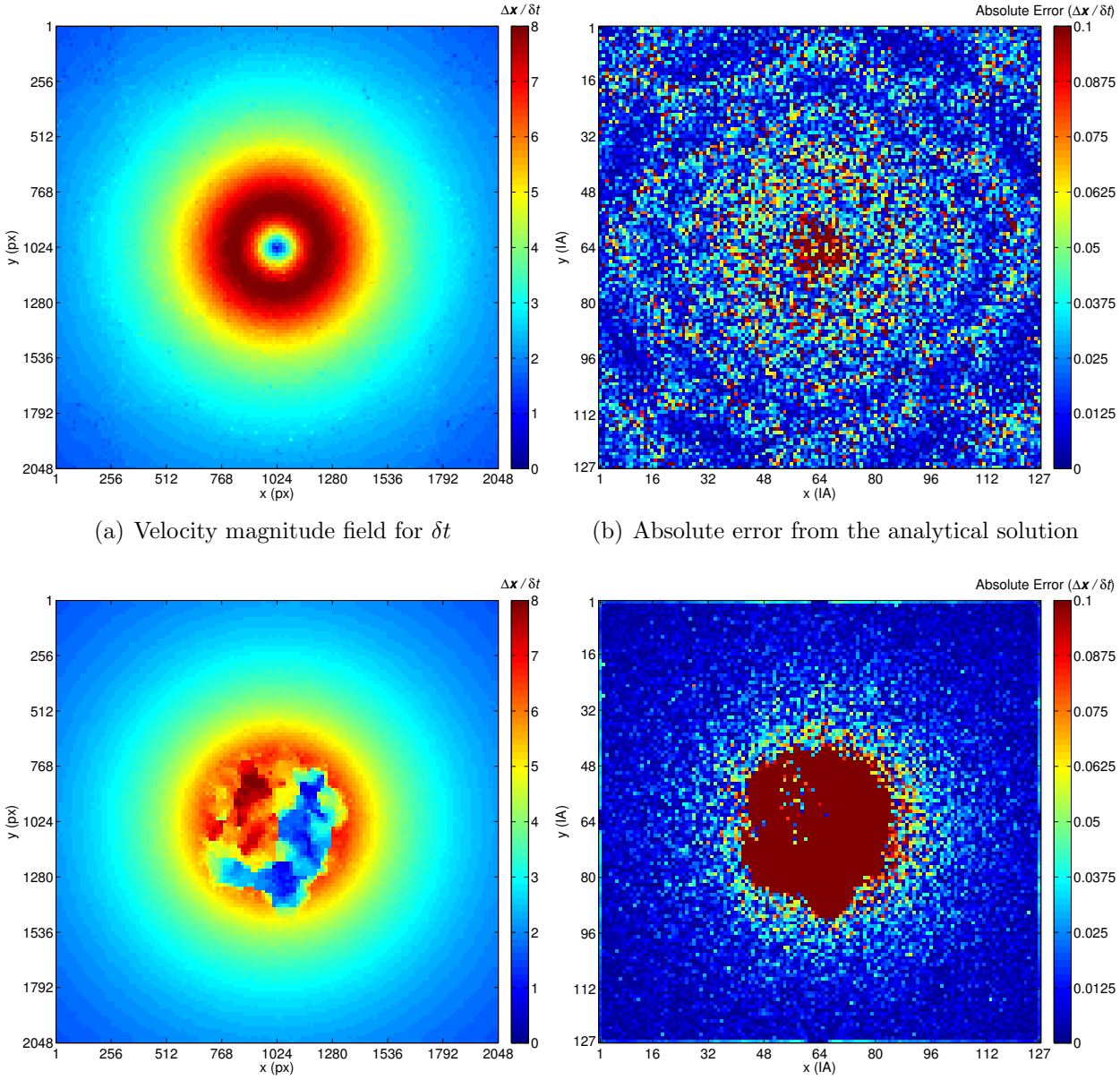

(a) Velocity magnitude field for δt

(b) Absolute error from the analytical solution

(c) Velocity magnitude field for $15\,\delta t$

(d) Absolute error from the analytical solution

Figure 4.4: Velocity magnitude fields and corresponding absolute errors for the image pairs spanning δt and $15\,\delta t$, respectively. Each field contains over 16,000 local velocity measurements for a synthetically generated Hamel-Oseen vortex. As is evident by the absolute error plots, in both cases a single interframe time is insufficient to resolve the full DVR of the flow. The contour coloring scheme in all plots is indicative of the local pixel-velocity ($\Delta\boldsymbol{x}/\delta t$).

provided by the central image pair (frames 8 and 9) can resolve the high-velocity regions near the vortex core but in doing cannot adequately resolve the remaining low-velocity regions (figure 4.4(a)). As a result, measurement accuracy for individual vectors in these

regions is of poor quality. Contrarily a large interframe time provided by the image pair (frames 1 and 16) spanning the entire temporal window of $15\,\delta t$ is unable to resolve the core (figure 4.4(c)). In this case, however, the low-velocity regions surrounding the core and nearing the image edges are highly resolved. The plots (figures 4.4(b) and 4.4(d)) presented alongside each velocity magnitude contour represent the total deviations, or absolute errors, in pixel-velocity that exist for each respective measurement. The patterns visible in these plots clearly illustrate the trends described previously. For both cases the low DVR in the measurements severely limits the viability of conventional PIV applications. Nevertheless, because this investigation represents the ideal case of zero noise, the individual correlations still perform very well. Results for all eight image pairs utilized in the HDR analysis are given in appendix C. Additional results for a similar investigation involving a pair of Hamel-Oseen vortices are provided in appendix D.

By employing the DEVOLS processing scheme described in the previous section, up to eight displacement measurements (one from each of the eight correlation analyses) can be considered at each spatial location to obtain a more accurate measurement of the velocity field. The fact that multiple interframe times are able to be used allows this measurement to characterize a much higher DVR of the flow than before. The plot shown in figure 4.5(a) contains the velocity magnitude field for the HDR result. The error minimization criteria specified in the DEVOLS algorithm to achieve this result were 12 pixels and 28 pixels for the particle displacement limits (first and second passes, respectively) and 0.975 for the R^2 tolerance. Unless specified, these values should be assumed for the HDR results contained in the remainder of this thesis. As before, the total deviation field in pixel-velocity from the analytical solution is shown in figure 4.5(b). The patterns visible in this plot with respect to the ones shown previously clearly illustrate the effectiveness of the algorithm.

To further quantify the performance of the DEVOLS processing scheme, the errors associated with the highest and lowest velocity ranges are considered. Because the ultimate goal of the algorithm is to increase the DVR of TR PIV measurements without jeopardizing

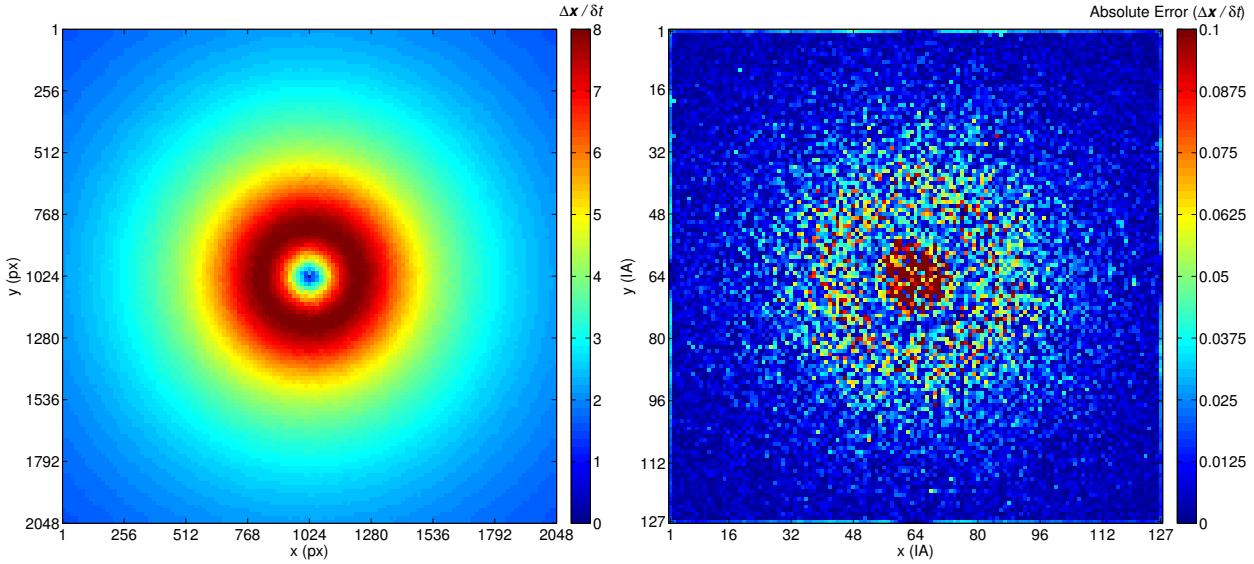

(a) Velocity magnitude field for the HDR result

(b) Absolute error from the analytical solution

Figure 4.5: Velocity magnitude field and corresponding absolute error field, respectively, for the HDR result. This result characterizes the DVR of the flow much better than the results shown previously (figure 4.4) since it is not restricted to a single interframe time. The patterns visible in the absolute error plot clearly illustrate this fact.

the errors found in conventional applications, it is imperative that the errors associated with the velocity extrema in the HDR result never exceed those values corresponding to the best-performing, individual correlations. From a theoretical perspective, a constant and optimum level of accuracy should be achievable for all velocity ranges assuming no accelerations and an infinite number of image pairs. In this case the accuracy would only be limited by the errors inherent to the latest PIV processing schemes. While this scenario is hardly practical, it serves as the theoretical limit for the current HDR algorithm. Hence the DEVOLS procedure is not designed to improve the correlation errors associated with state-of-the-art PIV processing software, rather it is intended to extend the velocity range over which such optimum correlation errors can be achieved.

Figure 4.6 contains the average absolute error results, in terms of pixel-velocity, for the velocity extrema of the Hamel-Oseen vortex. The vector plot in figure 4.6(a) represents the analytical solution for the vortex and is color-coded to signify regions of high and low velocity magnitude. The high-velocity vectors (red) contain magnitudes greater than 90% of

the total vector field. Similarly the low-velocity vectors (blue) correspond to measurements with magnitudes in the lowest 10%. The remaining 80% of vectors are shown in green. Each of the lines plotted in figure 4.6(b) is obtained by averaging the absolute error results for the vectors contained in one of these velocity ranges (the lines are also color-coded). The points in each solid line correspond to the individual correlation results, and the dotted lines signify the HDR result. As is evident, the errors associated with the HDR result are less than the ones observed in the individual correlation results for all cases.

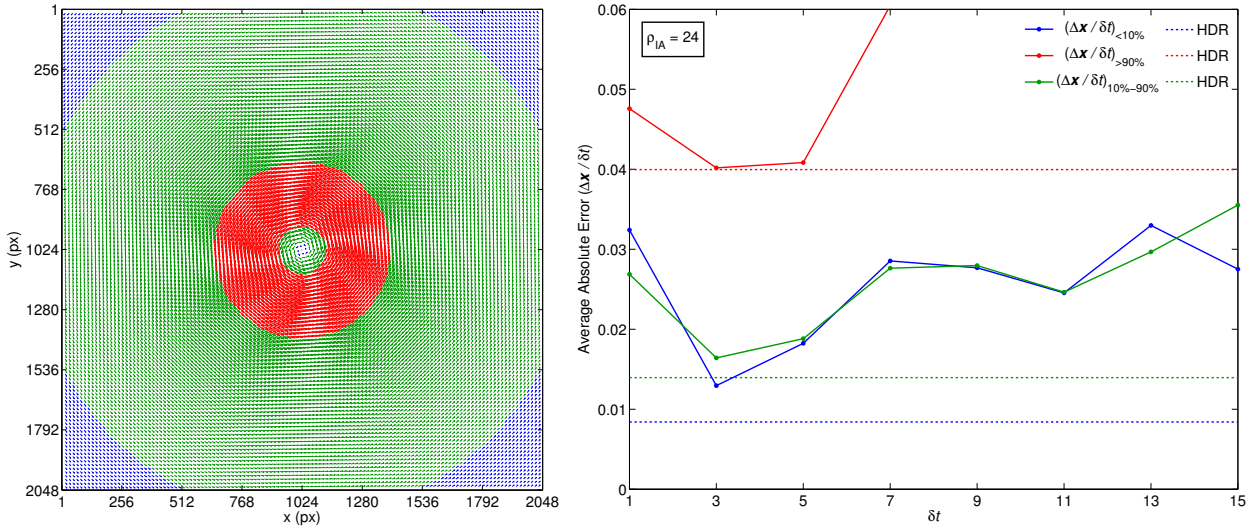

(a) Velocity extrema for the analytical solution (b) Average absolute errors for the velocity extrema

Figure 4.6: Velocity extrema and corresponding average absolute errors, respectively, for the Hamel-Oseen vortex. The vector plot in (a) represents the analytical solution for the vortex where the coloring scheme is indicative of the highest (red) and lowest (blue) velocity regions. The plot shown in (b) corresponds to the average absolute errors determined for each of these regions. The errors found in the HDR result (dotted lines) are less than the errors associated with the individual correlation results (solid lines) for all interframe times.

As expected, the HDR approach fared much better than the individual correlations at resolving the full DVR of the vortex. The obvious reason is because the DEVOLS processing scheme can locally utilize displacement results derived from multiple image pairs and thus multiple interframe times to more accurately sample the variety of flow regimes. Considering the overall velocity profile, only the image pairs spanning the shortest temporal distances should ideally be used to sample the high-velocity regions near the core. Contrarily multiple

image pairs with successively increasing temporal separations should be used to sample the regions located at increasing spatial distances from the core. As illustrated by the plot in figure 4.7(a), this exact trend is observed. The contour coloring scheme in this case is indicative of the number of displacement measurements (N_{vec}) utilized by the DEVOLS algorithm to determine the final OLS regression line at each spatial location. Hence the regions containing the lowest velocity measurements are characterized by the maximum number of image pairs, eight. Figure 4.7(b) also illustrates this trend by plotting the velocity magnitude obtained at each spatial position along the central, horizontal slice through the vortex. As is evident, the HDR result almost exactly matches the analytical solution for all spatial locations, whereas the individual correlations show significant deviations. The results derived from the image pairs spanning the largest temporal distances are especially ineffective at resolving the high-velocity regions near the core.

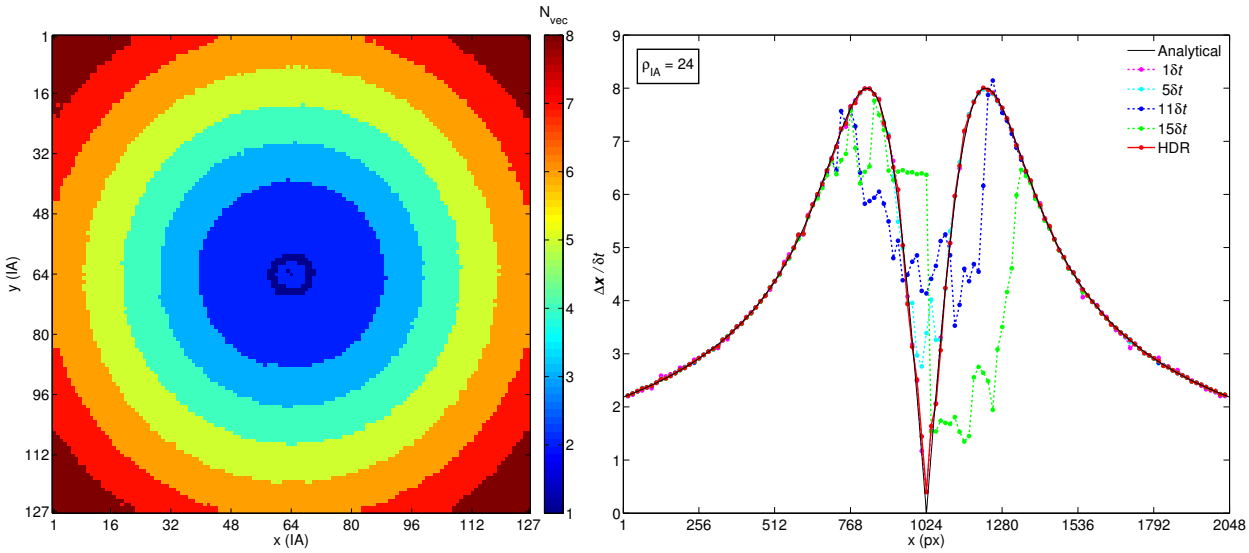

(a) Vectors considered per spatial location

(b) Velocity profile for the central, horizontal slice

Figure 4.7: Results for the vector evaluation field as well as the central velocity profile, respectively. The trends observed in both cases indicate that only image pairs spanning the shortest temporal distances are capable of resolving the high-velocity regions near the vortex core. Contrarily multiple image pairs spanning increasing temporal distances are able to resolve the low-velocity regions. Thus an increased number of displacement results can be utilized to determine the velocities located at increasing spatial distances from the core.

4.3.1 Effect of varying particle density

To characterize the effect that different particle densities have on the DEVOLS algorithm, five temporally resolved image sequences of increasing particle density were synthetically generated for the vortex. All parameters (particle diameter and diameter variation, allowable depth within the light sheet, zero out-of-plane particle motion, maximum circulation in terms of particle displacement between subsequent frames, and zero noise conditions) were held constant between the sequences except the total particle number. In each case this total particle number was chosen such that a desired, average number of particles would be found in the interrogation windows. Similarly as before, 32×32 px^2 windows were specified during the correlation analyses with a 50% overlap. The particle densities considered in this investigation and written in terms of particles per interrogation area are as follows: 3, 6, 12, 24, and 48. As an aside, the HDR results shown previously for a particle density of 24 correspond to the image sequence utilized in this investigation.

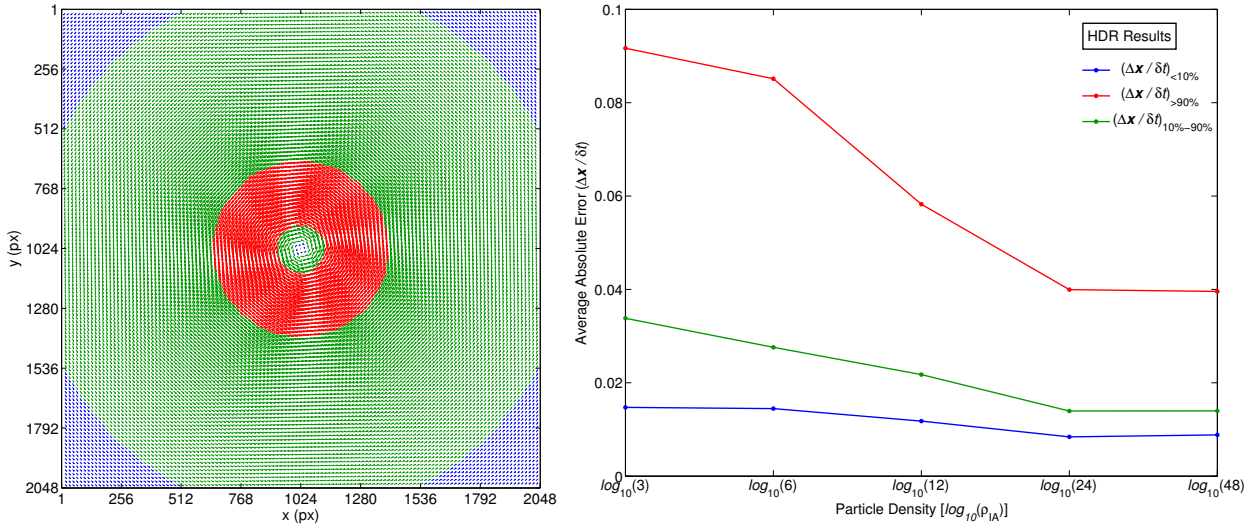

(a) Velocity extrema for the analytical solution

(b) Average absolute errors for the HDR results

Figure 4.8: Average absolute errors for the results of the varying particle density investigation. The vector plot in (a) represents the analytical solution for the Hamel-Oseen vortex where the coloring scheme is indicative of the highest (red) and lowest (blue) velocity regions. The plot shown in (b) corresponds to the average errors determined in each of these regions for the five HDR results. As expected, the error decreases with increasing particle density.

The plots shown in figure 4.8 represent the average absolute errors in the velocity extrema for the varying particle density investigation. Again, the high-velocity regions (red) are comprised of vectors with magnitudes in the top 10% of all vectors, whereas the low-velocity regions (blue) contain vectors with magnitudes in the bottom 10%. The plot shown in figure 4.8(b) illustrates the average absolute error determined in each of these regions for each of the five HDR results. As is evident, the error decreases with increasing particle density for all velocity ranges.

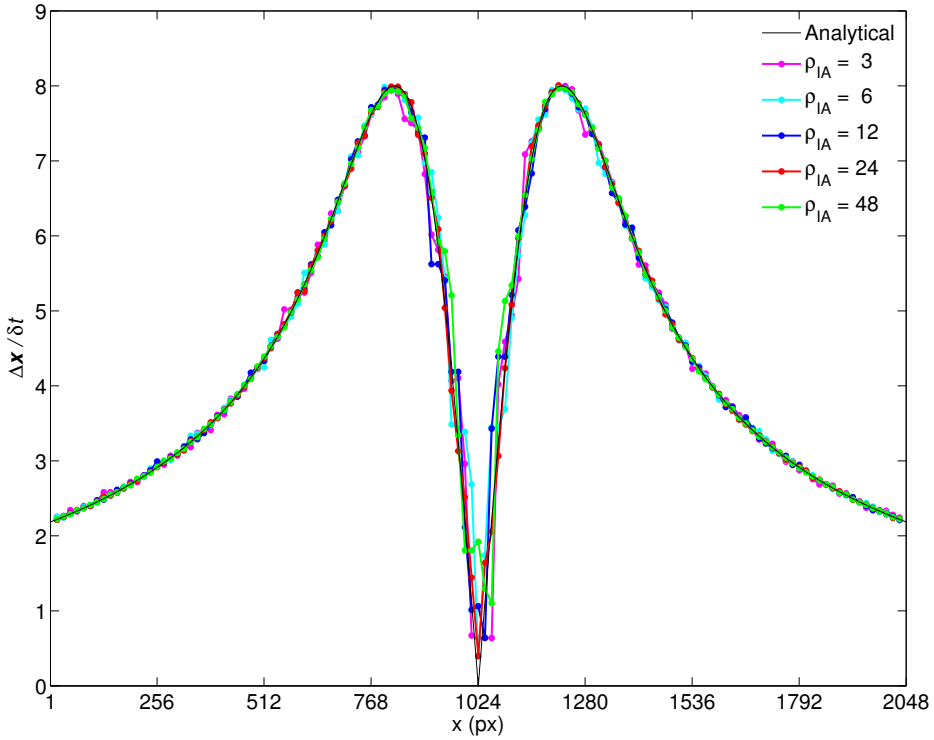

Figure 4.9: HDR results for the Hamel-Oseen vortex in which the particle density was varied. Five temporally resolved image sequences were synthetically generated to contain 3, 6, 12, 24, and 48 particles per interrogation area. The velocity profile shown corresponds to the central, horizontal slice through the vortex.

Considering the plot shown in figure 4.9, the particle densities selected for this investigation did not appear to affect the DEVOLS algorithm in any appreciable way (i.e., the inverse trend observed previously between absolute error and particle density is not apparent in this plot). Although a few deviations are noticeable for $\rho_{\mathrm{IA}} = 3$, the overall velocity profile still closely resembles that of the analytical solution. One would expect the measurement

error to increase rapidly for densities below 3 due to the lack of particles and consequent ambiguity in the correlation analyses. One would also expect the error to increase significantly at some value above 48 due to the increased occurrence of overlapping particle images in the recordings. Quantifying such levels where the DEVLOS processing scheme begins to experience significant deviations relative to conventional PIV algorithms is certainly a topic warranting further investigation.

4.3.2 Effect of varying noise conditions

In addition to varying the particle density, two investigations were conducted to characterize the effects that different noise sources have on the DEVOLS algorithm. In both cases four image sequences of increasing noise levels were considered against a baseline sequence with zero noise. As before, a Hamel-Oseen vortex was simulated in the particle motions, and all parameters were held constant between the sequences except for the variable in question. In both investigations the chosen particle density was 24 ($\rho_{\mathrm{IA}} = 24$), and care was taken to ensure that the initial positions of all particles remained the same. Thus all image sequences were identical in terms of particle density, particle distribution, and particle motion, however they differed in the prescribed level of noise.

Salt and pepper noise The first investigation was designed to simulate intensifier noise where hot spots are known to occur. This feat was accomplished by increasing the level of salt and pepper noise in the image sequences. Such noise affects the individual images within a sequence differently by randomly turning a number of pixels *on* to the maximum intensity value or *off* to the minimum intensity value. For a given sequence the number of pixels affected in each image is governed by a specified noise density (ρ_{noise}) applied to all of the images. Multiplying this value by the total number of pixels in each image yields the total number of pixels affected. Noise densities of 0, 0.025, 0.05, 0.075, and 0.1 were considered in this investigation. Sample particle images for $\rho_{\mathrm{noise}} = 0.0$ (baseline) and $\rho_{\mathrm{noise}} = 0.075$ are shown in figure 4.10, respectively.

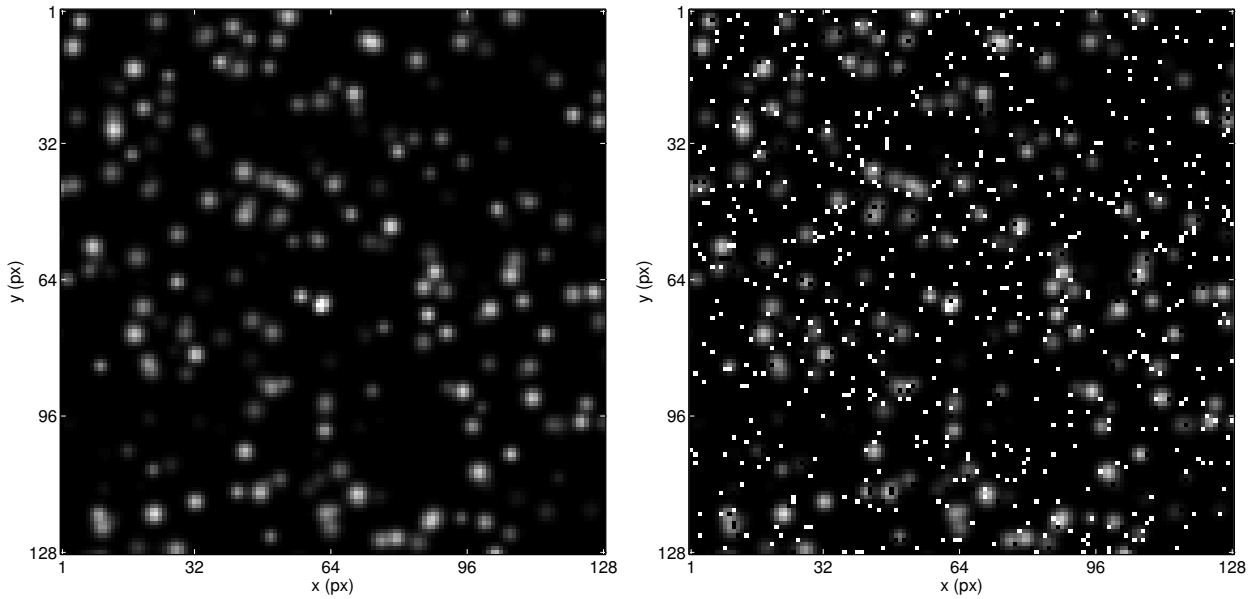

(a) Salt and pepper noise: $\rho_{\text{noise}} = 0.000$

(b) Salt and pepper noise: $\rho_{\text{noise}} = 0.075$

Figure 4.10: Image regions containing different levels of salt and pepper noise. Each region measures 128×128 px^2 and contains an identical particle density and particle distribution.

As before, to quantify the impact that increasing salt and pepper noise has on the DEVOLS algorithm, the average absolute errors in the velocity extrema are considered. The results for the baseline sequence as well as the four image sequences of increasing noise are shown in figure 4.11. In this case (figure 4.11(b)) the average errors are plotted against their corresponding noise densities. As expected, the errors associated with the velocity extrema (top and bottom 10% of all vectors in terms of velocity magnitude) as well as the middle velocity range appear to increase with increasing noise density.

To further assess how various salt and pepper noise levels influence the algorithm, the local velocity measurements along the central, horizontal slice through the vortex are considered. The plot shown in figure 4.12 contains the HDR results of the five image sequences corresponding to this velocity profile. As expected, the number of deviations from the analytical solution appears to increase with increasing noise density, although all results resemble the analytical solution rather closely. The fact that large deviations appear at different spatial positions for different image sequences indicates that the salt and pepper noise applied

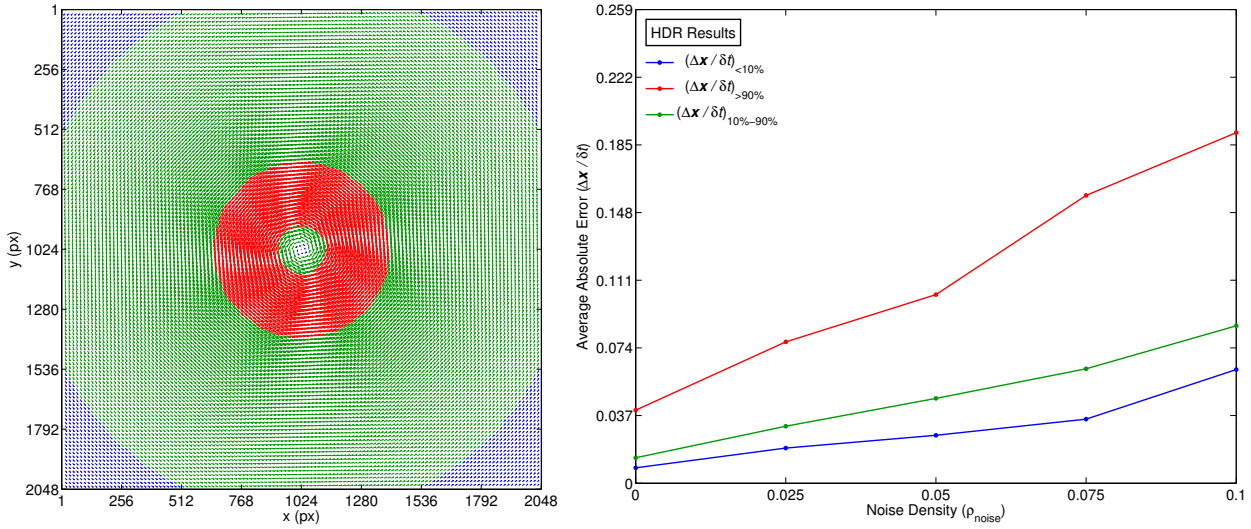

(a) Velocity extrema for the analytical solution

(b) Average absolute errors for the HDR results

Figure 4.11: Average absolute errors for the results of the salt and pepper noise investigation. The vector plot in (a) represents the analytical solution for the Hamel-Oseen vortex where the coloring scheme is indicative of the highest (red) and lowest (blue) velocity regions. The plot shown in (b) corresponds to the average errors determined in each of these regions for the five HDR results. As expected, the error increases with increasing noise density.

to each sequence was sufficiently random. Thus the correlation problems that resulted in the observed spikes were clearly due to the applied noise and not some underlying artifact in the particle-image distribution.

The plots included in figure 4.13 correspond to the HDR result for $\rho_{\text{noise}} = 0.075$. Figure 4.13(a) contains the entire velocity profile, whereas figure 4.13(b) shows an enlarged view of the region indicated by the axes. Despite several deviations from the analytical solution by the individual correlation results, the HDR curve follows the analytical one rather closely. This trend is especially obvious in the high-velocity regions near the core. As expected, the correlations of image pairs spanning the largest temporal distances were mostly affected in these regions and are visible as large deviations from the peaks in figure 4.13(a). In contrast the image pair spanning a single δt was mostly affected in the low-velocity regions near the image edges. Although the observed deviations for this case are significantly less than the ones seen for the larger interframe times, they are clearly visible in the zoomed view.

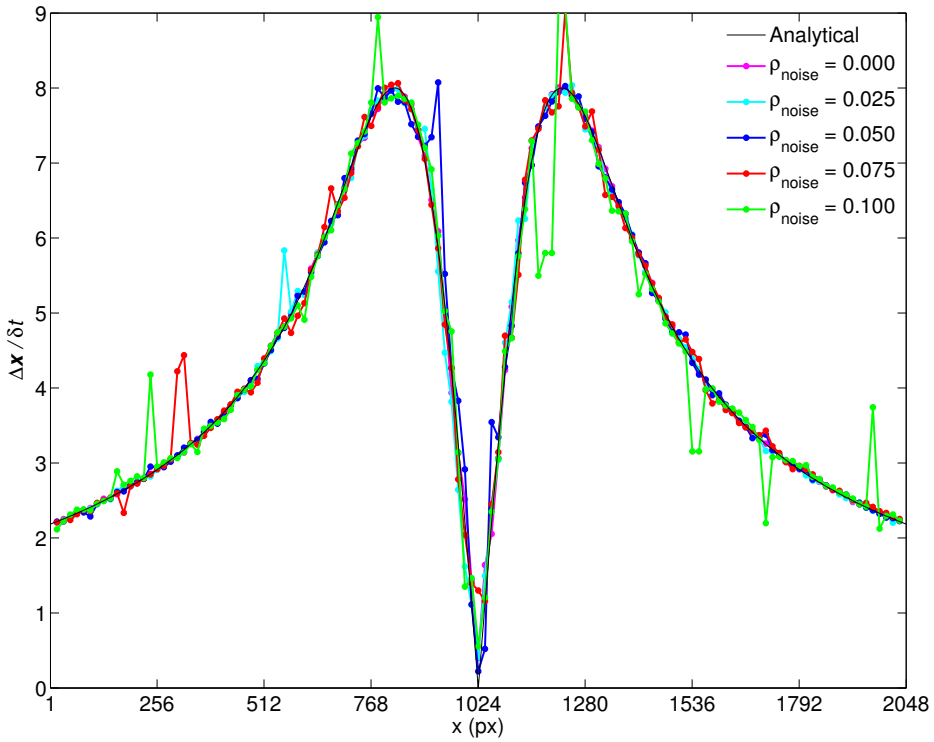

Figure 4.12: HDR results for the Hamel-Oseen vortex in which the prescribed level of salt and pepper noise was varied. Five temporally resolved image sequences were synthetically generated to contain noise densities of 0, 0.025, 0.05, 0.075, and 0.1 (where the density multiplied by the number of pixels per image yields the total number of pixels affected). The velocity profile shown corresponds to the central, horizontal slice through the vortex.

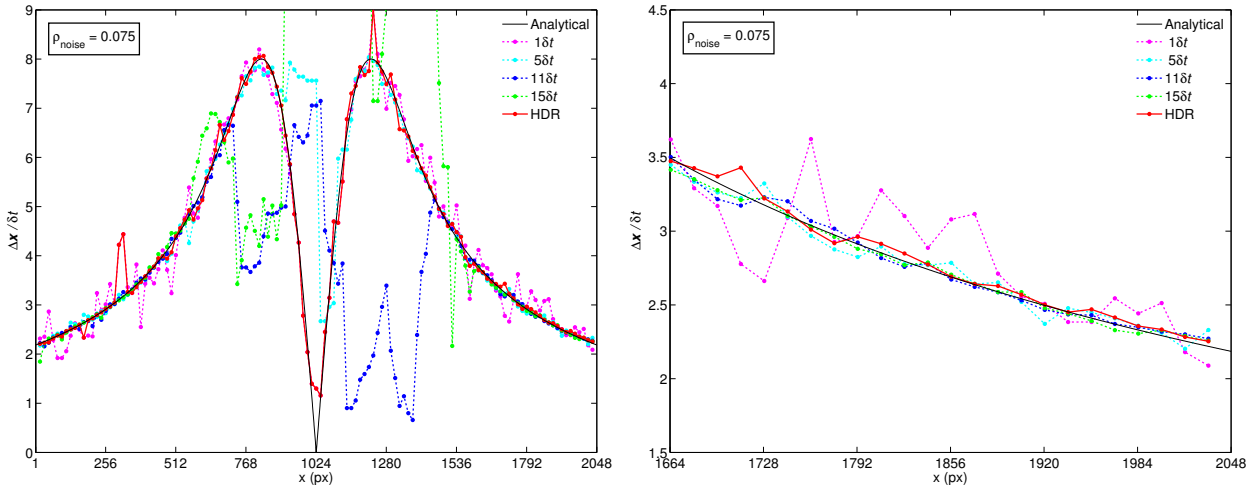

(a) Velocity profile for the central, horizontal slice (b) Enlarged view of the region indicated by the axes

Figure 4.13: Results achieved for the central velocity profile by the image sequence with $\rho_{\text{noise}} = 0.075$. Plots are shown that contain the entire velocity profile (a) as well as an enlarged view of the region indicated by the axes (b). The HDR result performed significantly better than the individual correlation results for almost all cases.

Gaussian white noise The second investigation was also designed to simulate intensifier noise by increasing the level of Gaussian white noise (i.e., the background intensity) in the image sequences. The term *Gaussian* refers to the distribution of noise values in each image (how frequently a particular value appears), and *white* describes the flat shape of the frequency spectrum. As such the noise applied to any two images for a given sequence is statistically independent or uncorrelated. Analogous to the noise density in the previous investigation, the mean (μ) and variance (σ^2) specified in the Gaussian distribution provided the ability to control the level of noise generated for each sequence. In all cases a zero-mean was specified, and variances of 0, 0.025, 0.05, 0.075, and 0.1 were considered. Sample particle images for $\sigma^2_{\mu=0} = 0.0$ (baseline) and $\sigma^2_{\mu=0} = 0.075$ are shown in figure 4.14, respectively.

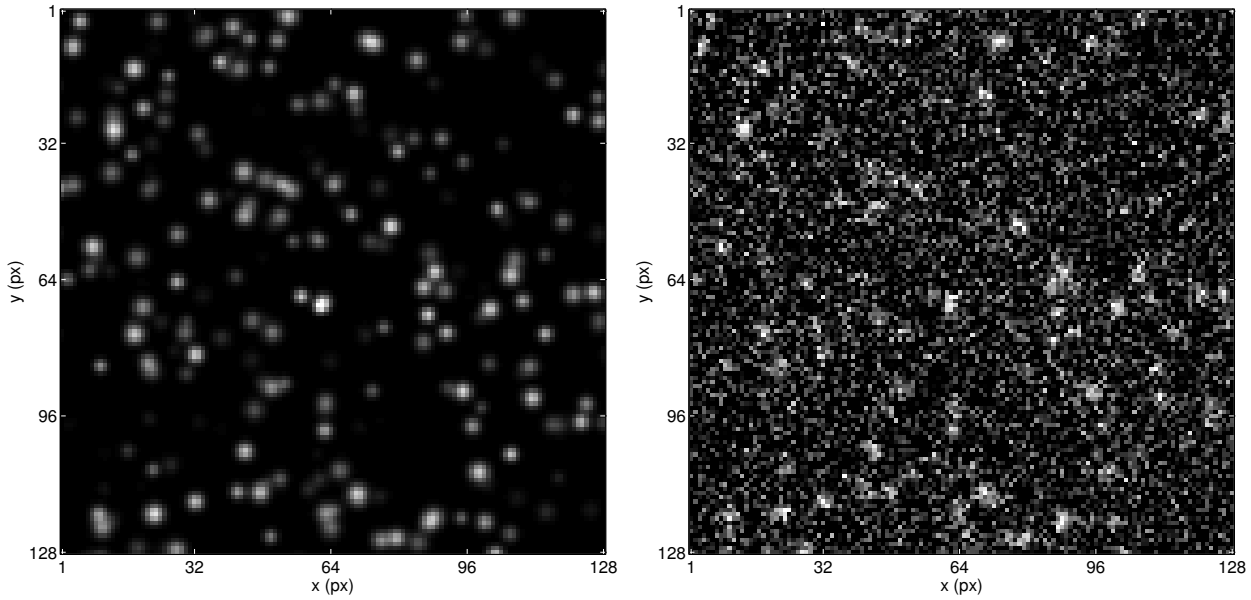

(a) Gaussian white noise: $\sigma^2_{\mu=0} = 0.000$

(b) Gaussian white noise: $\sigma^2_{\mu=0} = 0.075$

Figure 4.14: Image regions containing different levels of Gaussian white noise. Each region measures 128×128 px^2 and contains an identical particle density and particle distribution.

Presenting all results in the same order as the salt and pepper noise investigation, figure 4.15 contains the average absolute errors in the velocity extrema determined for the five HDR results. Obviously the errors in this case are plotted against their corresponding values of variance (figure 4.15(b)). Again as expected, the error in each velocity range

noticeably increases with increasing Gaussian white noise. Moreover, it appears that this noise source had a larger, more detrimental impact on the DEVOLS algorithm than did the salt and pepper noise shown previously (at least for the values considered). This result is significant since intensifier noise is the dominant noise source found in the experimental images due to the intensification process associated with the camera. Thus for optimum results in the DEVOLS processing scheme, the camera should be operated with as little MCP gain as possible to avoid significant levels of noise in the particle images.

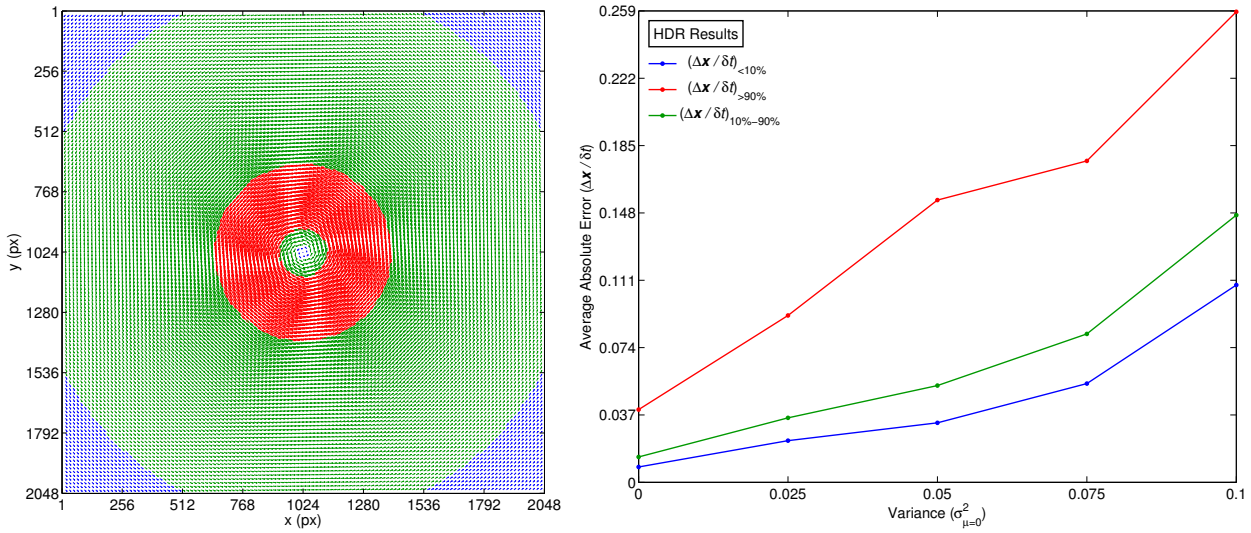

(a) Velocity extrema for the analytical solution

(b) Average absolute errors for the HDR results

Figure 4.15: Average absolute errors for the results of the intensifier noise investigation. The vector plot in (a) represents the analytical solution for the Hamel-Oseen vortex where the coloring scheme is indicative of the highest (red) and lowest (blue) velocity regions. The plot shown in (b) corresponds to the average errors determined in each of these regions for the five HDR results. As expected, the error increases with increasing Gaussian white noise.

The plot shown in figure 4.16 contains the HDR results for the five image sequences considered, namely the baseline case as well as the four cases of increasing noise. As before, the velocity profile corresponds to the velocity measurements achieved along the central, horizontal slice through the vortex. Analogous to the trend observed for increasing salt and pepper noise, the number of deviations from the analytical solution appears to increase for increasing values of variance (Gaussian white noise). Nevertheless, all results resemble the analytical solution to a considerable degree.

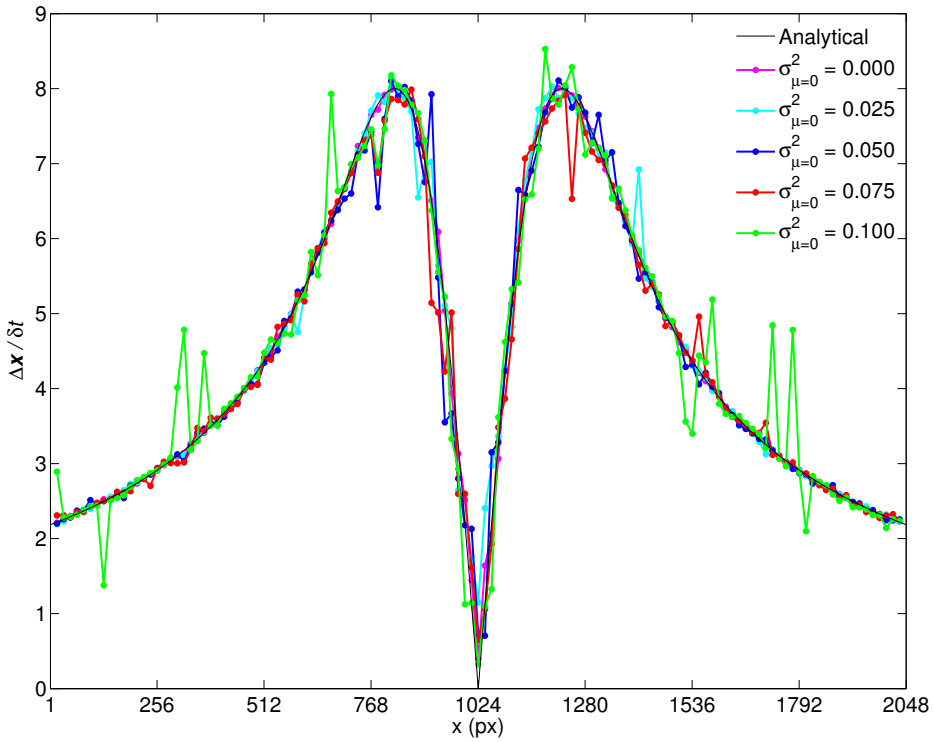

Figure 4.16: HDR results for the Hamel-Oseen vortex in which the level of Gaussian white noise was varied. Five temporally resolved image sequences were synthetically generated to contain zero-mean, Gaussian white noise with variances of 0, 0.025, 0.05, 0.075, and 0.1. The velocity profile shown corresponds to the central, horizontal slice through the vortex.

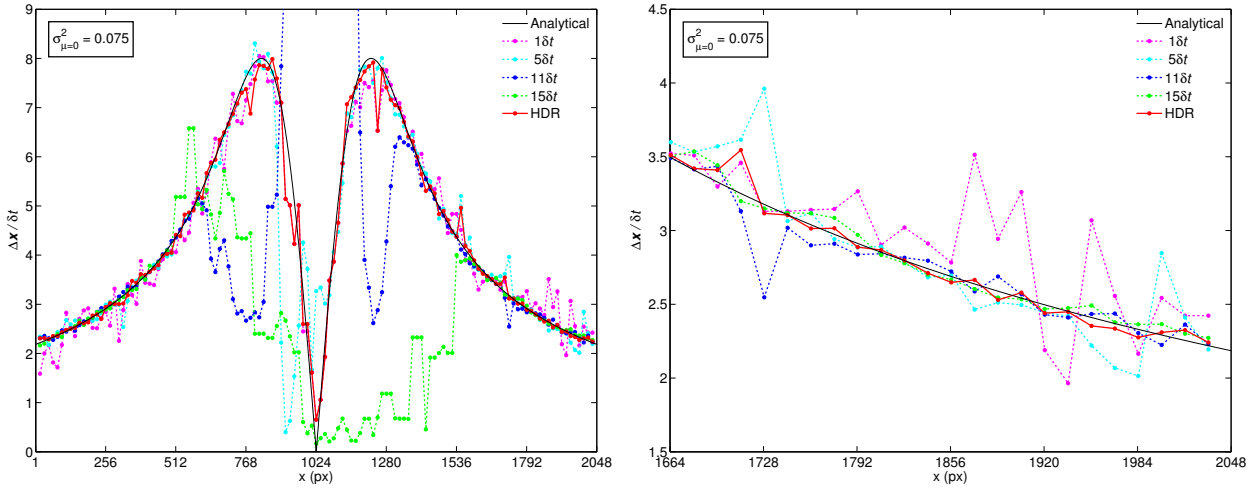

(a) Velocity profile for the central, horizontal slice (b) Enlarged view of the region indicated by the axes

Figure 4.17: Results achieved for the central velocity profile by the image sequence with $\sigma^2_{\mu=0} = 0.075$. Plots are shown that contain the entire velocity profile (a) as well as an enlarged view of the region indicated by the axes (b). The HDR result performed significantly better than the individual correlation results for almost all cases.

The plots included in figure 4.17 correspond to the HDR result for $\sigma^2_{\mu=0} = 0.075$. As before, figure 4.17(a) contains the entire velocity profile, whereas figure 4.17(b) shows an enlarged view of the region indicated by the axes. Considering both plots, the HDR result follows the velocity profile of the analytical solution rather closely at most spatial locations aside from a few apparent blips near the core. This trend is encouraging since unlike the previous noise investigation where only the image pairs spanning the largest temporal distances displayed significant deviations, small blips are evident in all of the individual correlation results over much of the velocity profile (figure 4.17(a)). Thus it appears that the Gaussian white noise, at least for the variances considered, had a much more profound effect on the individual correlation results and consequently the DEVOLS processing scheme than did the salt and pepper noise. Nevertheless, as is evident in the enlarged view, the HDR result still performed considerably better at most spatial locations than did the individual correlations.

Chapter 5

Experimental Results

Using the DEVOLS processing scheme described in the previous chapter, measurements for the near-nozzle velocity field considered during the experimental investigation were able to be obtained. Due to the poor quality of the experimental data and consequently the HDR results though, only a few select measurements are shown. The first section describes the preprocessing steps that were taken before each particle-image sequence was analyzed. Such steps included a dark-frame subtraction for noise removal as well as a spatial transformation for improved channel alignment. Sample velocity-field measurements achieved via these steps and the employed DEVOLS procedure are then presented in the second section. As mentioned however, only a few measurements are shown due to the subpar quality of these results. To better characterize the effectiveness of the DEVOLS algorithm as applied to a supersonic, shock-containing jet, synthetic particle-image sequences resembling the ones acquired during the experimental investigation were considered. The final section describes how these sequences were able to be generated and includes results corresponding to two spatial locations in the jet, namely the region immediately following the nozzle exit as well as the region encompassing the potential core collapse.

5.1 Image preprocessing

To prepare each particle-image sequence for the correlation analyses and the ensuing DEVOLS procedure, several image preprocessing and enhancement steps were performed. Such steps included a dark-frame subtraction to remove fixed-pattern noise as well as a spatial transformation to better align the eight independent camera channels. The noticeable improvements from these steps enabled significantly better displacement measurements to

be achieved. Because the spatial transformations played a significant role in quantifying the errors associated with the experimental results, in-depth discussion on this topic is saved for the following chapter. Only the dark-frame subtraction step is described in detail below.

Dark-frame subtraction is a common processing step in scientific, digital-imaging applications to remove or minimize the fixed-pattern component of image noise (hot pixels, dead pixels, dark current, etc.). Because such noise does not vary appreciably from one image to the next for a given sensor, it can easily be removed via subtraction. To ensure that the noise represented by a dark frame is comparable to the noise actually found in an image, dark frames are acquired using the same camera settings as employed during the experiments albeit with zero collected signal. In other words the exposure time for dark frames remains the same, however the sensor is not exposed to light. Furthermore, to avoid potential differences in the fixed-pattern component of image noise due to differences in the operational conditions of the camera, dark frames are generally acquired either immediately before or immediately after an experimental data set. For the experiments of interest approximately 25 dark sequences were acquired at the end of each data acquisition period.

To begin the preprocessing steps, image sequences were first corrected by subtracting the average of 25 dark frames from only the corresponding image frames. Because each sensor is subject to its own fixed-pattern component of image noise, images acquired by different sensors were processed separately. Thus only the images acquired by sensor 1 were corrected by subtracting the average of the 25 dark frames also acquired by sensor 1. In a similar fashion, exposures A and B for a given sensor were processed separately. As a reminder, each of the 8 sensors recorded 2 images (A and B) such that a total of 16 images were obtained for a given sequence. By generating an average dark frame, or *master dark*, the noise subtracted from each image was more representative of the fixed-pattern component of image noise inherent to that particular sensor and exposure (since averaging increases the signal-to-noise ratio). Thus the variable component of image noise was minimized in each master dark before the ensuing dark subtractions were performed.

Following the dark-frame subtractions, spatial transformations were applied to each image to correct the slight misalignments between channels. Such misalignments are unavoidable in the Cordin setup since each CCD sensor effectively acts as its own, independent camera. Achieving precise alignments between the channels is critical because apparent particle displacements caused by the sensor misalignments are perceived as actual particle motions in the correlation analyses. Thus even the slightest differences between channels, if not accounted for, can produce substantial errors in the velocity-field measurements. As mentioned, detailed discussion regarding the applied spatial transformations is given in the following chapter. For the purposes of this section it is sufficient to note that eight image transform functions, one for each of the eight camera channels, were determined by quantifying the discrepancies between acquired calibration target images and an ideal, virtual, calibration target image. Channel misalignments were then corrected by applying these transform functions to all of the corresponding images. Sample particle images that have been dark-subtracted as well as spatially transformed are shown in figure 5.1.

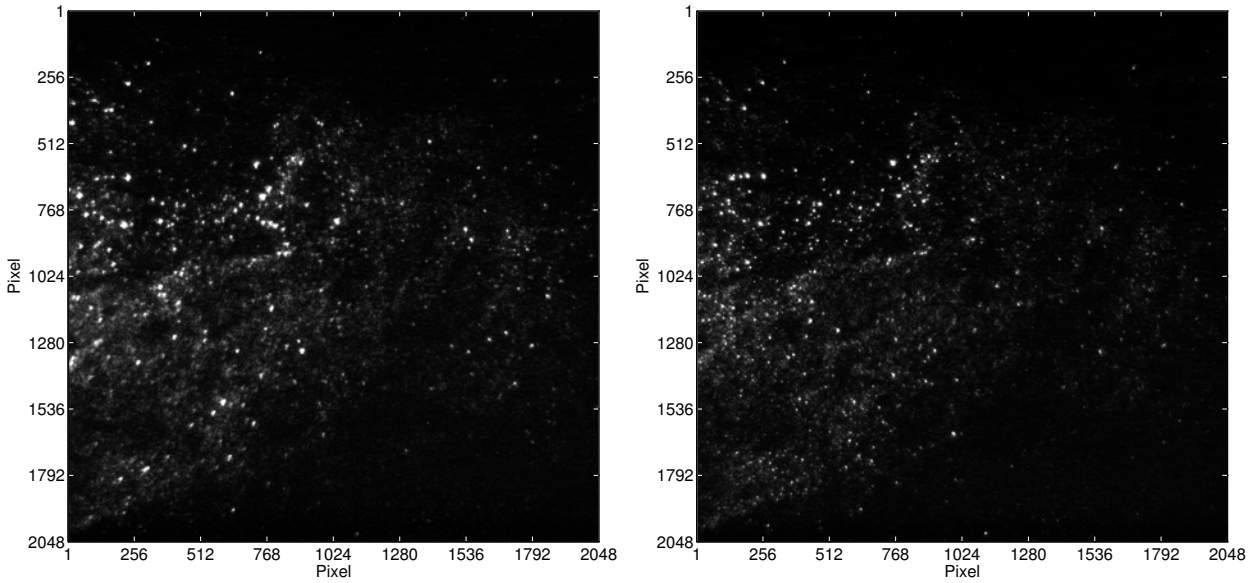

(a) Particle image 2 of 16

(b) Particle image 4 of 16

Figure 5.1: Particle images acquired in a high-temperature (1350°F), Mach 1.55 jet using the Cordin camera. The particles recorded in each image are aluminum oxide particles nominally 0.3 μm in diameter. Both images have been dark-subtracted as well as spatially transformed.

5.2 Experimental jet results

After applying the preparatory steps described in the previous section, velocity-field measurements were able to be obtained by employing the DEVOLS processing scheme. As before, Dantec DynamicStudio v3.31 software was used to perform all correlation analyses. Due to the increased particle size as well as the reduced particle density found in the images, 128×128 px^2 interrogation windows were specified with a 75% overlap. For the DEVOLS procedure, maximum particle displacements of 48 pixels and 112 pixels were specified in the first and second passes, respectively, along with an R^2 tolerance of 0.8. A relaxed tolerance was chosen based on the poor correlation results. The plots shown in figure 5.2 correspond to the HDR results obtained for one of the better sequences acquired during the experimental investigation. The axial and radial spatial positions, in terms of jet diameters, are referenced from the nozzle exit plane and the jet centerline, respectively. As an aside, the sample particle images shown in figure 5.1 were part of the sequence used to achieve these results.

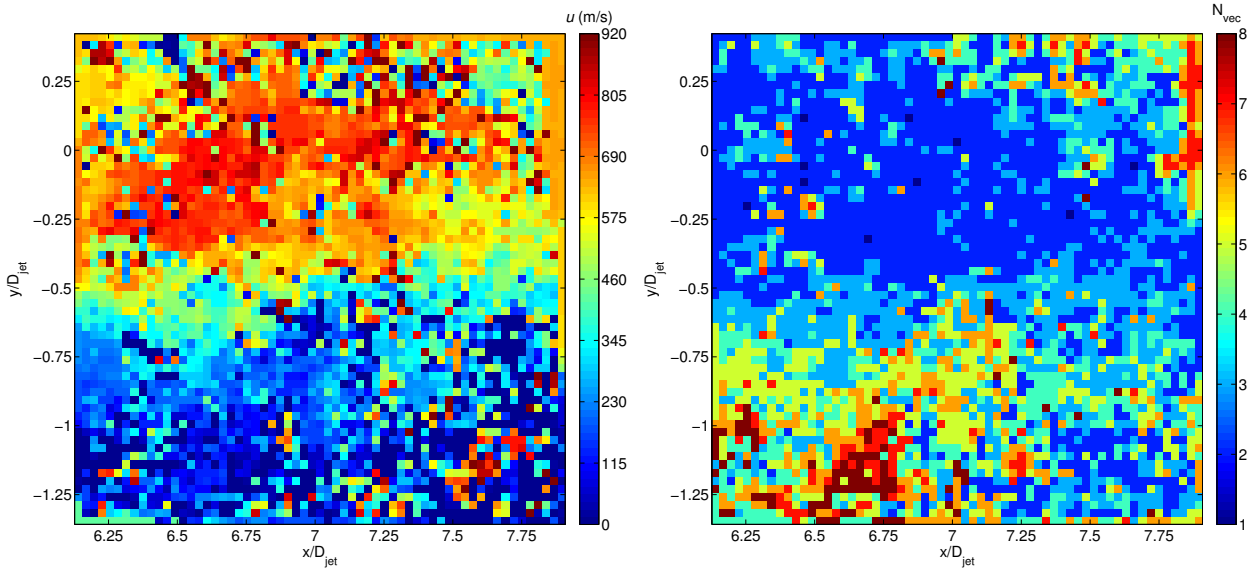

(a) Streamwise velocity for the HDR result

(b) Vectors considered per spatial location

Figure 5.2: HDR results for the velocity field considered during the experimental investigation. Although the quality of these results is poor, the DEVOLS processing scheme appears to have functioned correctly. Considering the vector evaluation field in (b), the algorithm appropriately utilized an increased number of displacement results to assess the low-velocity regions. Contrarily only a few displacements were used to determine velocities in the jet.

The plots shown in figure 5.2 correspond to the streamwise velocity field and the vector evaluation field, respectively, for one of the better HDR results. While the high-velocity regions inside the jet can be distinguished from the low-velocity regions outside the shear layer, nothing of quantitative value can be said regarding flow-structure evolution or the potential core collapse (at least nothing definitive). Despite such poor quality, the DEVOLS processing scheme appears to have functioned correctly regarding the number of displacement measurements utilized to achieve each local velocity result. Considering the vector evaluation field in figure 5.2(b), the algorithm performed as expected for the two velocity extrema. As is evident, only a few displacement measurements were considered in the high-velocity regions located within the jet. Contrarily an increased number of measurements were utilized in the low-velocity regions outside the shear layer. The worst-performing region appears to be the bottom-right corner where the fewest number of particles were observed.

Without question the substandard results of the correlation analyses are due in large part to the poor quality of the underlying particle-image sequences. At present the primary cause of such lackluster data appears to be two-fold. On one hand a very inconsistent seeding mechanism was utilized to supply the jet flow with particles. In most cases only a handful of particles were visible across the 16 frames of a sequence. This extremely low particle density limited the maximum achievable spatial resolution in the measurements and proved to be insufficient for obtaining high-accuracy results. Moreover, when higher particle densities were observed in the images, they generally appeared as thick clouds such that resolving individual particles was not possible. The cause of both the lack of particles in most image sequences as well as the occasional over-saturations in others is believed to be blockages in the particle seeding tubes. These tubes extended from the particle-containment reservoir to various attachment points on the burner system as described in chapter 3. The few sequences containing substantially increased particle densities are thought to coincide with blockages being cleared in one of more of the seeding lines.

On the other hand slight variations in focus between the eight optical pathways of the camera were evident in the images. When one or more of the channels appeared to be in good focus with the particles, other channels appeared slightly out-of-focus. Although this problem was not resolved before the completion of testing, the issue is now known to stem from acoustically induced vibrations. The high sound levels (∼140 dB) in the vicinity of the jet caused vibrations in the internal optics of the camera, specifically the beam splitters, which resulted in focus differences between the various particle images. Consequently the correlation results achieved by the Dantec software between in-focus and out-of-focus images were very poor. This effect was compounded by the fact that only symmetrically centered image pairs were used by DEVOLS. Because each sensor recorded two images, and no two images from the same sensor were symmetric about the central image pair (frames 8 and 9), every out-of-focus channel resulted in two unsatisfactory correlation results. Thus only two out-of-focus channels were required to impair half of the correlation results. Sample in-focus and out-of-focus particle images are shown in figure 5.3.

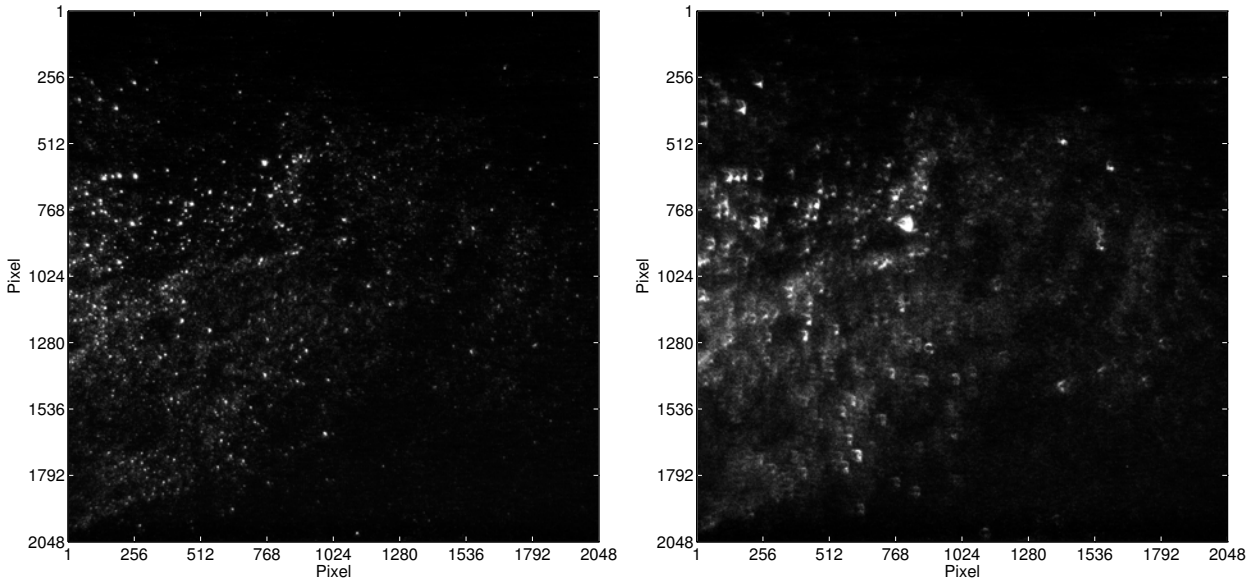

(a) In-focus particle image

(b) Out-of-focus particle image

Figure 5.3: In-focus and out-of-focus particle images acquired in the same sequence. Because these images were recorded only 1 μs apart, the same particles should be visible in each image and in roughly the same positions. As is evident, the differences in focus severely limited the experimental image quality and consequently the accuracy in the correlation results.

Despite the poor quality of the experimental data and consequently the HDR results, one additional measurement is included as a proof-of-concept. The plots presented in figure 5.4 on the following page represent an HDR result obtained with just four particle images. For this case only frames 1, 2, 3, and 4 of exposure A were considered such that the velocity field temporally located between frames 2 and 3 was characterized. As is evident, the ability to selectively utilize different sets of images within the DEVOLS algorithm to achieve velocity fields at different points in time is clearly demonstrated. It should be mentioned, however, that significant amounts of post-processing were required to achieve the streamwise velocity contours shown. Thus while no conclusive statements can be made regarding the quantitative nature of these plots, such results provide a nice representation, at least in a qualitative sense, of the near-nozzle velocity field considered during the experimental investigation. Steps to improve the quality of the experimental images and their corresponding particle-image displacements are provided in chapter 7. Several significant upgrades, most notably ones regarding the PIV system, are either currently underway or have already been completed.

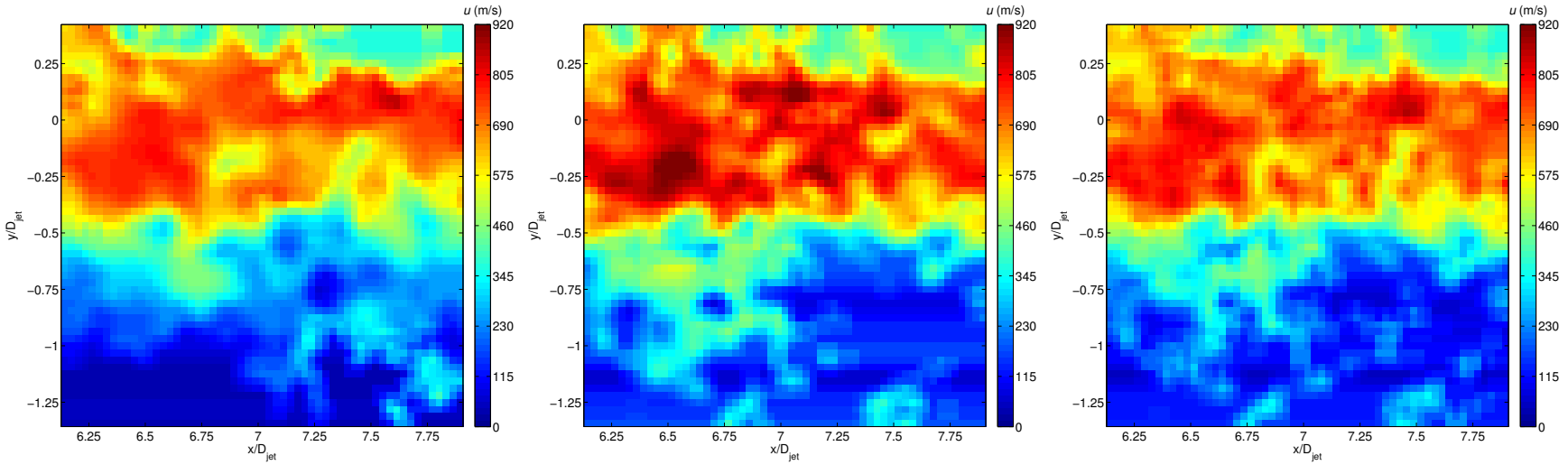

(a) Streamwise velocity for A1A4 ($3\,\delta t$)

(b) Streamwise velocity for A2A3 (δt)

(c) Streamwise velocity for the HDR result

Figure 5.4: Results for the near-nozzle velocity field considered during the experimental investigation. In all cases the contour coloring scheme is indicative of the streamwise velocity. The HDR result in (c) was obtained by using only those measurements contained in (a) and (b). Due to the significant amounts of post-processing required to achieve these results, each plot should only be viewed in a qualitative sense. Nevertheless, the ability to selectively utilize different sets of image pairs within the DEVOLS processing scheme is clearly demonstrated.

5.3 Synthetic jet results

Although the DEVOLS processing scheme is applicable to any flow field containing a wide velocity range (assuming a temporally resolved image sequence can be obtained), the motivation behind the procedure stems largely from the experiments of interest. Thus to better characterize the effectiveness of the DEVOLS algorithm as applied to a supersonic, shock-containing jet, synthetic particle-image sequences resembling the ones acquired during the experimental investigation were considered. For these sequences the particle displacements were generated using the velocity-field results of a previously conducted, large eddy simulation (LES) analysis[1].[39, 40] Without going into detail, LES is a CFD technique in which only the largest scales of fluid motion are explicitly resolved.[41] By filtering the smaller turbulent lengths and approximating their effects using subgrid scale models, the computational cost incurred by the smallest flow scales can be significantly reduced[2].

To achieve the necessary particle-displacement information utilized by the synthetic image generator, the specified nozzle configuration and operational conditions in the LES simulation were exactly those considered during the experimental investigation. Thus a shock-containing jet emanating from a conical C-D nozzle with an upstream centerbody section was generated with an exit jet diameter (D_{jet}) of 2 inches and an exit Mach number of 1.55. Then, by using the temporally resolved, velocity-field measurements from the LES calculations to generate the particle motions across a given number of images, very realistic albeit synthetically generated TR PIV data was able to be obtained. Furthermore, by limiting each sequence to only 16 images with a specified resolution of 2048×2048 px^2, the data resembled exactly that acquired by the Cordin camera (albeit without the problems described previously).

[1]The LES data was provided by CRAFT Tech®, a small and well-established R&D business that specializes in the numerical modeling of aero-propulsive flow fields. This group was uniquely qualified to collaborate on the experimental investigation since they have prior experience modeling the NCPA nozzle setup.

[2]The computational cost associated with LES is greatly reduced from direct numerical simulation since the entire range of turbulent length scales is not resolved. Nevertheless, LES techniques still require an increased number of computational resources compared to Reynolds-averaged Navier-Stokes methods.

The following subsections contain sample results achieved at two spatial locations in the synthetically generated jet, namely the region immediately following the nozzle exit as well as the region encompassing the potential core collapse. For both cases the velocity data was scaled such that the maximum flow velocity in the jet, not necessarily the maximum flow velocity in each region of interest, corresponded to a maximum particle displacement of 8 pixels. In addition, the particle density was chosen to achieve approximately 24 particles in each 32×32 px^2 interrogation window. Such windows were specified with a 50% overlap during the correlation analyses. Again, all correlations were performed using the software provided by Dantec. Lastly, only zero-noise conditions were simulated in the images. Thus each sequence represented the ideal case for data acquired by the Cordin camera.

5.3.1 Nozzle exit

The plots shown in figure 5.5 represent conventional PIV results achieved for the nozzle exit. From top to bottom these results correspond to the image pairs spanning δt and $15\,\delta t$, respectively. In both cases a velocity magnitude plot is presented on the left, and its associated absolute error is given on the right. Considering the absolute error results, the larger interframe time was unable to resolve the turbulent shear layers of the jet due to the increased levels of fluid entrainment and mixing (i.e., particle accelerations). Thus the time scales associated with the velocity fluctuations in these regions were considerably less than the temporal spacing between the two images. This effect is evident in the corresponding velocity magnitude plot (figure 5.5(c)) given the overall smoothness in appearance.

Based on these results, one would expect the turbulent shear layers in the HDR result to be characterized almost exclusively by the image pairs spanning the smallest interframe times. Considering figure 5.6, this exact trend is observed. As before, the velocity magnitude field associated with the HDR result is presented on the left. For this case, however, a vector evaluation field rather than an absolute error plot is given on the right. As is evident, only the low-velocity regions outside the jet shear layers were assessed by all available image pairs.

Contrarily less than half of the image pairs were used to characterize the jet. The remaining individual correlation results as well as additional HDR results are presented in appendix E.

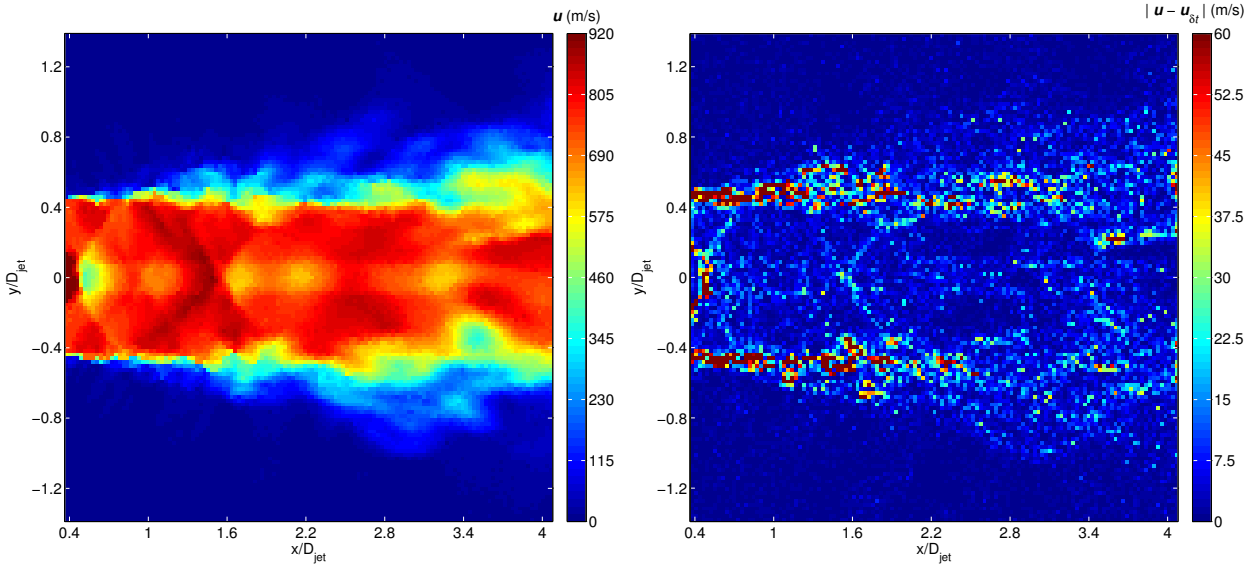

(a) Velocity magnitude field for δt

(b) Absolute error from the analytical solution

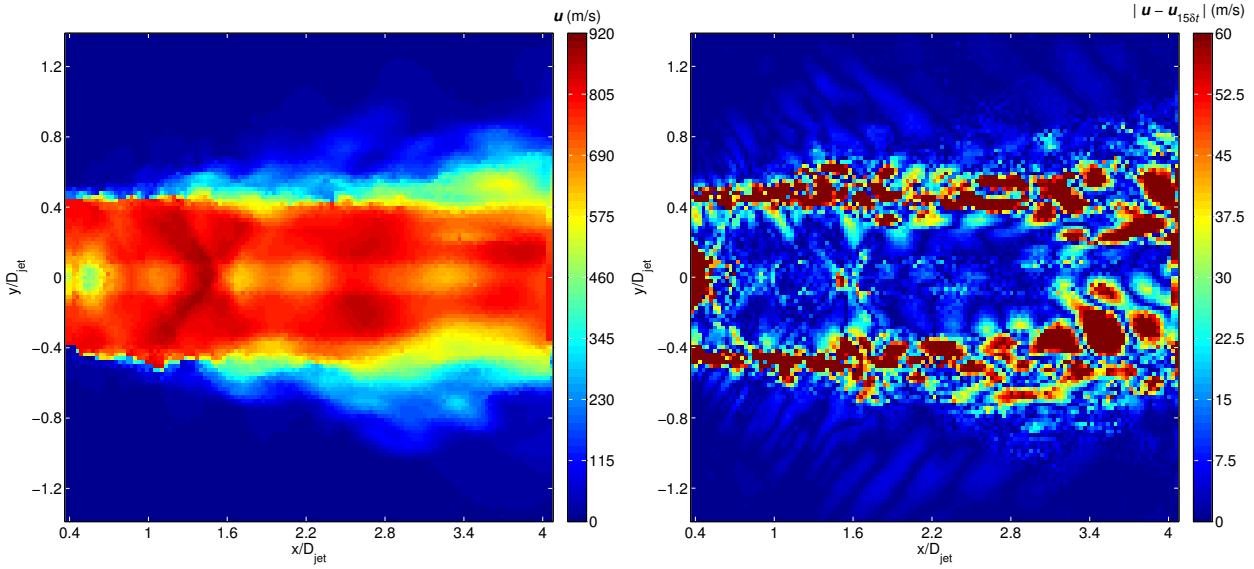

(c) Velocity magnitude field for $15\,\delta t$

(d) Absolute error from the analytical solution

Figure 5.5: Velocity magnitude fields and corresponding absolute errors for the image pairs spanning δt and $15\,\delta t$, respectively. As is evident by the absolute error plot in (d), the larger interframe time is insufficient to resolve the velocity fluctuations that exist in the shear layers of the jet. Thus the corresponding velocity magnitude field in (c) appears smooth. The contour coloring scheme in all plots is indicative of the local velocity magnitude in m/s.

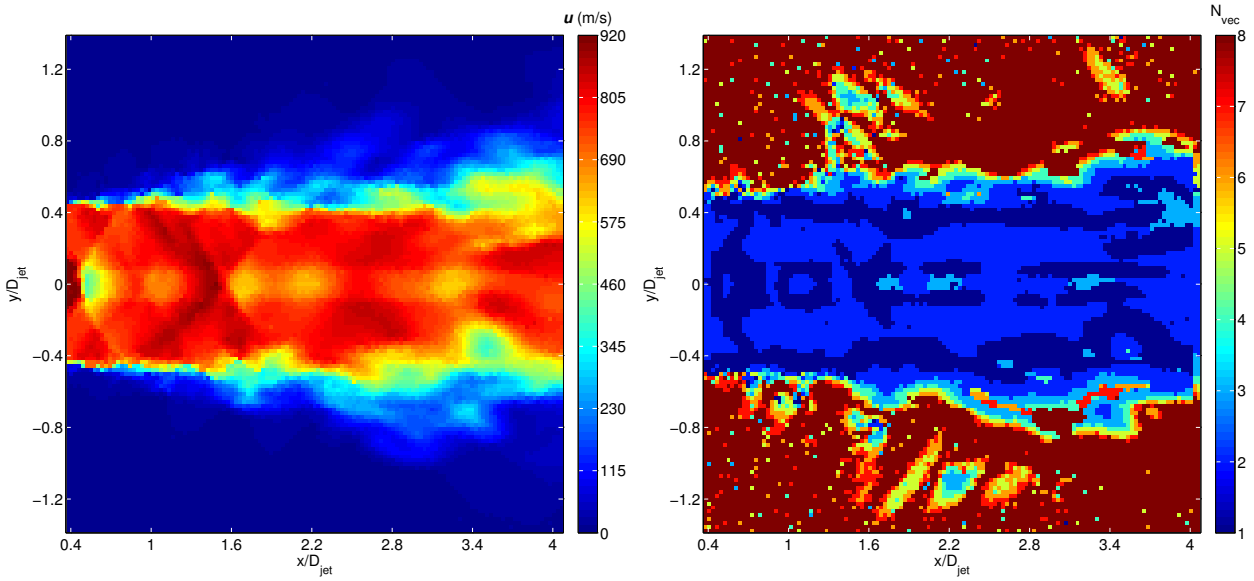

(a) Velocity magnitude field for the HDR result

(b) Vectors considered per spatial location

Figure 5.6: HDR results for the nozzle exit of the synthetically generated jet. The vector evaluation field in (b) indicates the number of displacement measurements considered at each spatial location to determine the local velocity. As is evident, only the smallest interframe times were capable of resolving the high-velocity/high-acceleration regions in the jet.

5.3.2 Potential core collapse

Following the same presentation layout as employed in the previous subsection, the plots in figure 5.7 represent conventional PIV results achieved for the potential core collapse. Similarly as before, the velocity magnitude fields (left) and their associated absolute errors (right) correspond to the image pairs spanning δt and $15\,\delta t$, respectively. Considering the absolute errors, the inability of the larger interframe time to accurately resolve regions of high particle acceleration is more obvious here than in the previous case. The reason is because as the potential core collapses, the uniform flow along the jet centerline is subjected to increasing levels of turbulent fluctuations. Thus flow instabilities previously confined to only the turbulent shear layers are now prevalent throughout the entire flow field.

The HDR results achieved for this region are shown in figure 5.8. Again, the velocity magnitude field and its corresponding vector evaluation field are presented on the left and right, respectively. Without going into detail, the observed trends from the previous case

are also evident in this one, namely the turbulent flow regions associated with the jet are only assessed by the image pairs spanning the shortest interframe times. Additional results for the individual correlations as well as the HDR measurement are provided in appendix F.

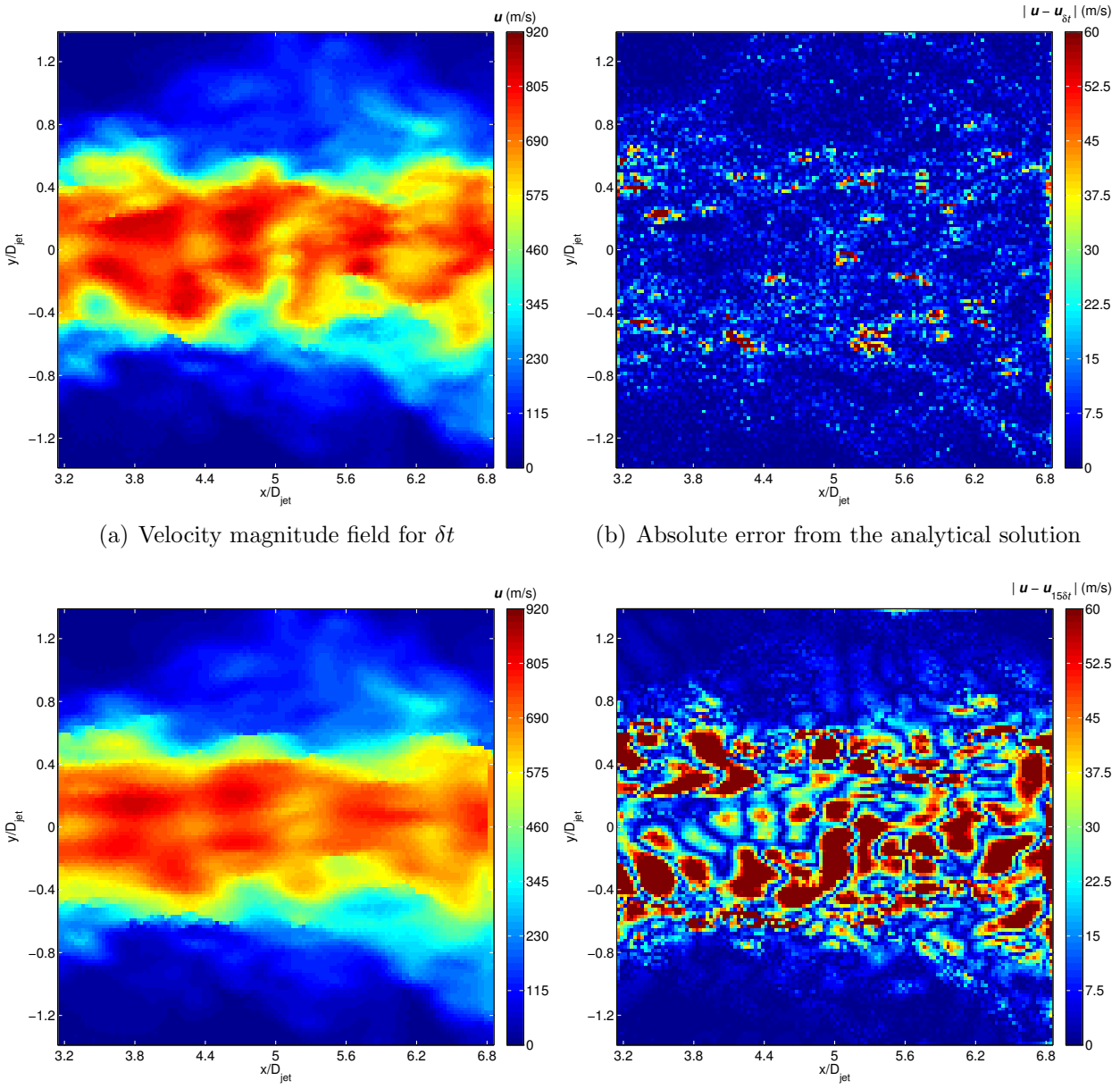

(a) Velocity magnitude field for δt

(b) Absolute error from the analytical solution

(c) Velocity magnitude field for $15\,\delta t$

(d) Absolute error from the analytical solution

Figure 5.7: Velocity magnitude fields and corresponding absolute errors for the image pairs spanning δt and $15\,\delta t$, respectively. As is evident by the absolute error plot in (d), the larger interframe time is insufficient to resolve the velocity fluctuations that exist throughout the jet. Thus the corresponding velocity magnitude field in (c) appears quite smooth. The contour coloring scheme in all plots is indicative of the local velocity magnitude in m/s.

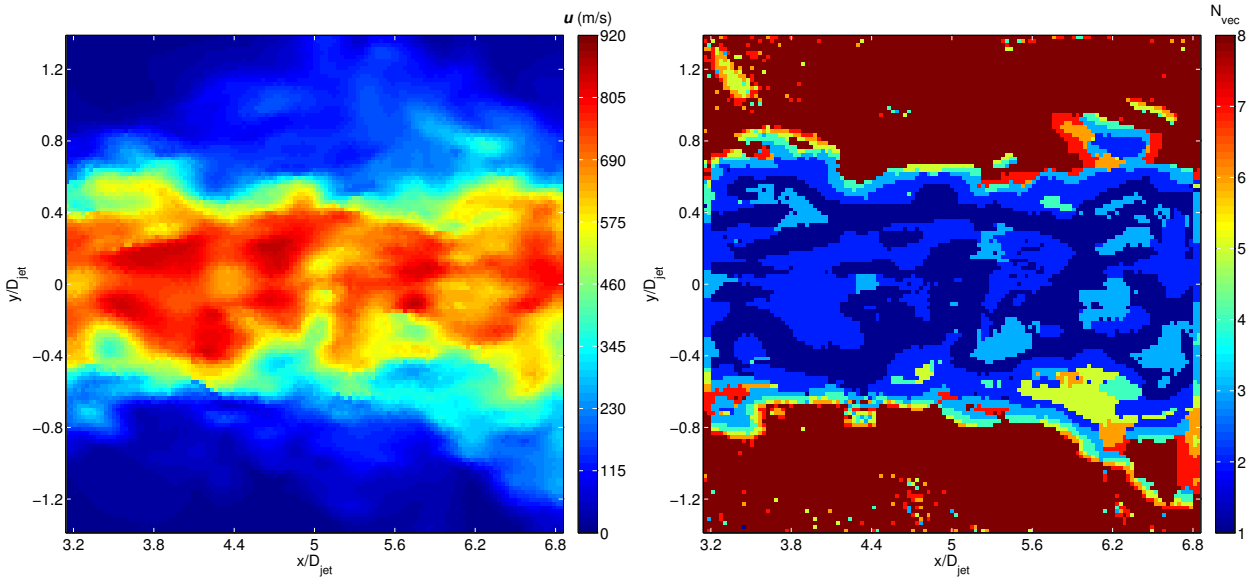

(a) Velocity magnitude field for the HDR result

(b) Vectors considered per spatial location

Figure 5.8: HDR results for the potential core collapse of the synthetically generated jet. The vector evaluation field in (b) indicates the number of displacement measurements considered at each spatial location to determine the local velocity. As is evident, only the smallest interframe times were capable of resolving the turbulent fluctuations inside the jet.

Chapter 6

Experimental Error Analysis

Zero-time-displacement (zero-δt) images were used to quantify the measurement errors present in the experimental results. Such images were obtained by simultaneously exposing the camera's 8 CCDs over a 0.75 μs exposure time to the same particle field[1]. Because particle motions under these circumstances should be nonexistent, any discrepancies between images are directly attributable to error. This error limits the maximum achievable accuracy in the PIV results and is comprised of both a systematic and a random component.[42] The systematic or bias error between any two channels is found by calculating the average particle displacement between the zero-δt images. Once found this component is correctable in the experimental results since particle motion due to misaligned channels represents a repeatable source of error. The random error is determined by computing the standard deviation in the bias error measurements. As such it provides a true measure of uncertainty in the PIV results. The computational procedure used to determine both of these error components is described in the sections below. Values for select image pairs are given in the final section.

6.1 Mapping particle images to a virtual image

Before the average particle motions or bias errors are determined, each particle image is spatially transformed according to a CCD-specific transform function. Such transformations serve to better align the eight independent camera channels and thus significantly reduce the particle jitter. A schematic illustrating the procedure for generating each spatial transform function is shown in figure 6.1. For each channel an average calibration target image is first

[1]The particle field considered in this error analysis was imaged at the identical test position and over-expanded conditions as the experimental results. Thus only the individual channel delays were adjusted prior to the acquisition of the zero-time-displacement images.

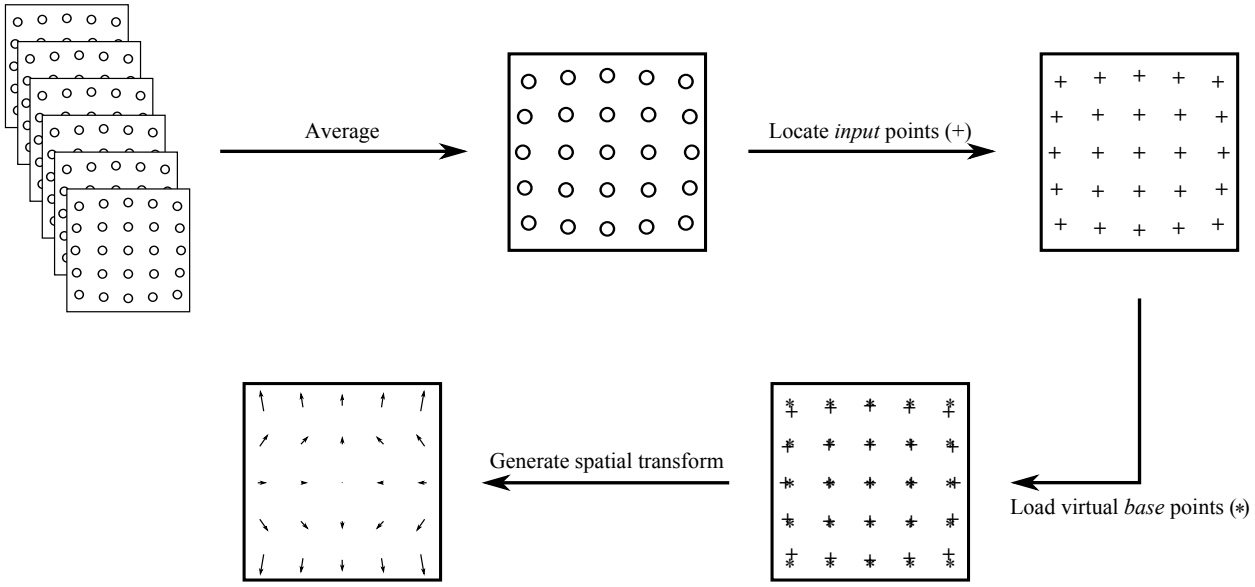

Figure 6.1: Flowchart illustrating the procedure for generating a CCD-specific transform function. Eight total functions were generated for the eight independent camera channels.

computed using 30 total images (15 calibration sequences were acquired in which each sensor recorded 2 images). The central position of each calibration dot is then determined based on a circular Hough transform that relies on the gradient field of the image.[43] Sample results illustrating the dot positions detected for channels 2 and 4 are shown in figure 6.2.

To generate the transform function for each channel, the detected dot positions or *input* points are mapped to specified *base* points in a synthetic, virtual image. This virtual image is created based on the known magnification of the camera as well as the known dot spacings on the actual calibration target. To ensure that satisfactory alignment corrections are achieved, the input points determined for each channel are mapped to the same, virtual base points. Figure 6.3(a) contains all of the input points detected for each channel as well as the specified, virtual base points. An enlarged view of the region enclosed by the dashed box is shown in figure 6.3(b). The position of the base point in figure 6.3(b) is specified to be the average position of the eight input points detected at that location. Using this position as a reference, the remaining base points are specified according to the known magnification and the known dot spacings as previously mentioned.

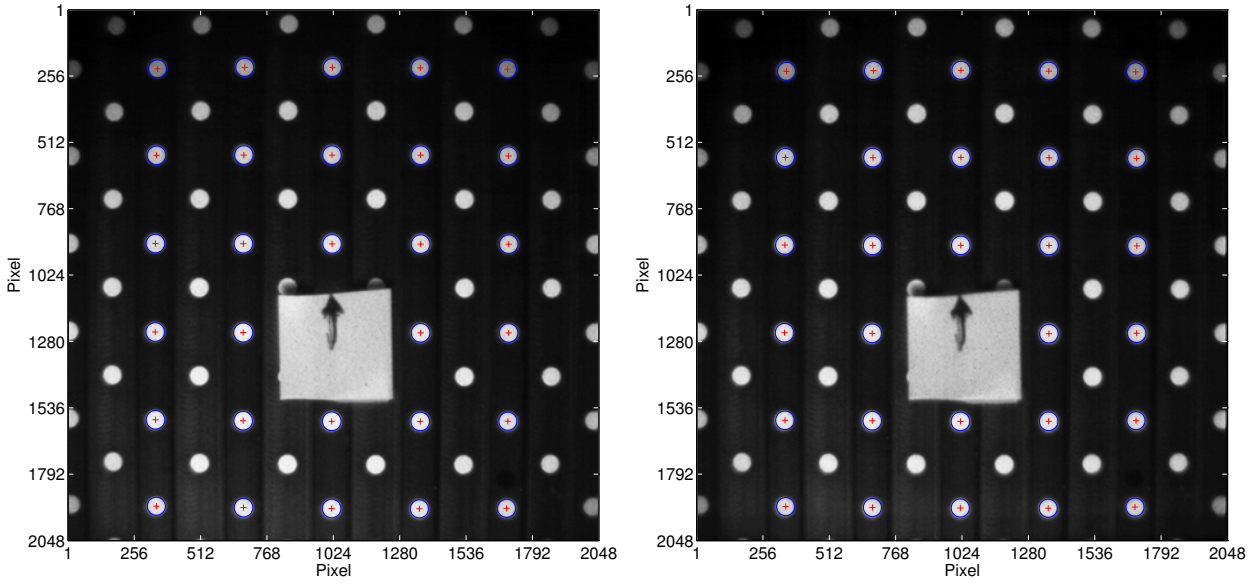

(a) Dot positions determined for channel 2 (b) Dot positions determined for channel 4

Figure 6.2: Central dot positions determined for two of the eight average calibration target images. Because the actual calibration target contained two different surface levels, only dots located within the image focal plane were considered during the analysis procedure. Thus 29 total dot positions were available for each average calibration target image. For clarification, the arrow present in each image is not associated with the calibration procedure.

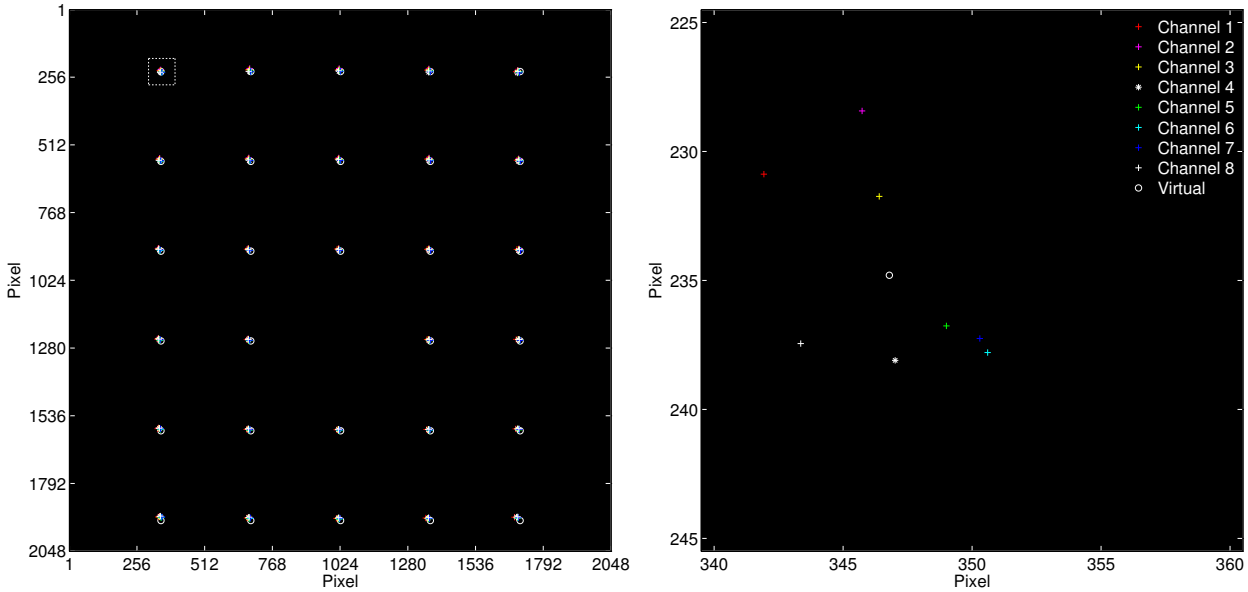

(a) Determined input points relative to base points (b) Enlarged view of the enclosed region in (a)

Figure 6.3: Positions of the input points for all channels relative to the virtual base points before spatial transformations have been applied.

Using the spatial information provided by the input and virtual base points, a third-order polynomial routine is specified inside the MATLAB function **cp2tform** to generate the spatial transformation for each channel. A bilinear interpolation scheme is then employed by the MATLAB function **imtransform** to actually transform each zero-δt image according to the correct transform function. Figure 6.4 shows the input points for all channels relative to the virtual base points once these spatial transformations have been applied.

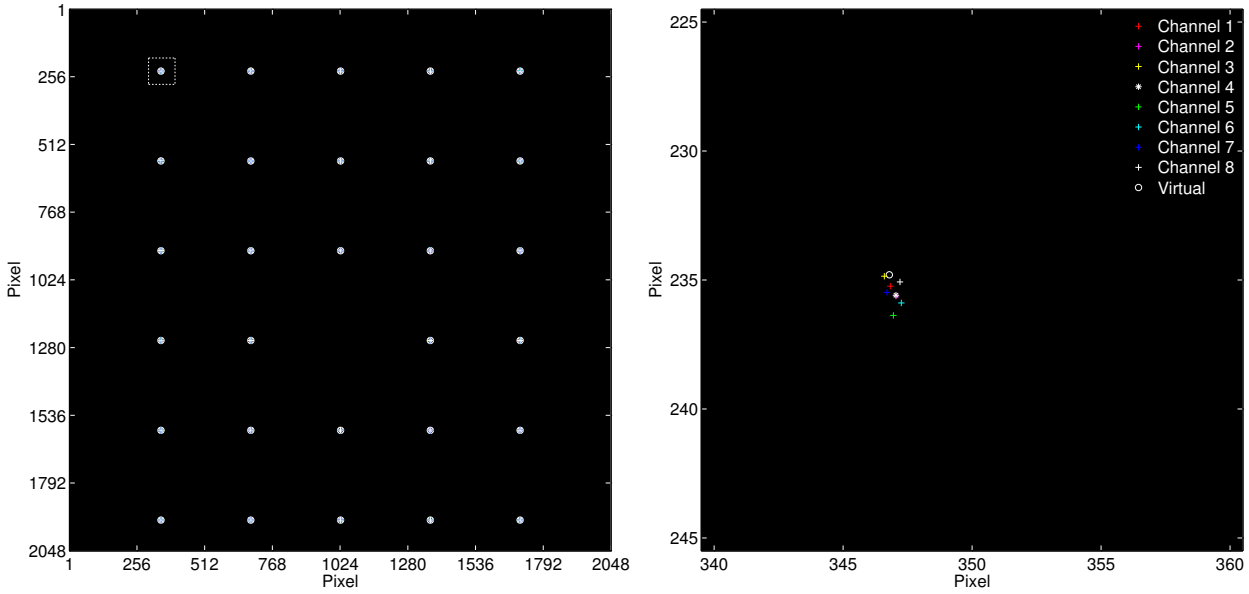

(a) Transformed input points relative to base points (b) Enlarged view of the enclosed region in (a)

Figure 6.4: Positions of the input points for all channels relative to the virtual base points after spatial transformations have been applied.

6.2 Filtering particle displacements using median statistics

Once each zero-δt image has been corrected by its particular spatial transform function, cross-correlation analyses are performed to determine the remaining discrepancies between images. These discrepancies or slight particle displacements correspond to the bias errors that can be corrected between any two channels. The standard deviations in these bias errors represent the random errors and thus uncertainties present in the actual velocity measurements. The schematic shown in figure 6.5 illustrates the procedure for determining the bias error at a single vector position for one of the possible image-pair combinations.

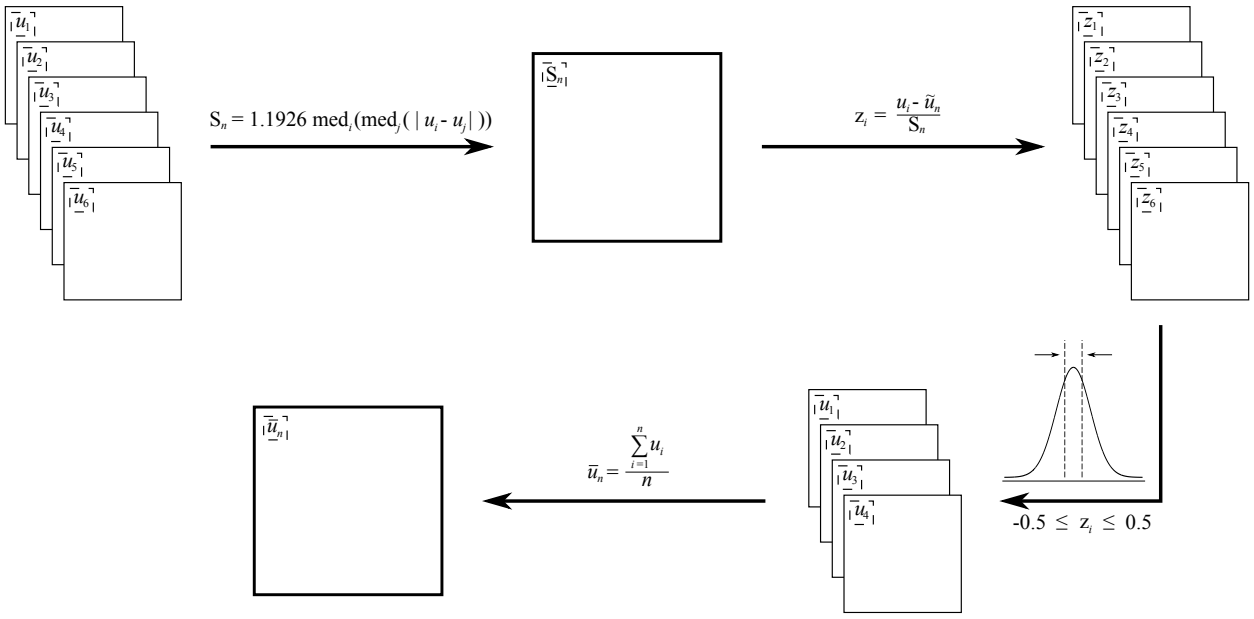

Figure 6.5: Flowchart illustrating the procedure for determining the bias error at a single vector position. Almost 4000 positions were considered during the actual analysis.

As is evident from the schematic, median rather than mean statistics are used to filter the data for outliers. The reason is because the median is a robust measure of central tendency, whereas the mean is not. Thus outliers and long tails in the data distributions have no significant influence over the statistical results. The estimator used in this analysis, known as the S_n estimator, is a robust measure of statistical dispersion and consequently is more resilient to outliers than classical estimators such as standard deviation. The S_n estimator was chosen for use over other robust measures of scale, such as median absolute deviation (MAD), due to its increased level of statistical efficiency (58% for S_n to 37% for MAD) and better handling of data skewness.[44]

For each vector position a single S_n value is calculated from the displacement results of the correlation analyses. Once this value has been determined, each displacement measurement is given a modified z-score by subtracting the median of the data and dividing by the S_n value. Using these scores, outliers are deemed any measurement falling outside the range $[-0.5\ 0.5]$. Any remaining, valid measurements are then averaged to determine the local bias error or average displacement at that position. In appendix G, the error plots

labeled (a) represent the local bias errors determined for the symmetrically centered image pairs utilized in the DEVOLS processing scheme.

To determine the overall bias error, the local bias errors for all positions are averaged. In performing this average, one inherently assumes that all locations across a given vector field exhibit the same, average displacement. This assumption is warranted since the alignment issues known to produce variations in the local bias errors (rotation, warping, etc.) have already been corrected via the spatial transformations. Furthermore, by treating the local bias errors as a distribution about some mean, the data can be filtered similarly as before with only those values falling within a specified range actually contributing to the final result. In this case outliers are deemed any measurement falling outside the z-score range $[-3.0\ 3.0]$. Removing these measurements provides the filtered plots shown in appendix G with label (b). The plots labeled (c) indicate the number of displacement measurements considered at each position to determine the local bias error and thus the overall bias error. Positions with z-scores not falling within the $[-3.0\ 3.0]$ range are shown with a value of 0. As an aside, these contour plots also provide a qualitative representation of the underlying particle distributions in the zero-δt images since the areas containing sufficient particle numbers are more likely to produce valid results and thus more likely to be included in the bias error measurements. The fact that an uneven distribution is observed for all cases that is heavily concentrated towards the center suggests possible vignetting in the particle images.

Finally, the standard deviation about the overall bias error represents the random component of error. As mentioned, this component contributes significantly to the uncertainty in the correlation analyses since apparent particle displacements due to channel misalignments and actual particle displacements due to fluid motions cannot be differentiated. In fact, unless the random error is known to a precision less than 0.1 pixels (the value widely accepted as the minimum resolvable displacement limit in state-of-the-art PIV software), the overall measurement accuracy is entirely limited by the extent to which the individual channels can be aligned. In the following section, the bias errors and uncertainties associated with the

displacement measurements in the horizontal (u_i) and vertical (u_j) directions are presented for several image pairs.

6.3 Systematic and random error results

Table 6.1 provides the systematic and random error results for the symmetrically centered image pairs utilized in the DEVOLS processing scheme. As mentioned, the systematic error corresponds to the correctable, bias component between any two channels. Contrarily the random error represents the alignment uncertainty that contributes to the overall uncertainty in the correlation analyses. Because the random component shown for all cases is significantly greater than the minimum resolvable displacement limit achievable by the Dantec software, this component is indicative of the maximum-achievable accuracy in the velocity-field measurements. It should be mentioned, however, that the poor image quality obtained in the zero-δt images (similarly to the experimental data) severely limited the viability of this error approach.

Table 6.1: Systematic and random error results for the specified image-pair combinations.

Image pair 1–8:	Image pair 5–4:
u_i : 8.989 ± 4.888 pixels	u_i : 0.857 ± 1.670 pixels
u_j : 0.855 ± 4.320 pixels	u_j : −1.737 ± 1.814 pixels
Image pair 2–7:	Image pair 6–3:
u_i : 2.457 ± 1.980 pixels	u_i : −1.709 ± 2.639 pixels
u_j : −0.729 ± 2.084 pixels	u_j : −1.772 ± 2.874 pixels
Image pair 3–6:	Image pair 7–2:
u_i : 2.083 ± 2.440 pixels	u_i : −2.302 ± 2.091 pixels
u_j : 4.882 ± 3.023 pixels	u_j : 3.337 ± 2.093 pixels
Image pair 4–5:	Image pair 8–1:
u_i : −0.795 ± 1.660 pixels	u_i : −8.736 ± 4.853 pixels
u_j : 4.217 ± 2.113 pixels	u_j : 2.997 ± 3.884 pixels

Chapter 7

Concluding Remarks

The development, validation, and application of a novel HDR processing scheme to supplement conventional PIV algorithms have been presented. As mentioned, the motivation behind such work was the experimental investigation of a high-temperature, shock-containing jet using TR PIV measurements. The processing scheme, termed dynamic evaluation via ordinary least squares (DEVOLS), offers substantial improvements over conventional PIV methods for its ability to increase the dynamic velocity range and its enhanced robustness in the presence of noise. Unique to this approach is an iterative validation scheme that enables a variable number of displacement measurements to be utilized in the determination of a single velocity vector. This feat is accomplished by fitting an ordinary least squares regression line to all displacement measurements satisfying a maximum displacement criterion at a given spatial location. The resulting slope of this line is indicative of the local velocity. A user-specified tolerance, that is, a minimum allowable coefficient of determination (R^2), dictates how strictly this linear regression line must fit the data. To validate the DEVOLS processing scheme, a temporally resolved sequence containing 16 synthetically generated particle images was considered in which the flow field was specified to be a Hamel-Oseen vortex. Effects due to varying particle density as well as varying noise conditions were specifically addressed. Following such validation, results achieved for the over-expanded jet considered during the experimental investigation were shown. However, due to the poor quality of these results, only qualitative descriptions were possible. Thus to better characterize the effectiveness of the DEVOLS algorithm as applied to a supersonic, shock-containing jet, synthetic particle-image sequences were generated using the velocity-field results of a previously conducted, large eddy simulation analysis. Based on these sequences, realistic measurements

were able to be achieved at different spatial locations in the jet, namely the region immediately following the nozzle exit as well as the region encompassing the potential core collapse. Experimental investigations of these regions are anticipated in the near future following notable improvements to the PIV system.

One such improvement that has already been made is the implementation of a new seeding mechanism. As discussed in chapter 5, very low particle densities were observed in the experimental images due to problems associated with the inconsistent seeding procedure. Loose, dry particles confined to a nitrogen-pressurized reservoir were injected into the burner system via four seeding tubes connected symmetrically around the combustion chamber. Particle clumping and subsequent blockages in one or more of these seeding tubes severely limited the maximum-achievable particle density during the experiments. To illustrate this point, one of the better particle images recorded with this seeding mechanism is shown in figure 7.1(a). It should be mentioned that neither this image nor the one in figure 7.1(b) were acquired with the Cordin camera.

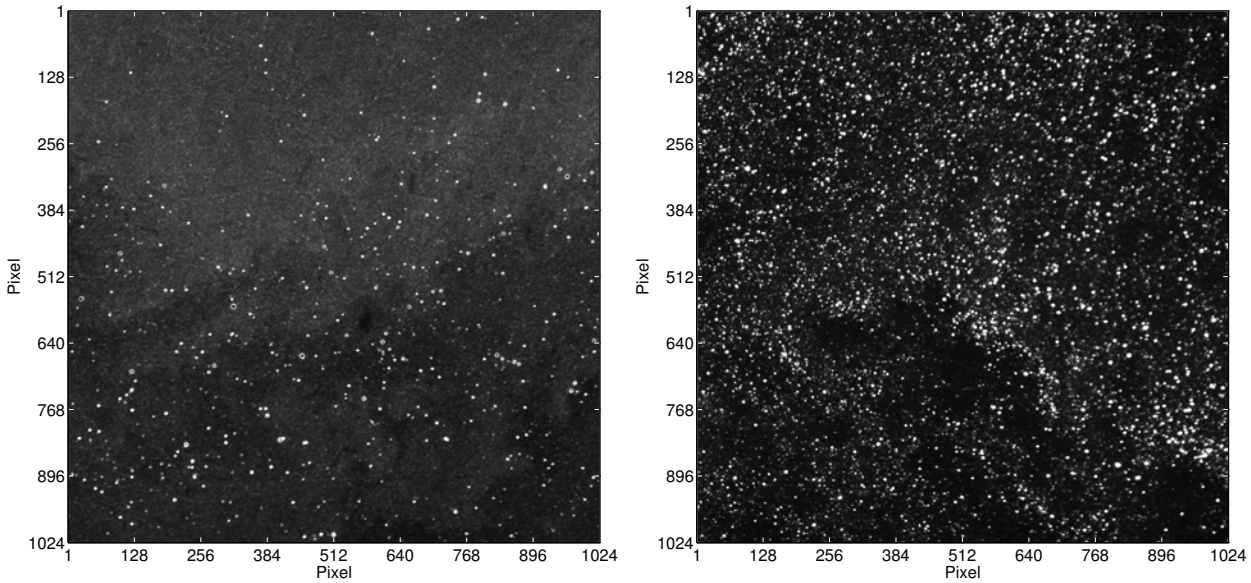

(a) Particle image with the old seeding mechanism (b) Particle image with the new seeding mechanism

Figure 7.1: Particle images acquired in the experimental jet. Each aluminum oxide particle is nominally 0.3 μm in diameter. The noticeable difference in particle density between the two cases reflects the considerable improvement achieved with the new seeding mechanism.

To overcome this problem, a new seeding system was installed that utilizes a mixture of ethanol and the aluminum oxide particles. By dissolving the particles in ethanol and subsequently injecting the solution into the combustion chamber, a very consistent seed density can be achieved. Furthermore, by avoiding blockages in the particle seeding tubes, a higher concentration of particles can be delivered to the flow. It should be mentioned that the ethanol is vaporized upstream of the nozzle exit due to the high temperatures associated with the propane combustion. Thus while imaging problems related to the ethanol solution are not a concern (i.e., the ethanol droplets are vaporized well upstream of the imaging region), extreme care must still be taken to ensure that the injected solution does not alter the physics or the desired properties (temperature, etc.) of the underlying flow. A sample particle image recorded with the new seeding mechanism is shown in figure 7.1(b).

A second and highly encouraged improvement that should be made regarding the PIV system is the correction to the individual camera focuses. Again as discussed in chapter 5, slight variations in focus between the eight optical pathways of the camera resulted from vibrations in the camera's internal optics, namely the beam splitters. Such vibrations were visible in the form of in-focus and out-of-focus particle images comprising each of the acquired image sequences. These variations impaired the HDR measurements because the results of individual correlations between in-focus and out-of-focus particle images were so poor. Thus it goes without saying that shielding the camera from intense sound levels to prevent problems associated with acoustically induced vibrations should be a major priority before similar PIV experiments are conducted.

In addition to revamping the experimental investigation, a couple of improvements are suggested for the DEVOLS algorithm that should enable better results. The first involves transitioning the iterative validation scheme from an OLS regression model to a weighted least squares approach. This modification would allow increased emphasis to be placed on measurements corresponding to optimum particle displacements. Stated differently, instead of treating all valid displacement measurements equally, an additional criterion should be

used to determine the optimum sampling rate (i.e., the optimum temporal separation between images) for a given spatial location. Increased weights could then be assigned to displacement measurements achieved at sampling rates nearest this optimum value. In addition to this modification, the derivation of a least squares equation that includes acceleration could also prove beneficial. Such an equation would enable regression lines to account for higher-order trends in the data and not be restricted to only linear fits. This approach would also allow an increased number of displacement results to be considered at each location which, in turn, could improve the overall measurement accuracy.

In closing, the HDR processing scheme presented in this thesis is clearly capable of increasing the dynamic velocity range of TR PIV measurements and concurrently reducing their overall measurement errors. Although the results achieved for the experimental investigation were subpar, the success experienced by the DEVOLS algorithm in accurately characterizing the Hamel-Oseen vortex as well as the synthetic jet data is more than sufficient to demonstrate this fact. Furthermore, the ability of the algorithm to function correctly in the presence of significant image noise speaks to the robustness of the processing scheme. Thus the hope is that the work contained herein will provide a solid foundation for achieving high-quality, HDR results in future experimental investigations.

Bibliography

[1] L. Prandtl. Über Flüssigkeitsbewegung bei sehr kleiner Reibung, Proc. *Verhandlungen des III. Internationalen Mathematiker-Kongresses, Heidelberg, 1904, Teubner, Leipzig*, pages 404–491, 1905.

[2] W. Merzkirch. *Flow Visualization*. Academic Press, London, 2nd edition, 1987.

[3] A. N. Kolmogorov. Dissipation of energy in the locally isotropic turbulence. *Proceedings of the USSR Academy of Sciences*, 32:16–18, 1941.

[4] R. J. Adrian and J. Westerweel. *Particle Image Velocimetry*. Cambridge University Press, New York, 2011.

[5] M. Raffel, C. E. Willert, S. T. Wereley, and J. Kompenhans. *Particle Image Velocimetry: A Practical Guide*. Springer, New York, 2nd edition, 2007.

[6] A. Melling. Tracer particles and seeding for particle image velocimetry. *Measurement Science and Technology*, 8(12):1406–1416, 1997.

[7] R. J. Adrian and C. S. Yao. Development of pulsed laser velocimetry (PLV) for measurement of fluid flow. *Proceedings of the 8th Biennial Symposium on Turbulence*, pp. 170–186. Rolla, Missouri, September 26-28, 1984.

[8] R. D. Keane and R. J. Adrian. Optimization of particle image velocimeters. Part I: Double pulsed systems. *Measurement Science and Technology*, 1(11):1202–1215, 1990.

[9] R. D. Keane and R. J. Adrian. Optimization of particle image velocimeters. Part II: Multiple pulsed systems. *Measurement Science and Technology*, 2(10):963–974, 1991.

[10] R. D. Keane and R. J. Adrian. Theory of cross-correlation analysis of PIV images. *Applied Scientific Research*, 49(3):191–215, 1992.

[11] G. Cavazzini (editor). *The Particle Image Velocimetry - Characteristics, Limits and Possible Applications*. InTech, 2012.

[12] P. A. Davidson. *Turbulence: An Introduction for Scientists and Engineers*. Oxford University Press, New York, 2004.

[13] K. T. Christensen and R. J. Adrian. Measurement of instantaneous Eulerian acceleration fields by particle image accelerometry: method and accuracy. *Experiments in Fluids*, 33(6):759–769, 2002.

[14] L. Perret, P. Braud, C. Fourment, L. David, and J. Delville. 3-Component acceleration field measurement by dual-time stereoscopic particle image velocimetry. *Experiments in Fluids*, 40(5):813–824, 2006.

[15] A. Jensen and G. K. Pedersen. Optimization of acceleration measurements using PIV. *Measurement Science and Technology*, 15(11):2275–2283, 2004.

[16] X. Liu and J. Katz. Instantaneous pressure and material derivative measurements using a four exposure PIV system. *Experiments in Fluids*, 41(2):227–240, 2006.

[17] D. Violato, P. Moore, and F. Scarano. Lagrangian and Eulerian pressure field evaluation of rod-airfoil flow from tomographic PIV. *Experiments in Fluids*, 50(4):1057–1070, 2011.

[18] R. J. Adrian. Dynamic ranges of velocity and spatial resolution of particle image velocimetry. *Measurement Science and Technology*, 8(12):1393–1398, 1997.

[19] R. J. Adrian. Twenty years of particle image velocimetry. *Experiments in Fluids*, 39(2):159–169, 2005.

[20] A. Fincham and G. Delerce. Advanced optimization of correlation imaging velocimetry algorithms. *Experiments in Fluids*, 29(Supplement 1):S13–S22, 2000.

[21] F. Pereira, A. Ciarravano, G. P. Romano, and F. Di Felice. Adaptive multi-frame PIV. *12th International Symposium on Applications of Laser Techniques to Fluid Mechanics*. Lisbon, Portugal, July 12-15, 2004.

[22] R. Hain and C. J. Kähler. Fundamentals of multiframe particle image velocimetry (PIV). *Experiments in Fluids*, 42(4):575–587, 2007.

[23] C. J. Kähler. Significance of dynamic evaluation of time resolved PIV images for complex flow investigations. *International Workshop on Dynamic PIV*. Takeda Hall, University of Tokyo, March 23, 2004.

[24] A. Sciacchitano, F. Scarano, and B. Wieneke. Adaptive multi-step ensemble correlation (AMEC) for time-resolved particle image velocimetry (TR-PIV). *9th International Symposium on Particle Image Velocimetry*. Kobe, Japan, July 21-23, 2011.

[25] C. D. Meinhart, S. T. Wereley, and J. G. Santiago. A PIV algorithm for estimating time-averaged velocity fields. *Journal of Fluids Engineering*, 122(2):285–289, 2000.

[26] T. Persoons and T. S. O'Donovan. High dynamic velocity range particle image velocimetry using multiple pulse separation imaging. *Sensors*, 11(1):1–18, 2011.

[27] N. Murray, G. Lyons, C. E. Tinney, B. Donald, W. Baars, B. Thurow, H. Haynes, and P. Panickar. A laboratory framework for synchronous near/far-field acoustics and MHz PIV in high-temperature, shock-containing, jets. *Proceedings of the Internoise 2012/ASME NCAD meeting*, New York City, USA, August 19-22, 2012.

[28] N. E. Murray, C. E. Tinney, B. S. Thurow, and N. Sinha. Toward active control of noise from hot supersonic jets. *Technical Proposal*, BAA 11-001 Special Notice 11-SN-0007.

[29] M. J. Lighthill. On sound generated aerodynamically. I. General theory. *Proceedings of the Royal Society of London. Series A, Mathematical and Physical Sciences*, 211(1107):564–587, 1952.

[30] M. J. Lighthill. On sound generated aerodynamically. II. Turbulence as a source of sound. *Proceedings of the Royal Society of London. Series A, Mathematical and Physical Sciences*, 222(1148):1–32, 1954.

[31] I. Proudman. The generation of noise by isotropic turbulence. *Proceedings of the Royal Society of London. Series A, Mathematical and Physical Sciences*, 214(1116):119–132, 1952.

[32] H. S. Ribner. Quadrupole correlations governing the pattern of jet noise. *Journal of Fluid Mechanics*, 38(1):1–24, 1969.

[33] L. Ukeiley, C. Tinney, R. Mann, and M. Glauser. Spatial correlations in a transonic jet. *AIAA Journal*, 45(6):1357–1369, 2007.

[34] M. Ponton, J. Seiner, L. Ukeiley, and B. Jansen. A new anechoic chamber design for testing high-temperature jet flows. *AIAA Paper*, No. 2001-2190, 2001.

[35] W. R. Lempert, P. Wu, B. Zhang, R. B. Miles, J. L. Lowrance, V. Mastracola, and W. F. Kosonocky. Pulseburst laser system for high speed flow diagnostics. *AIAA Paper*, No. 96-0179, 1996.

[36] M. Wernet and A. Opalski. Development and application of a MHz frame rate digital particle image velocimetry system. *AIAA Paper*, No. 2004-2184, 2004.

[37] B. Thurow, A. Satija, and K. Lynch. Third-generation megahertz-rate pulse burst laser system. *Applied Optics*, 48(11):2086–2093, 2009.

[38] W. Thielicke and E. J. Stamhuis. PIVlab - time-resolved digital particle image velocimetry tool for MATLAB. Published under the BSD license, programmed with MATLAB 7.1.0.246 (R14) Service Pack 3, MATLAB Central: *PIVlab_GUI.m*, 2005.

[39] N. Sinha, C. Kannepalli, and S. Arunajatesan. LES Predictions of Noise Emissions from a Low-Bypass Ratio Military Gas Turbine Engine. *Proceedings of the ASME Turbo Expo 2010: Gas Turbine Technical Congress & Exposition*, No. GT2010-22191, Glasgow, UK, June 14-18, 2010.

[40] J. Erwin and N. Sinha. Near and Far-Field Investigations of Supersonic Jet Noise Predictions Using a Coupled LES and FW-H Equation Method. *Proceedings of the ASME Turbo Expo 2011: Turbine Technical Conference & Exposition*, No. GT2011-45210, Vancouver, Canada, June 6-10, 2011.

[41] J. H. Ferziger. *Simulation and Modeling of Turbulent Flows*, chapter 3 Large Eddy Simulation, p. 109. Oxford University Press, New York, 1996.

[42] J. R. Taylor. *An Introduction to Error Analysis: The Study of Uncertainties in Physical Measurements*, chapter 4.1 Random and Systematic Errors, p. 94. University Science Books, Sausalito, California, 1997.

[43] T. Peng. Detect circles with various radii in grayscale image via Hough transform. Department of Mechanical Engineering, University of Maryland, College Park, Maryland 20742, USA, MATLAB Central: *CircularHough_Grd.m*, 2005.

[44] P. J. Rousseeuw and C. Croux. Alternatives to the median absolute deviation. *Journal of the American Statistical Association*, 88(424):1273–1283, 1993.

Appendices

Appendix A

Experimental Settings

This appendix contains the operational parameters and timing settings for the major constituents of the MHz frame rate PIV system (i.e., the pulse burst laser and the Cordin high-speed camera). A primary timing box served as the master trigger or signal generator for all of the individual components. An additional timing box used as an intermediary device to the AOM provided the means of creating MHz rate laser pulses for particle illumination. Settings in the camera software allowed the framing rate of the camera to be synchronized with the pulse-generating rate of the pulse burst laser. A delay sent to the camera from the primary timing box enabled direct selection of the 16 laser pulses that were actually imaged. Ultimately this configuration allowed the pulse burst laser to be synchronized with the Cordin high-speed camera such that TR PIV could be performed. More information including the exact setting values for each component are given in the sections below.

Pulse burst laser The primary timing box (Quantum Composer 9530 Series Pulse Generator) was operated in continuous mode with a specified T_0 period of 0.5 s (2 Hz). This particular setting was chosen based on previous experiments conducted at Auburn University, Florida State University, and Texas A&M in which superior levels of laser stability were achieved by operating the amplifier flashlamps at this repetition rate. An intermediary timing box (Quantum Composer Model 9514 Pulse Generator) connected only to the AOM was specified to operate in burst mode. For each input trigger this mode allowed a sequence of 60 pulses to be generated with a specified $T_0 = 1.0$ μs (1 MHz). Based on this configuration the laser system fired twice each second, with each firing constituting a burst of 60 pulses with an interframe time of 1.0 μs. A delay sent to the camera from the primary timing box determined which 16 pulses were actually imaged. The exact settings for the primary

and intermediary timing boxes as well as the flashlamp-pumped Nd:YAG rod amplifiers are given in the tables below. Further discussion regarding the delay, exposure, and operational settings for the camera is provided in the following section.

Table A.1: Settings for the primary timing box as well as the amplifier control boxes. The primary timing box was operated in continuous mode with a T_0 period of 0.5 s.

Channel	Device	Delay (μs)	Duration (μs)	Voltage (V)
A	Amp 1	85	250	370
B	Amp 2	85	250	420
C	Amp 3	160	150	470
D	Amp 4	160	200	800
E	Amp 5	175	200	1000
F	Amp 6	175	200	900
G	Camera	665	—	—
H	AOM *	575	—	—

* An additional timing box served as an intermediary control to this device.

Table A.2: Settings for the intermediary timing box. This box was operated in burst mode with a specified number of 60 pulses and a $T_0 = 1.0$ μs.

Channel	Device	Delay (μs)	Width (ns)
A	AOM	0	20
B	Oscilloscope	0	20
C	—	—	—
D	—	—	—

Cordin 222-4G high-speed camera The Cordin software in conjunction with a high-accuracy clock internal to the camera permitted full control of the eight independent optical pathways. Individual delay and exposure settings were available for each channel along with the ability to modify the MCP and CCD gains. Because the camera was operated in double-shot mode, two images (denoted A and B in table A.3) were captured per optical channel. Similarly to the A sequence, delay and exposure settings were available for all frames recorded in the B sequence. The delay settings provided by the camera software enabled each channel to be temporally positioned relative to the other channels and thus

synchronized with the pulse-generating rate of the pulse burst laser. The 16 images acquired at a 1 MHz framing rate were achieved by delaying each channel 1.0 μs from the previous one. The exposure setting for all cases was specified to be 0.75 μs. This *frame-on* time was more than sufficient to encompass the corresponding 20 ns laser pulse utilized for particle illumination. As mentioned previously, a master delay sent to the camera from the primary timing box dictated which block of 16 laser pulses was selected for synchronization with the 16 camera frames. A photodiode connected to a MHz rate oscilloscope (Tektronix TDS5054B Digital Phosphor Oscilloscope) enabled real-time viewing of the 60 laser pulses generated by the pulse burst laser. Based on the pulse profile, the most stable 16 pulses were chosen for imaging. All setting values for the camera software are provided in table A.3 below.

Table A.3: Software settings for the internal timing system of the Cordin high-speed camera.

Channel	Sequence	Delay (μs)	Exposure (μs)	CCD Gain	MCP Gain (Offset)
1	A, B	0, 8	0.75, 0.75	90	100 (+25)
2	A, B	1, 9	0.75, 0.75	90	100 (−7)
3	A, B	2, 10	0.75, 0.75	90	100 (−12)
4	A, B	3, 11	0.75, 0.75	90	100 (+0)
5	A, B	4, 12	0.75, 0.75	90	100 (+16)
6	A, B	5, 13	0.75, 0.75	90	100 (+7)
7	A, B	6, 14	0.75, 0.75	90	100 (+7)
8	A, B	7, 15	0.75, 0.75	90	100 (−8)

For completion it should be noted that the near-field and the far-field pressure measurement devices were synchronized with the PIV system using auxiliary output triggers from the camera. Although the primary timing box was run continuously at 2 Hz, the camera actually controlled how frequently measurements were performed. This particular mode of operation was chosen since the data transfer between the camera and its controlling computer represented the limiting factor in regards to turn-around time between acquisition periods. By ensuring that the camera performed at its maximum turnover rate, the overall experimental procedure was optimized.

The experimental procedure was also automated by employing the Auto Rearm feature included in the camera software. Once armed, the camera would wait for an external trigger from the primary timing box before recording images. As described, this trigger served to delay or position the camera frames with respect to the desired block of laser pulses. Auxiliary connections available on the camera provided the means of relaying the external trigger to the pressure-sensing devices. The signal then activated the necessary components in each of these devices to ensure that all measurements were acquired over the same temporal window. The setting values specified in the camera software for the first auxiliary (AUX 1) output sequence are as follows: Delay = 2.0 μs and On Time = 16.0 μs. The second auxiliary output sequence remained unused.

Appendix B

DEVOLS Processing Code

```
% Dynamic Evaluation via Ordinary Least Squares (DEVOLS)
% R. Harris Haynes | rhh0006@auburn.edu

%%%%%%%%%%%%%%%%%%%%%%%%%%%%%%%%%%%%%%%%%%%%%%%%%%%%%%%%%%%%%%%%%%%%%%%%%%%%%%%

clear all;
close all;
clc;

%#ok<*NASGU>
%#ok<*SAGROW>

%%%%%%%%%%%%%%%%%%%%%%%%%%%%%%%%%%%%%%%%%%%%%%%%%%%%%%%%%%%%%%%%%%%%%%%%%%%%%%%

% Specify path to Dantec files (.mat)
fpath = '<FilePath>';
fname1 = '<FileNamePrefix>';
fname2 = '<FileNameSuffix>';

% Save output?  ('yes' or 'no')
fsave = 'no';

%%%%%%%%%%%%%%%%%%%%%%%%%%%%%%%%%%%%%%%%%%%%%%%%%%%%%%%%%%%%%%%%%%%%%%%%%%%%%%%

% Load Dantec files
filename = [fpath,fname1,'A1B8_',fname2,'.mat'];
load(filename,'x','y','u','v','status');
xx(:,:,1) = x; yy(:,:,1) = y; uu(:,:,1) = u; vv(:,:,1) = v;
ss(:,:,1) = status;
clear filename x y u v status;

filename = [fpath,fname1,'A2B7_',fname2,'.mat'];
load(filename,'x','y','u','v','status');
xx(:,:,2) = x; yy(:,:,2) = y; uu(:,:,2) = u; vv(:,:,2) = v;
ss(:,:,2) = status;
clear filename x y u v status;

filename = [fpath,fname1,'A3B6_',fname2,'.mat'];
load(filename,'x','y','u','v','status');
xx(:,:,3) = x; yy(:,:,3) = y; uu(:,:,3) = u; vv(:,:,3) = v;
ss(:,:,3) = status;
clear filename x y u v status;

```

```
filename = [fpath,fname1,'A4B5_',fname2,'.mat'];
load(filename,'x','y','u','v','status');
xx(:,:,4) = x; yy(:,:,4) = y; uu(:,:,4) = u; vv(:,:,4) = v;
ss(:,:,4) = status;
clear filename x y u v status;

filename = [fpath,fname1,'A5B4_',fname2,'.mat'];
load(filename,'x','y','u','v','status');
xx(:,:,5) = x; yy(:,:,5) = y; uu(:,:,5) = u; vv(:,:,5) = v;
ss(:,:,5) = status;
clear filename x y u v status;

filename = [fpath,fname1,'A6B3_',fname2,'.mat'];
load(filename,'x','y','u','v','status');
xx(:,:,6) = x; yy(:,:,6) = y; uu(:,:,6) = u; vv(:,:,6) = v;
ss(:,:,6) = status;
clear filename x y u v status;

filename = [fpath,fname1,'A7B2_',fname2,'.mat'];
load(filename,'x','y','u','v','status');
xx(:,:,7) = x; yy(:,:,7) = y; uu(:,:,7) = u; vv(:,:,7) = v;
ss(:,:,7) = status;
clear filename x y u v status;

filename = [fpath,fname1,'A8B1_',fname2,'.mat'];
load(filename,'x','y','u','v','status');
xx(:,:,8) = x; yy(:,:,8) = y; uu(:,:,8) = u; vv(:,:,8) = v;
ss(:,:,8) = status;
clear filename x y u v status;

%%%%%%%%%%%%%%%%%%%%%%%%%%%%%%%%%%%%%%%%%%%%%%%%%%%%%%%%%%%%%%%%%%%%%%%%%%%%%%%

% Cordin 222-4G CCD sensor (px)
npx = 2048;
npy = 2048;

% Dimensions in terms of interrogation regions (vec)
nrow = size(xx,1);
ncol = size(xx,2);

%%%%%%%%%%%%%%%%%%%%%%%%%%%%%%%%%%%%%%%%%%%%%%%%%%%%%%%%%%%%%%%%%%%%%%%%%%%%%%%

% Specify temporal separations for all image pairs
dt_all = (1:2:15)';

% Specify maximum allowable particle displacement
dx_max = 12;

% Specify R^2 tolerance for each interrogation region [0...1]
R2_tol = 0.975;

%%%%%%%%%%%%%%%%%%%%%%%%%%%%%%%%%%%%%%%%%%%%%%%%%%%%%%%%%%%%%%%%%%%%%%%%%%%%%%%

% Initialize HDR matrices
x_HDR = xx(:,:,8); clear xx;
y_HDR = yy(:,:,8); clear yy;
```

```
u_HDR = zeros(nrow,ncol);
v_HDR = zeros(nrow,ncol);
n_HDR = zeros(nrow,ncol);

% Perform HDR analysis (pass 1)
for i = 1:nrow
    for j = 1:ncol

        % Compile all displacement results for a given vector location
        utmp = uu(i,j,8:-1:1); u(:,1) = utmp; clear utmp;
        vtmp = vv(i,j,8:-1:1); v(:,1) = vtmp; clear vtmp;
        uv = sqrt(u.*u+v.*v);

        % Remove displacements greater than the maximum allowable
        uv(uv>dx_max) = NaN;
        findnan = (isnan(uv) | any(isnan(dt_all)));
        havenan = any(findnan);
        if havenan
            dt = dt_all;
            dt(findnan) = [];
            uv(findnan) = [];
            u(findnan) = [];
            v(findnan) = [];
            n = length(uv);
        else
            dt = dt_all;
            n = length(uv);
        end
        clear findnan havenan;

        % Remove displacements less than any previous displacement
        %   Consider only total displacement (uv)
        if n>1 && uv(1,1)≠max(uv)
            for k = 2:n
                if uv(k,1)<max(uv(1:(k-1),1))
                    uv(k,1) = NaN;
                end
            end
            findnan = isnan(uv);
            havenan = any(findnan);
            if havenan
                dt(findnan) = [];
                uv(findnan) = [];
                u(findnan) = [];
                v(findnan) = [];
                n = length(uv);
            end
            clear k findnan havenan;
        end
        %   Consider only horizontal displacement (u)
        if n>1 && abs(u(1,1))≠max(abs(u)) && abs(u(1,1))>1
            for k = 2:n
                if abs(u(k,1))<max(abs(u(1:(k-1),1)))
                    uv(k,1) = NaN;
                end
            end
```

```
156             findnan = isnan(uv);
157             havenan = any(findnan);
158             if havenan
159                 dt(findnan) = [];
160                 uv(findnan) = [];
161                 u(findnan) = [];
162                 v(findnan) = [];
163                 n = length(uv);
164             end
165             clear k findnan havenan;
166         end
167         %   Consider only vertical displacement (v)
168         if n>1 && abs(v(1,1))≠max(abs(v)) && abs(v(1,1))>1
169             for k = 2:n
170                 if abs(v(k,1))<max(abs(v(1:(k-1),1)))
171                     uv(k,1) = NaN;
172                 end
173             end
174             findnan = isnan(uv);
175             havenan = any(findnan);
176             if havenan
177                 dt(findnan) = [];
178                 uv(findnan) = [];
179                 u(findnan) = [];
180                 v(findnan) = [];
181                 n = length(uv);
182             end
183             clear k findnan havenan;
184         end
185 
186         % Remove displacements following any rejected (NaN) displacements
187         if n>1
188             for k = 2:n
189                 if (dt(k,1)-dt((k-1),1))≠2
190                     dt(k,1) = NaN;
191                     uv(k,1) = NaN;
192                 end
193             end
194             findnan = isnan(uv);
195             havenan = any(findnan);
196             if havenan
197                 dt(findnan) = [];
198                 uv(findnan) = [];
199                 u(findnan) = [];
200                 v(findnan) = [];
201                 n = length(uv);
202             end
203             clear k findnan havenan;
204         end
205 
206         % Compute the velocity based on ordinary least squares (OLS)
207         uv_ols = (dt'*uv)/(dt'*dt); %dt\uv;
208         u_ols = (dt'*u)/(dt'*dt);   %dt\u;
209         v_ols = (dt'*v)/(dt'*dt);   %dt\v;
210 
211         % Compute the coefficient of determination (R^2)
```

```
212         if n>1
213             % average
214             uv_bar = sum(uv)/n;
215             % total sum of squares
216             uv_SStot = sum((uv-uv_bar).^2);
217             % regression sum of squares
218             uv_SSreg = sum((uv_ols.*dt-uv_bar).^2);
219             % residual sum of squares
220             uv_SSerr = sum((uv-uv_ols.*dt).^2);
221             % coefficient of determination (R^2)
222             uv_R2 = 1-uv_SSerr/uv_SStot;
223         else
224             uv_R2 = 1;
225         end
226         clear uv_bar uv_SStot uv_SSreg uv_SSerr;
227 
228         % Filter displacements based on the specified R^2 tolerance
229         while uv_R2<R2_tol
230 
231             % Remove only one displacement per iteration
232             if n>2
233 
234                 % Remove the displacement permitting the highest R^2 value
235                 tmp_uv_R2 = zeros(n,1);
236                 for k = 1:n
237                     if k==1
238                         tmp_dt = dt(2:end,1);
239                         tmp_uv = uv(2:end,1);
240                     elseif k==n
241                         tmp_dt = dt(1:(end-1),1);
242                         tmp_uv = uv(1:(end-1),1);
243                     else
244                         tmp_dt = [dt(1:(k-1),1);dt((k+1):end,1)];
245                         tmp_uv = [uv(1:(k-1),1);uv((k+1):end,1)];
246                     end
247                     tmp_uv_ols = (tmp_dt'*tmp_uv)/(tmp_dt'*tmp_dt);
248                     tmp_uv_bar = sum(tmp_uv)/(n-1);
249                     tmp_uv_SStot = sum((tmp_uv-tmp_uv_bar).^2);
250                     tmp_uv_SSreg = sum((tmp_uv_ols.*tmp_dt-tmp_uv_bar).^2);
251                     tmp_uv_SSerr = sum((tmp_uv-tmp_uv_ols.*tmp_dt).^2);
252                     tmp_uv_R2(k,1) = 1-tmp_uv_SSerr/tmp_uv_SStot;
253                     clear tmp_dt tmp_uv tmp_uv_ols tmp_uv_bar;
254                     clear tmp_uv_SStot tmp_uv_SSreg tmp_uv_SSerr;
255                 end
256                 [tmp,idx] = max(tmp_uv_R2);
257                 uv(idx,1) = NaN;
258                 findnan = isnan(uv);
259                 dt(findnan) = [];
260                 uv(findnan) = [];
261                 u(findnan) = [];
262                 v(findnan) = [];
263                 n = length(uv);
264                 clear k tmp_uv_R2 tmp idx findnan;
265 
266             else
267 
```

```
268                 % Remove the displacement with the maximum residual
269                 uv_res = abs(uv-uv_ols.*dt);
270                 uv_res(uv_res==max(uv_res(2:end,1))) = NaN;
271                 findnan = isnan(uv_res);
272                 dt(findnan) = [];
273                 uv(findnan) = [];
274                 u(findnan) = [];
275                 v(findnan) = [];
276                 n = length(uv);
277                 clear uv_res findnan;
278
279             end
280
281             % Compute the new velocity based on OLS
282             uv_ols = (dt'*uv)/(dt'*dt); %dt\uv;
283             u_ols = (dt'*u)/(dt'*dt);   %dt\u;
284             v_ols = (dt'*v)/(dt'*dt);   %dt\v;
285
286             % Compute the new coefficient of determination (R^2)
287             if n>1
288                 % average
289                 uv_bar = sum(uv)/n;
290                 % total sum of squares
291                 uv_SStot = sum((uv-uv_bar).^2);
292                 % regression sum of squares
293                 uv_SSreg = sum((uv_ols.*dt-uv_bar).^2);
294                 % residual sum of squares
295                 uv_SSerr = sum((uv-uv_ols.*dt).^2);
296                 % coefficient of determination (R^2)
297                 uv_R2 = 1-uv_SSerr/uv_SStot;
298             else
299                 uv_R2 = 1;
300             end
301             clear uv_bar uv_SStot uv_SSreg uv_SSerr;
302
303         end
304
305         % Adjust velocity components based on the highest R^2 component
306         if n>1
307             % average
308             u_bar = sum(u)/n;
309             v_bar = sum(v)/n;
310             % total sum of squares
311             u_SStot = sum((u-u_bar).^2);
312             v_SStot = sum((v-v_bar).^2);
313             % regression sum of squares
314             u_SSreg = sum((u_ols.*dt-u_bar).^2);
315             v_SSreg = sum((v_ols.*dt-v_bar).^2);
316             % residual sum of squares
317             u_SSerr = sum((u-u_ols.*dt).^2);
318             v_SSerr = sum((v-v_ols.*dt).^2);
319             % coefficient of determination (R^2)
320             u_R2 = 1-u_SSerr/u_SStot;
321             v_R2 = 1-v_SSerr/v_SStot;
322             % Compute only one new component
323             if u_R2>v_R2
```

```
                v_ols = (v_ols/abs(v_ols))*sqrt(uv_ols^2-u_ols^2);
            else
                u_ols = (u_ols/abs(u_ols))*sqrt(uv_ols^2-v_ols^2);
            end
        end
        clear u_bar u_SStot u_SSreg u_SSerr;
        clear v_bar v_SStot v_SSreg v_SSerr;

        % Retain the final results
        u_HDR(i,j) = u_ols;
        v_HDR(i,j) = v_ols;
        n_HDR(i,j) = n;

        % Clear any remaining variables
        clear dt uv uv_ols uv_R2 u u_ols u_R2 v v_ols v_R2 n;

    end
end
clear i j;

%%%%%%%%%%%%%%%%%%%%%%%%%%%%%%%%%%%%%%%%%%%%%%%%%%%%%%%%%%%%%%%%%%%%%%%%%%%%%%%

% Increase the maximum allowable particle displacement
dx_max = 28;

% Perform HDR analysis (pass 2)
for i = 1:nrow
    for j = 1:ncol

        % Compute the velocity obtained from pass 1
        uv_old = sqrt(u_HDR(i,j)*u_HDR(i,j)+v_HDR(i,j)*v_HDR(i,j));

        % Compute the sample deviation in the local velocity
        %   A square box of dimension 'box' defines the local region
        %   Specify an odd number greater than or equal to 3
        box = 5;
        if i>floor(box/2) && i<(nrow-floor(box/2-1)) &&...
                j>floor(box/2) && j<(ncol-floor(box/2-1))
            uv_box = sqrt(...
                u_HDR((i-floor(box/2)):(i+floor(box/2)),...
                (j-floor(box/2)):(j+floor(box/2))).*...
                u_HDR((i-floor(box/2)):(i+floor(box/2)),...
                (j-floor(box/2)):(j+floor(box/2)))+...
                v_HDR((i-floor(box/2)):(i+floor(box/2)),...
                (j-floor(box/2)):(j+floor(box/2))).*...
                v_HDR((i-floor(box/2)):(i+floor(box/2)),...
                (j-floor(box/2)):(j+floor(box/2))));
            uv_dif = (uv_box-uv_old).^2;
            uv_dev = sqrt(sum(sum(uv_dif))/(box*box-1));
        else
            uv_dev = 0;
        end

        % Consider only regions with weak velocity gradients
        if uv_dev<1

```

```
380             % Compile all displacement results for a given vector location
381             utmp = uu(i,j,8:-1:1); u(:,1) = utmp; clear utmp;
382             vtmp = vv(i,j,8:-1:1); v(:,1) = vtmp; clear vtmp;
383             uv = sqrt(u.*u+v.*v);
384
385             % Remove displacements greater than the maximum allowable
386             uv(uv>dx_max) = NaN;
387             findnan = (isnan(uv) | any(isnan(dt_all)));
388             havenan = any(findnan);
389             if havenan
390                 dt = dt_all;
391                 dt(findnan) = [];
392                 uv(findnan) = [];
393                 u(findnan) = [];
394                 v(findnan) = [];
395                 n = length(uv);
396             else
397                 dt = dt_all;
398                 n = length(uv);
399             end
400             clear findnan havenan;
401
402             % Remove displacements less than any previous displacement
403             %   Consider only total displacement (uv)
404             if n>1 && uv(1,1)≠max(uv)
405                 for k = 2:n
406                     if uv(k,1)<max(uv(1:(k-1),1))
407                         uv(k,1) = NaN;
408                     end
409                 end
410                 findnan = isnan(uv);
411                 havenan = any(findnan);
412                 if havenan
413                     dt(findnan) = [];
414                     uv(findnan) = [];
415                     u(findnan) = [];
416                     v(findnan) = [];
417                     n = length(uv);
418                 end
419                 clear k findnan havenan;
420             end
421             %   Consider only horizontal displacement (u)
422             if n>1 && abs(u(1,1))≠max(abs(u)) && abs(u(1,1))>1
423                 for k = 2:n
424                     if abs(u(k,1))<max(abs(u(1:(k-1),1)))
425                         uv(k,1) = NaN;
426                     end
427                 end
428                 findnan = isnan(uv);
429                 havenan = any(findnan);
430                 if havenan
431                     dt(findnan) = [];
432                     uv(findnan) = [];
433                     u(findnan) = [];
434                     v(findnan) = [];
435                     n = length(uv);
```

```
436                 end
437                 clear k findnan havenan;
438             end
439             %   Consider only vertical displacement (v)
440             if n>1 && abs(v(1,1))≠max(abs(v)) && abs(v(1,1))>1
441                 for k = 2:n
442                     if abs(v(k,1))<max(abs(v(1:(k-1),1)))
443                         uv(k,1) = NaN;
444                     end
445                 end
446                 findnan = isnan(uv);
447                 havenan = any(findnan);
448                 if havenan
449                     dt(findnan) = [];
450                     uv(findnan) = [];
451                     u(findnan) = [];
452                     v(findnan) = [];
453                     n = length(uv);
454                 end
455                 clear k findnan havenan;
456             end
457
458             % Remove displacements following any rejected (NaN) displacements
459             if n>1
460                 for k = 2:n
461                     if (dt(k,1)-dt((k-1),1))≠2
462                         dt(k,1) = NaN;
463                         uv(k,1) = NaN;
464                     end
465                 end
466                 findnan = isnan(uv);
467                 havenan = any(findnan);
468                 if havenan
469                     dt(findnan) = [];
470                     uv(findnan) = [];
471                     u(findnan) = [];
472                     v(findnan) = [];
473                     n = length(uv);
474                 end
475                 clear k findnan havenan;
476             end
477
478             % Compute the velocity based on ordinary least squares (OLS)
479             uv_ols = (dt'*uv)/(dt'*dt); %dt\uv;
480             u_ols = (dt'*u)/(dt'*dt);   %dt\u;
481             v_ols = (dt'*v)/(dt'*dt);   %dt\v;
482
483             % Compute the coefficient of determination (R^2)
484             if n>1
485                 % average
486                 uv_bar = sum(uv)/n;
487                 % total sum of squares
488                 uv_SStot = sum((uv-uv_bar).^2);
489                 % regression sum of squares
490                 uv_SSreg = sum((uv_ols.*dt-uv_bar).^2);
491                 % residual sum of squares
```

```
            uv_SSerr = sum((uv-uv_ols.*dt).^2);
            % coefficient of determination (R^2)
            uv_R2 = 1-uv_SSerr/uv_SStot;
        else
            uv_R2 = 1;
        end
        clear uv_bar uv_SStot uv_SSreg uv_SSerr;

        % Filter displacements based on the specified R^2 tolerance
        while uv_R2<R2_tol

            % Remove only one displacement per iteration
            if n>2

                % Remove the displacement permitting the highest R^2 value
                tmp_uv_R2 = zeros(n,1);
                for k = 1:n
                    if k==1
                        tmp_dt = dt(2:end,1);
                        tmp_uv = uv(2:end,1);
                    elseif k==n
                        tmp_dt = dt(1:(end-1),1);
                        tmp_uv = uv(1:(end-1),1);
                    else
                        tmp_dt = [dt(1:(k-1),1);dt((k+1):end,1)];
                        tmp_uv = [uv(1:(k-1),1);uv((k+1):end,1)];
                    end
                    tmp_uv_ols = (tmp_dt'*tmp_uv)/(tmp_dt'*tmp_dt);
                    tmp_uv_bar = sum(tmp_uv)/(n-1);
                    tmp_uv_SStot = sum((tmp_uv-tmp_uv_bar).^2);
                    tmp_uv_SSreg = sum((tmp_uv_ols.*tmp_dt-tmp_uv_bar).^2);
                    tmp_uv_SSerr = sum((tmp_uv-tmp_uv_ols.*tmp_dt).^2);
                    tmp_uv_R2(k,1) = 1-tmp_uv_SSerr/tmp_uv_SStot;
                    clear tmp_dt tmp_uv tmp_uv_ols tmp_uv_bar;
                    clear tmp_uv_SStot tmp_uv_SSreg tmp_uv_SSerr;
                end
                [tmp,idx] = max(tmp_uv_R2);
                uv(idx,1) = NaN;
                findnan = isnan(uv);
                dt(findnan) = [];
                uv(findnan) = [];
                u(findnan) = [];
                v(findnan) = [];
                n = length(uv);
                clear k tmp_uv_R2 tmp idx findnan;

            else

                % Remove the displacement with the maximum residual
                uv_res = abs(uv-uv_ols.*dt);
                uv_res(uv_res==max(uv_res(2:end,1))) = NaN;
                findnan = isnan(uv_res);
                dt(findnan) = [];
                uv(findnan) = [];
                u(findnan) = [];
                v(findnan) = [];
```

```
548                     n = length(uv);
549                     clear uv_res findnan;
550 
551                 end
552 
553                 % Compute the new velocity based on OLS
554                 uv_ols = (dt'*uv)/(dt'*dt); %dt\uv;
555                 u_ols = (dt'*u)/(dt'*dt);   %dt\u;
556                 v_ols = (dt'*v)/(dt'*dt);   %dt\v;
557 
558                 % Compute the new coefficient of determination (R^2)
559                 if n>1
560                     % average
561                     uv_bar = sum(uv)/n;
562                     % total sum of squares
563                     uv_SStot = sum((uv-uv_bar).^2);
564                     % regression sum of squares
565                     uv_SSreg = sum((uv_ols.*dt-uv_bar).^2);
566                     % residual sum of squares
567                     uv_SSerr = sum((uv-uv_ols.*dt).^2);
568                     % coefficient of determination (R^2)
569                     uv_R2 = 1-uv_SSerr/uv_SStot;
570                 else
571                     uv_R2 = 1;
572                 end
573                 clear uv_bar uv_SStot uv_SSreg uv_SSerr;
574 
575             end
576 
577             % Adjust velocity components based on the highest R^2 component
578             if n>1
579                 % average
580                 u_bar = sum(u)/n;
581                 v_bar = sum(v)/n;
582                 % total sum of squares
583                 u_SStot = sum((u-u_bar).^2);
584                 v_SStot = sum((v-v_bar).^2);
585                 % regression sum of squares
586                 u_SSreg = sum((u_ols.*dt-u_bar).^2);
587                 v_SSreg = sum((v_ols.*dt-v_bar).^2);
588                 % residual sum of squares
589                 u_SSerr = sum((u-u_ols.*dt).^2);
590                 v_SSerr = sum((v-v_ols.*dt).^2);
591                 % coefficient of determination (R^2)
592                 u_R2 = 1-u_SSerr/u_SStot;
593                 v_R2 = 1-v_SSerr/v_SStot;
594                 % Compute only one new component
595                 if u_R2>v_R2
596                     v_ols = (v_ols/abs(v_ols))*sqrt(uv_ols^2-u_ols^2);
597                 else
598                     u_ols = (u_ols/abs(u_ols))*sqrt(uv_ols^2-v_ols^2);
599                 end
600             end
601             clear u_bar u_SStot u_SSreg u_SSerr;
602             clear v_bar v_SStot v_SSreg v_SSerr;
603 
```

```
604             % Retain the final results
605             if (abs(uv_ols-uv_old)/uv_old)<0.5
606                 u_HDR(i,j) = u_ols;
607                 v_HDR(i,j) = v_ols;
608                 n_HDR(i,j) = n;
609             end
610 
611             % Clear any remaining variables
612             clear box uv_old uv_box uv_dif uv_dev;
613             clear dt uv uv_ols uv_R2 u u_ols u_R2 v v_ols v_R2 n;
614 
615         end
616 
617     end
618 end
619 clear dx_max i j uu vv ss;
620 
621 %%%%%%%%%%%%%%%%%%%%%%%%%%%%%%%%%%%%%%%%%%%%%%%%%%%%%%%%%%%%%%%%%%%%%%%%%%%%%%%
622 
623 % Save results to .mat file
624 if strcmp(fsave,'Yes') || strcmp(fsave,'yes')
625     savename = ['Dantec_HDR_',fname2,'.mat'];
626     save([fpath,savename],'x_HDR','y_HDR','u_HDR','v_HDR','n_HDR');
627 end
628 clear fname1 fname2;
629 
630 %%%%%%%%%%%%%%%%%%%%%%%%%%%%%%%%%%%%%%%%%%%%%%%%%%%%%%%%%%%%%%%%%%%%%%%%%%%%%%%
631 
632 % Plot results
633 f1 = figure('Name','Velocity Field (Vector)','NumberTitle','off');
634 set(f1,'Color','white','Position',[280 108 1120 840]);
635 
636 % QUIVER:
637 scale = 0; qscale = 6;
638 q1 = quiver(x_HDR,y_HDR,u_HDR,v_HDR,scale,'b');
639 set(q1,'LineWidth',1);
640 hU = get(q1,'UData'); hV = get(q1,'VData');
641 set(q1,'UData',qscale*hU,'VData',qscale*hV);
642 
643 axis image;
644 set(gca,'XLim',[0.5 npx+0.5],'XTick',[1,256:256:2048]);
645 set(gca,'YLim',[0.5 npy+0.5],'YTick',[1,256:256:2048]);
646 
647 set(gca,'Visible','off'); ax1 = gca;
648 ax2 = axes('Color','none','Position',get(ax1,'Position'));
649 set(ax2,'TickDir','in','Box','on','FontSize',16); axis ij image;
650 set(ax2,'XLim',[0.5 npx+0.5],'XTick',[1,256:256:2048]);
651 set(ax2,'YLim',[0.5 npy+0.5],'YTick',[1,256:256:2048]);
652 xlabel('x (px)'); ylabel('y (px)');
653 
654 if strcmp(fsave,'Yes') || strcmp(fsave,'yes')
655     export_fig(f1,[fpath,'Dantec_HDR_vec'],'-pdf');
656 end
657 clear f1 scale qscale q1 hU hV ax1 ax2;
658 
659 %%%%%%%%%%%%%%%%%%%%%%%%%%%%%%%%%%%%%%%%%%%%%%%%%%%%%%%%%%%%%%%%%%%%%%%%%%%%%%%
```

```
660
661 % Plot results
662 f2 = figure('Name','Velocity Field (Contour)','NumberTitle','off');
663 set(f2,'Color','white','Position',[280 108 1120 840]);
664
665 % IMAGESC:
666 imagesc(u_HDR); axis xy image;
667 cmap = 'jet'; colormap(cmap);
668
669 % Pixel displacement:
670 cmin = -8; cmax = 8; caxis([cmin cmax]);
671 c1 = colorbar('YTick',cmin:2:cmax,'FontSize',16);
672 title(c1,'{\it\Deltax / \Δt}');
673
674 set(gca,'Visible','off'); ax3 = gca;
675 ax4 = axes('Color','none','Position',get(ax3,'Position'));
676 set(ax4,'TickDir','in','Box','on','FontSize',16); axis ij image;
677 set(ax4,'XLim',[0.5 npx+0.5],'XTick',[1,256:256:2048]);
678 set(ax4,'YLim',[0.5 npy+0.5],'YTick',[1,256:256:2048]);
679 xlabel('x (px)'); ylabel('y (px)');
680
681 if strcmp(fsave,'Yes') || strcmp(fsave,'yes')
682     export_fig(f2,[fpath,'Dantec_HDR_con'],'-pdf');
683 end
684 clear f2 cmap cmin cmax c1 ax3 ax4;
685
686 %%%%%%%%%%%%%%%%%%%%%%%%%%%%%%%%%%%%%%%%%%%%%%%%%%%%%%%%%%%%%%%%%%%%%%%%%%%%%%%
687
688 % Plot results
689 f3 = figure('Name','Vector Evaluation Field (Contour)','NumberTitle','off');
690 set(f3,'Color','white','Position',[280 108 1120 840]);
691
692 % IMAGESC:
693 imagesc(n_HDR); axis xy image;
694 cmap = 'jet'; colormap(cmap);
695
696 % Total number of vectors considered:
697 cmin = 1; cmax = 8; caxis([cmin cmax]);
698 c2 = colorbar('YTick',cmin:cmax,'FontSize',16);
699 title(c2,'N_{vec}');
700
701 set(gca,'Visible','off'); ax5 = gca;
702 ax6 = axes('Color','none','Position',get(ax5,'Position'));
703 set(ax6,'TickDir','in','Box','on','FontSize',16); axis ij image;
704 set(ax6,'XLim',[0.5 ncol+0.5],'XTick',[1,16:16:112,127]);
705 set(ax6,'YLim',[0.5 nrow+0.5],'YTick',[1,16:16:112,127]);
706 xlabel('x (IA)'); ylabel('y (IA)');
707
708 if strcmp(fsave,'Yes') || strcmp(fsave,'yes')
709     export_fig(f3,[fpath,'Dantec_HDR_img'],'-pdf');
710 end
711 clear f3 cmap cmin cmax c2 ax5 ax6;
712 clear fpath fsave;
713
714 %%%%%%%%%%%%%%%%%%%%%%%%%%%%%%%%%%%%%%%%%%%%%%%%%%%%%%%%%%%%%%%%%%%%%%%%%%%%%%%
```

Appendix C

Hamel-Oseen Vortex Plots

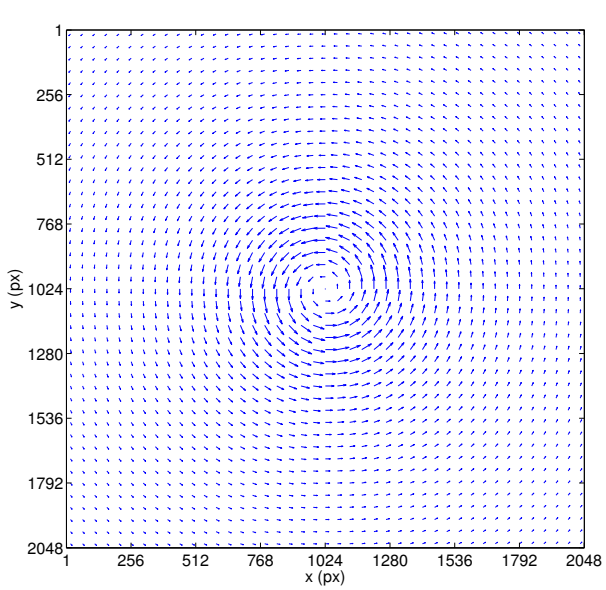

(a) Vector plot for the analytical solution

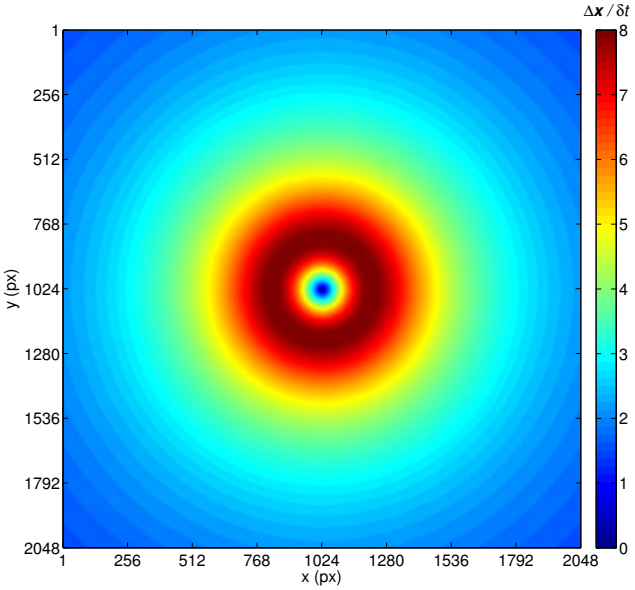

(b) Velocity magnitude for the analytical solution

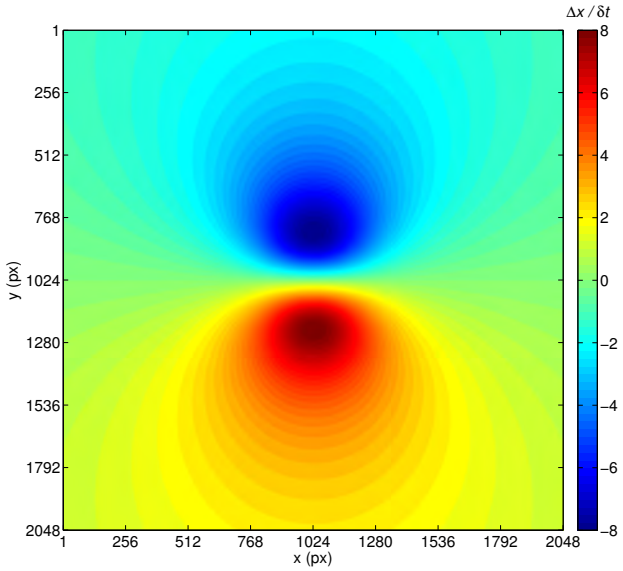

(c) Velocity ($\Delta x/\delta t$) for the analytical solution

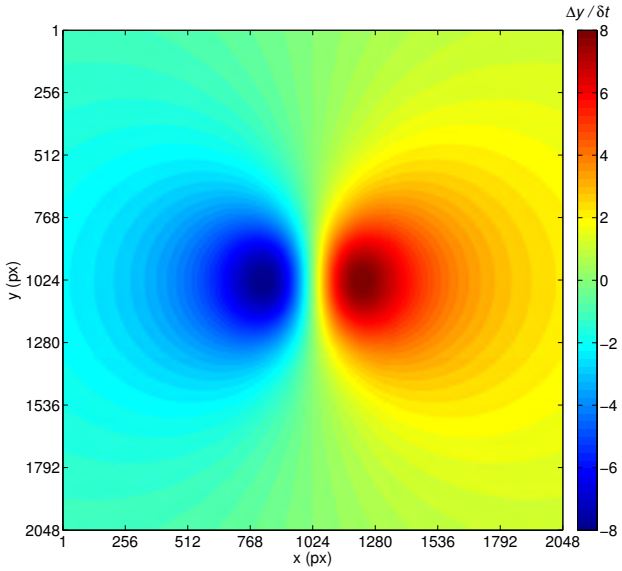

(d) Velocity ($\Delta y/\delta t$) for the analytical solution

Figure C.1: Analytical results for the synthetically generated Hamel-Oseen vortex.

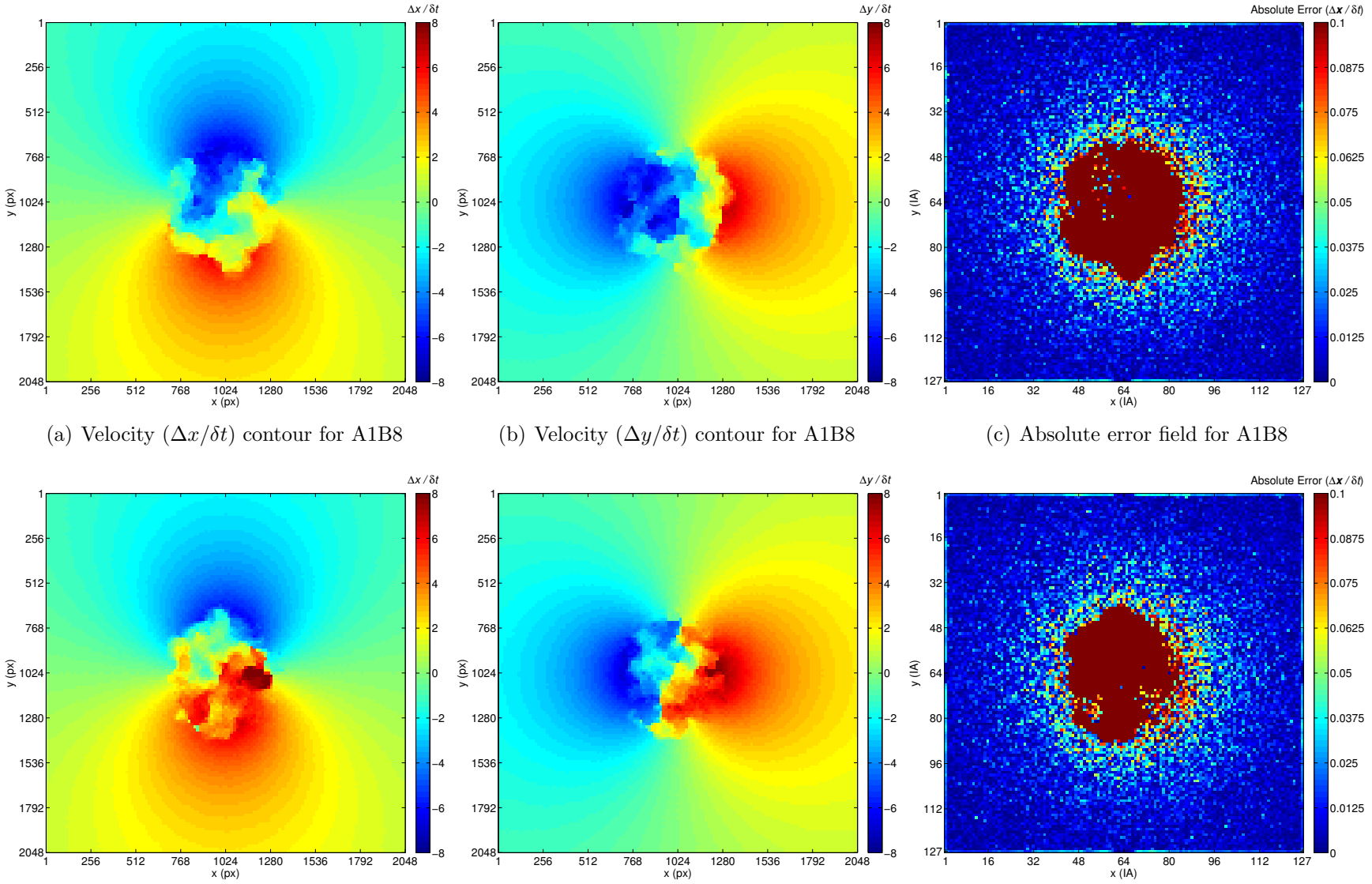

(a) Velocity ($\Delta x/\delta t$) contour for A1B8

(b) Velocity ($\Delta y/\delta t$) contour for A1B8

(c) Absolute error field for A1B8

(d) Velocity ($\Delta x/\delta t$) contour for A2B7

(e) Velocity ($\Delta y/\delta t$) contour for A2B7

(f) Absolute error field for A2B7

Figure C.2: Velocity field and absolute error results for the image pairs spanning $15\,\delta t$ (top) and $13\,\delta t$ (bottom).

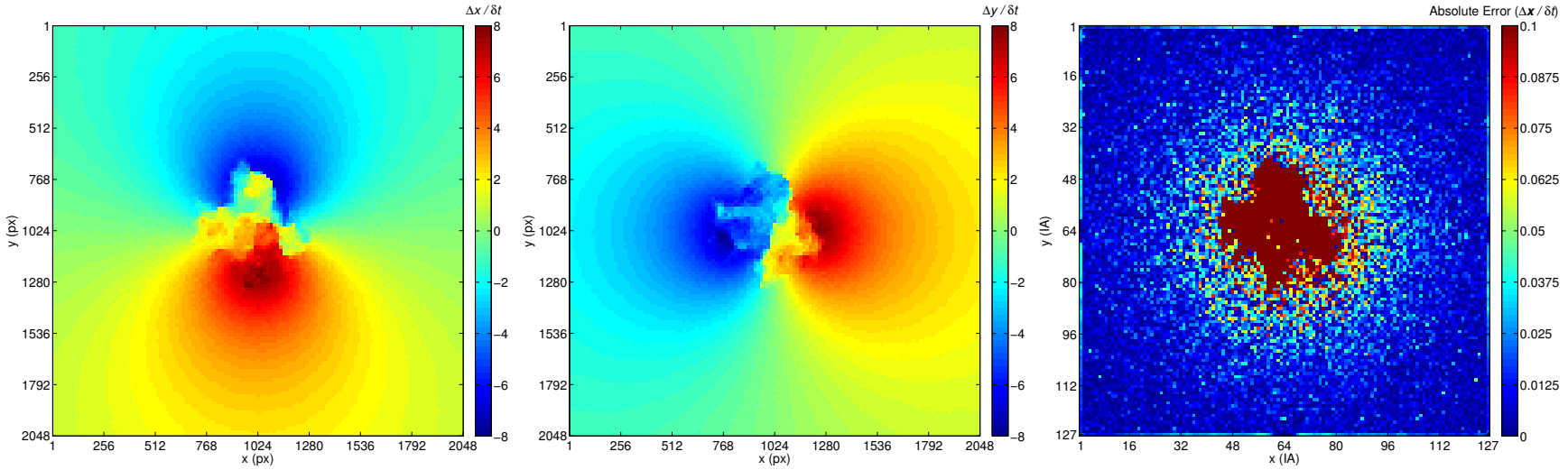

(a) Velocity ($\Delta x/\delta t$) contour for A3B6 (b) Velocity ($\Delta y/\delta t$) contour for A3B6 (c) Absolute error field for A3B6

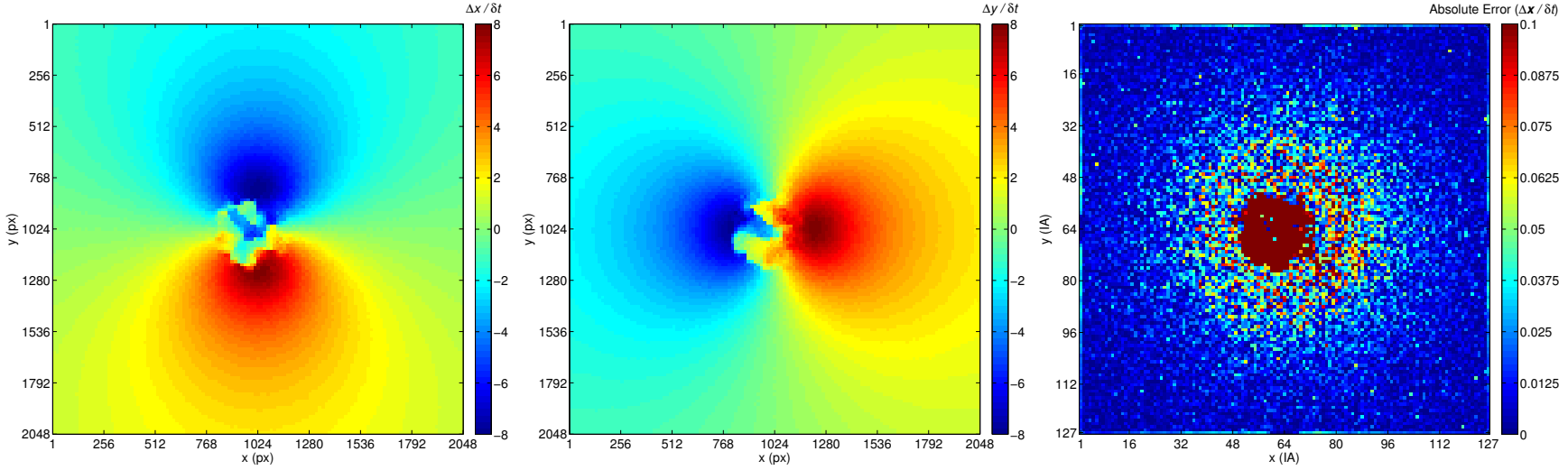

(d) Velocity ($\Delta x/\delta t$) contour for A4B5 (e) Velocity ($\Delta y/\delta t$) contour for A4B5 (f) Absolute error field for A4B5

Figure C.3: Velocity field and absolute error results for the image pairs spanning 11 δt (top) and 9 δt (bottom).

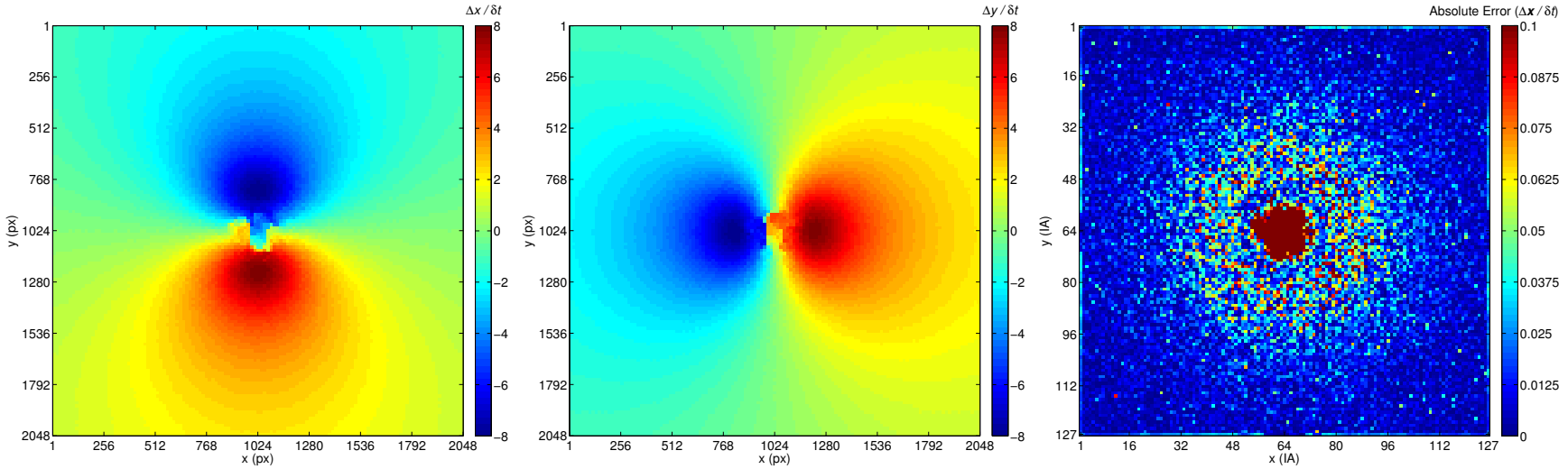

(a) Velocity ($\Delta x/\delta t$) contour for A5B4 (b) Velocity ($\Delta y/\delta t$) contour for A5B4 (c) Absolute error field for A5B4

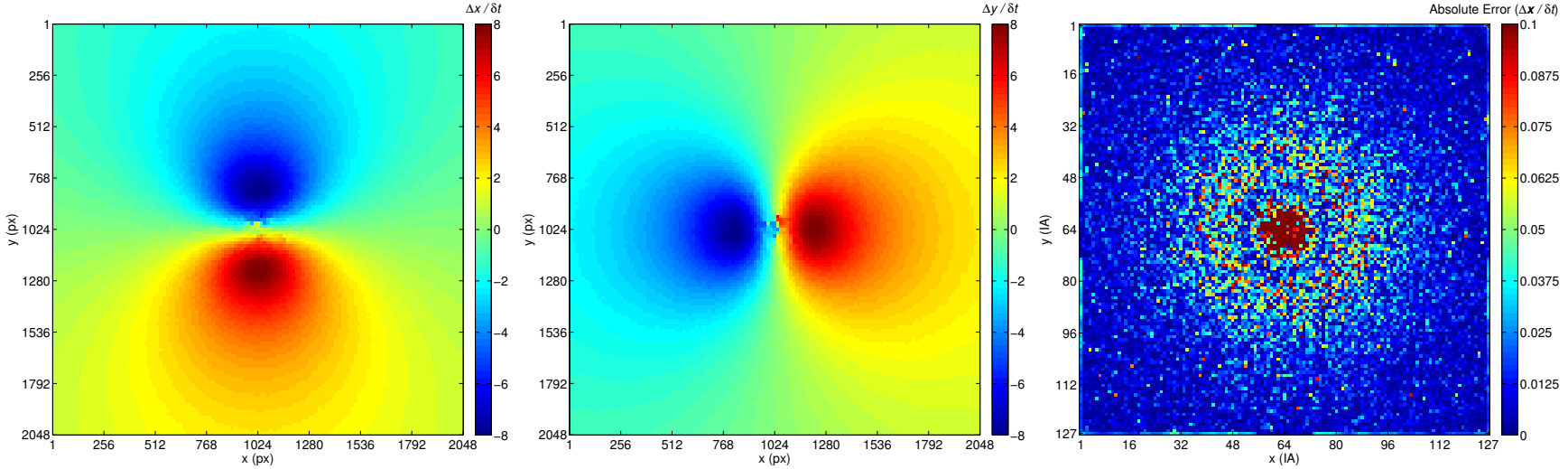

(d) Velocity ($\Delta x/\delta t$) contour for A6B3 (e) Velocity ($\Delta y/\delta t$) contour for A6B3 (f) Absolute error field for A6B3

Figure C.4: Velocity field and absolute error results for the image pairs spanning $7\,\delta t$ (top) and $5\,\delta t$ (bottom).

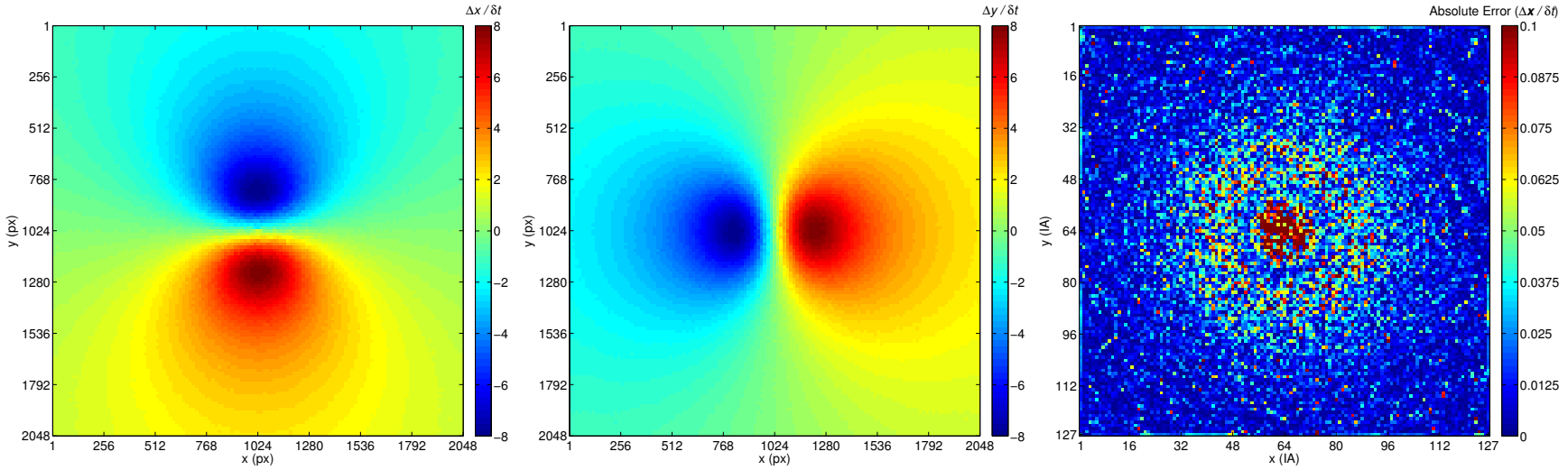

(a) Velocity ($\Delta x/\delta t$) contour for A7B2 (b) Velocity ($\Delta y/\delta t$) contour for A7B2 (c) Absolute error field for A7B2

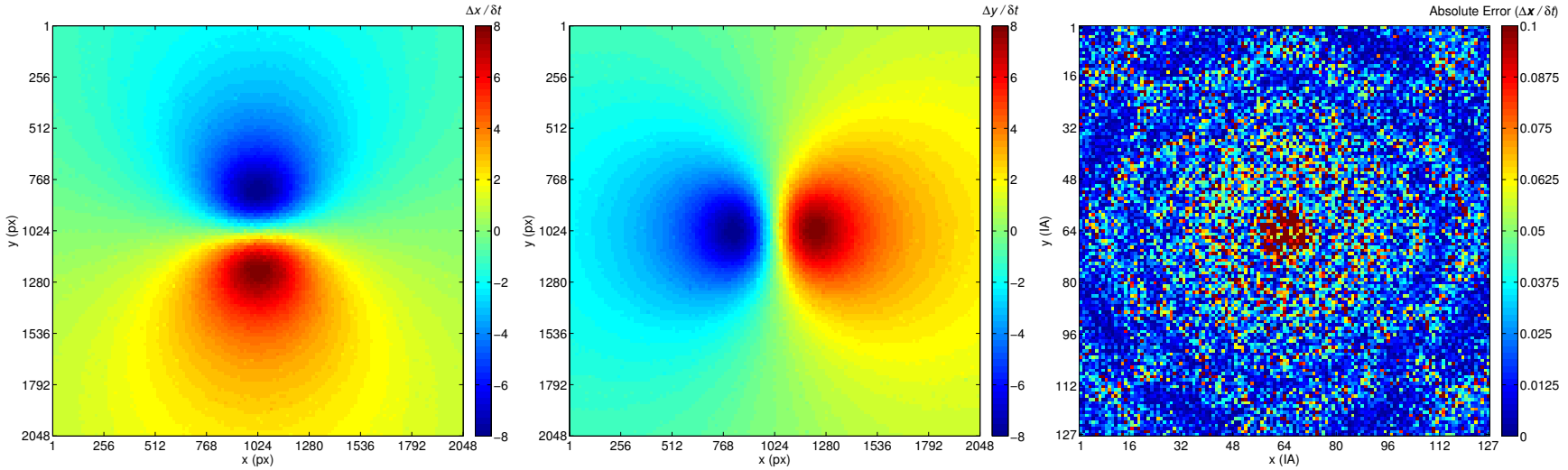

(d) Velocity ($\Delta x/\delta t$) contour for A8B1 (e) Velocity ($\Delta y/\delta t$) contour for A8B1 (f) Absolute error field for A8B1

Figure C.5: Velocity field and absolute error results for the image pairs spanning $3\,\delta t$ (top) and δt (bottom).

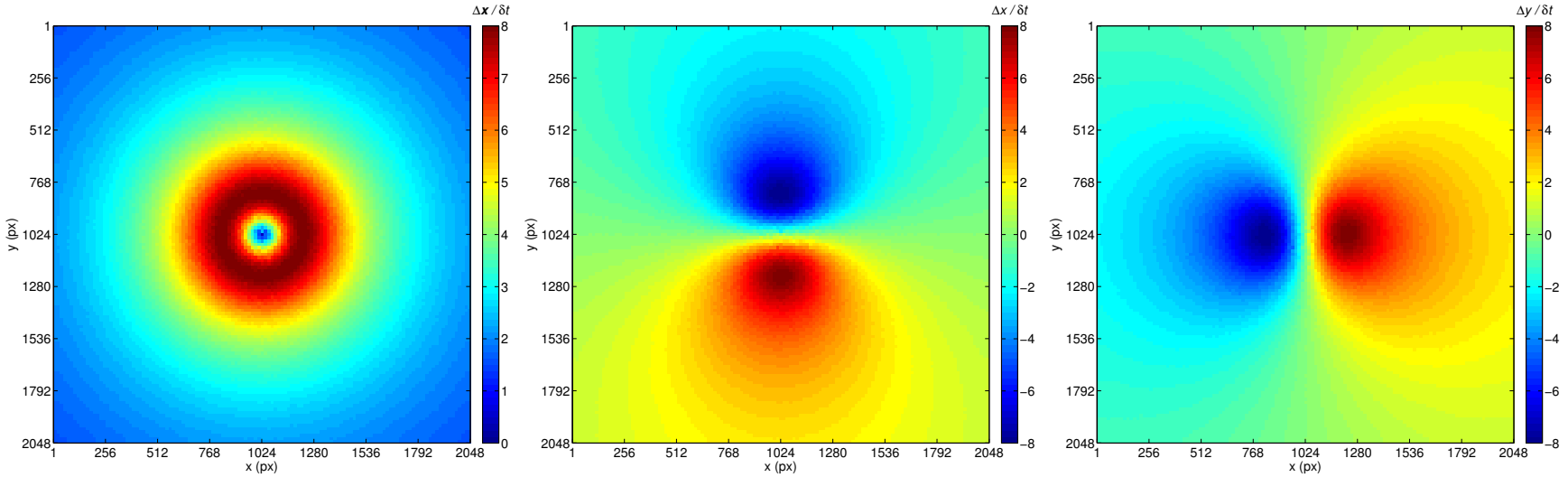

(a) Velocity magnitude for the HDR result (b) Velocity ($\Delta x/\delta t$) for the HDR result (c) Velocity ($\Delta y/\delta t$) for the HDR result

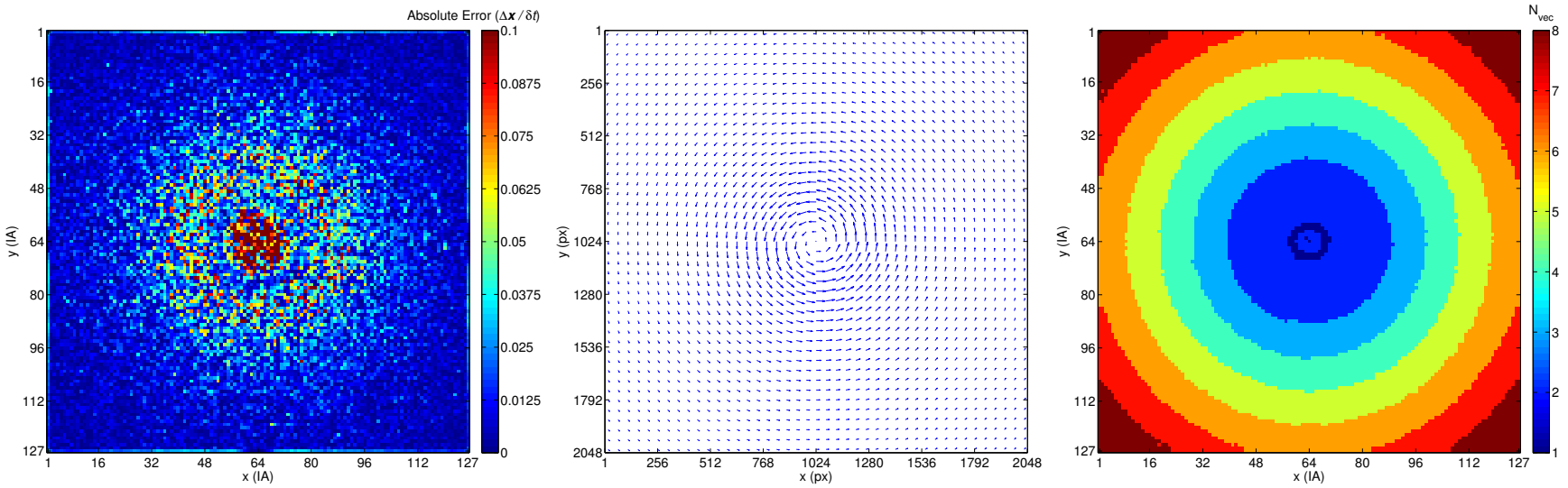

(d) Absolute error field for the HDR result (e) Vector plot for the HDR result (f) Vectors considered per spatial location

Figure C.6: HDR results for the synthetically generated Hamel-Oseen vortex.

Appendix D

Hamel-Oseen Vortex Pair Plots

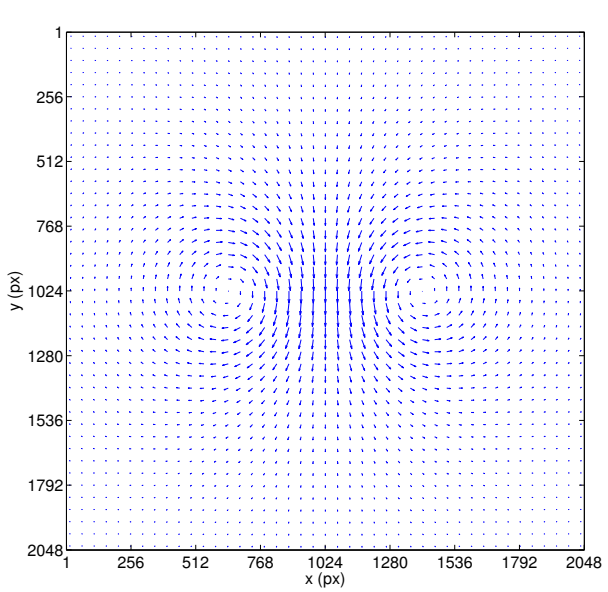

(a) Vector plot for the analytical solution

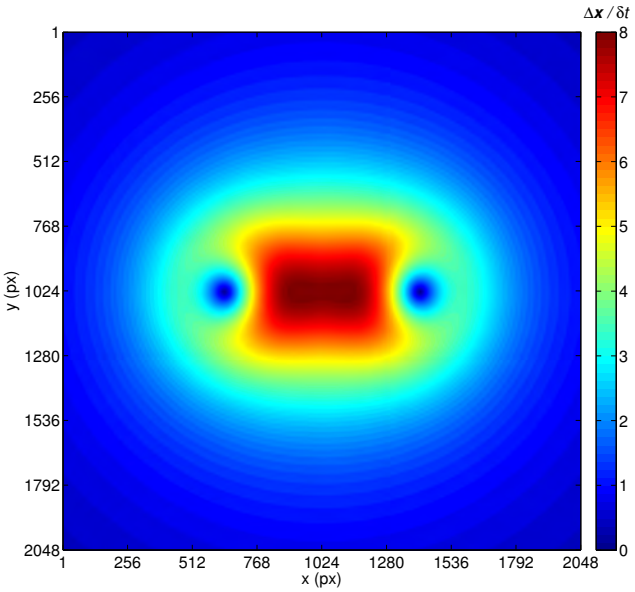

(b) Velocity magnitude for the analytical solution

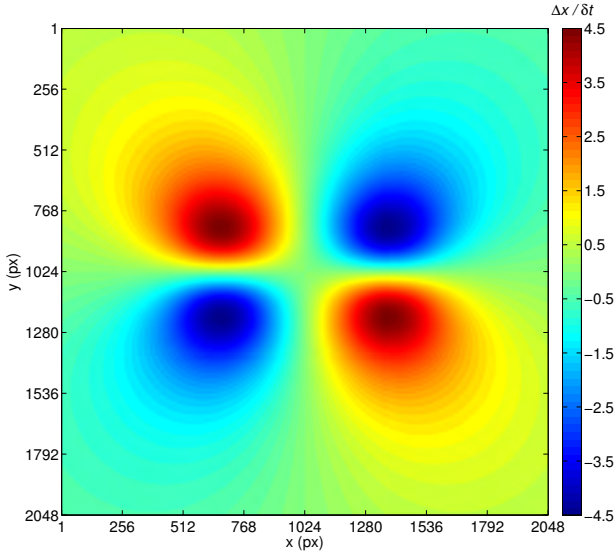

(c) Velocity ($\Delta x/\delta t$) for the analytical solution

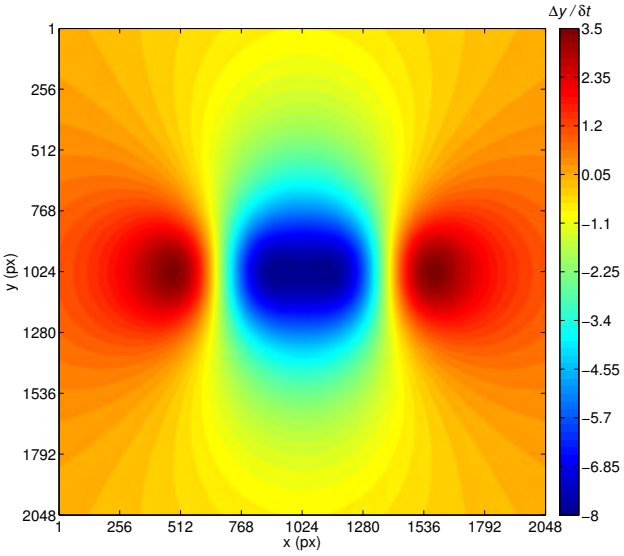

(d) Velocity ($\Delta y/\delta t$) for the analytical solution

Figure D.1: Analytical results for the synthetically generated Hamel-Oseen vortex pair.

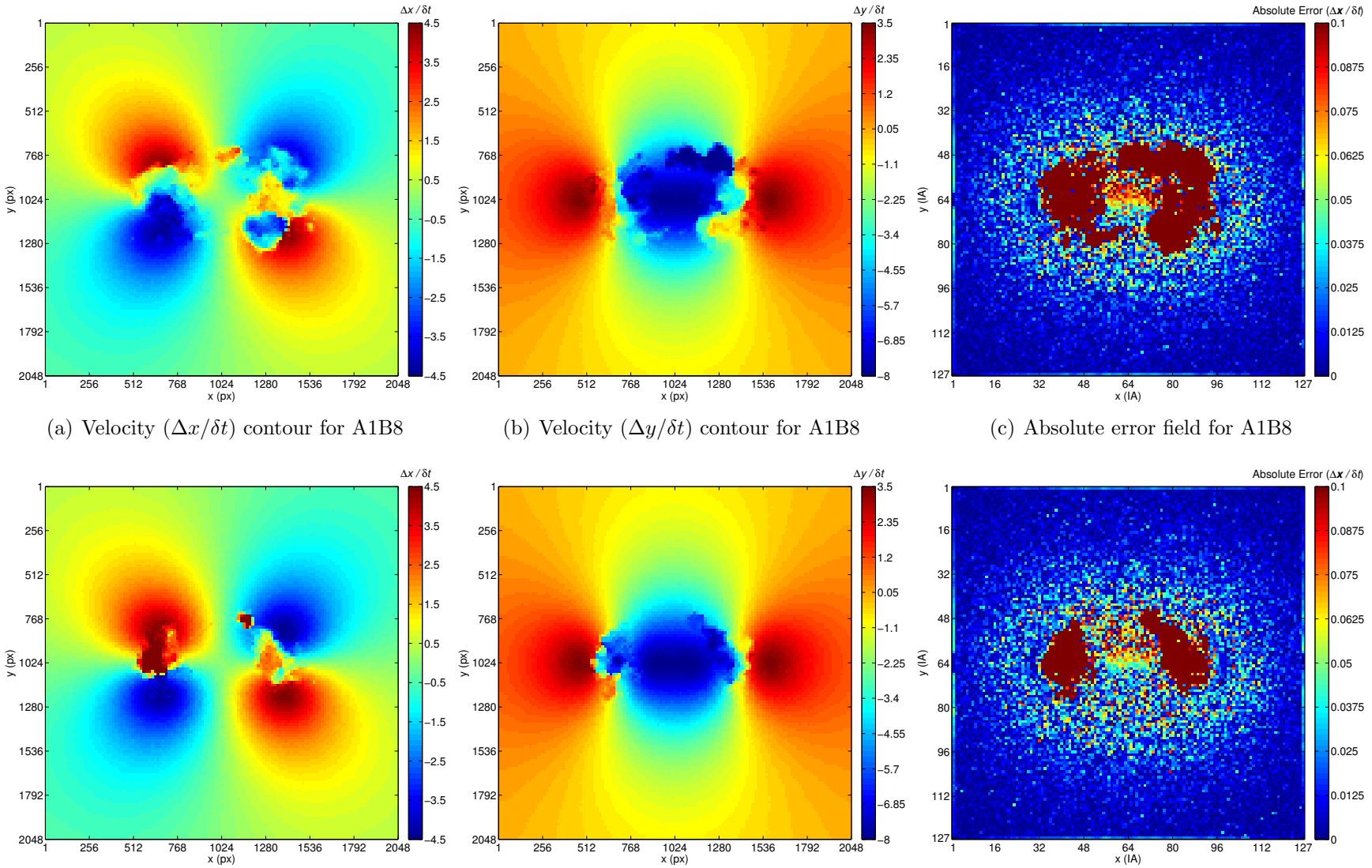

(a) Velocity ($\Delta x/\delta t$) contour for A1B8

(b) Velocity ($\Delta y/\delta t$) contour for A1B8

(c) Absolute error field for A1B8

(d) Velocity ($\Delta x/\delta t$) contour for A2B7

(e) Velocity ($\Delta y/\delta t$) contour for A2B7

(f) Absolute error field for A2B7

Figure D.2: Velocity field and absolute error results for the image pairs spanning $15\,\delta t$ (top) and $13\,\delta t$ (bottom).

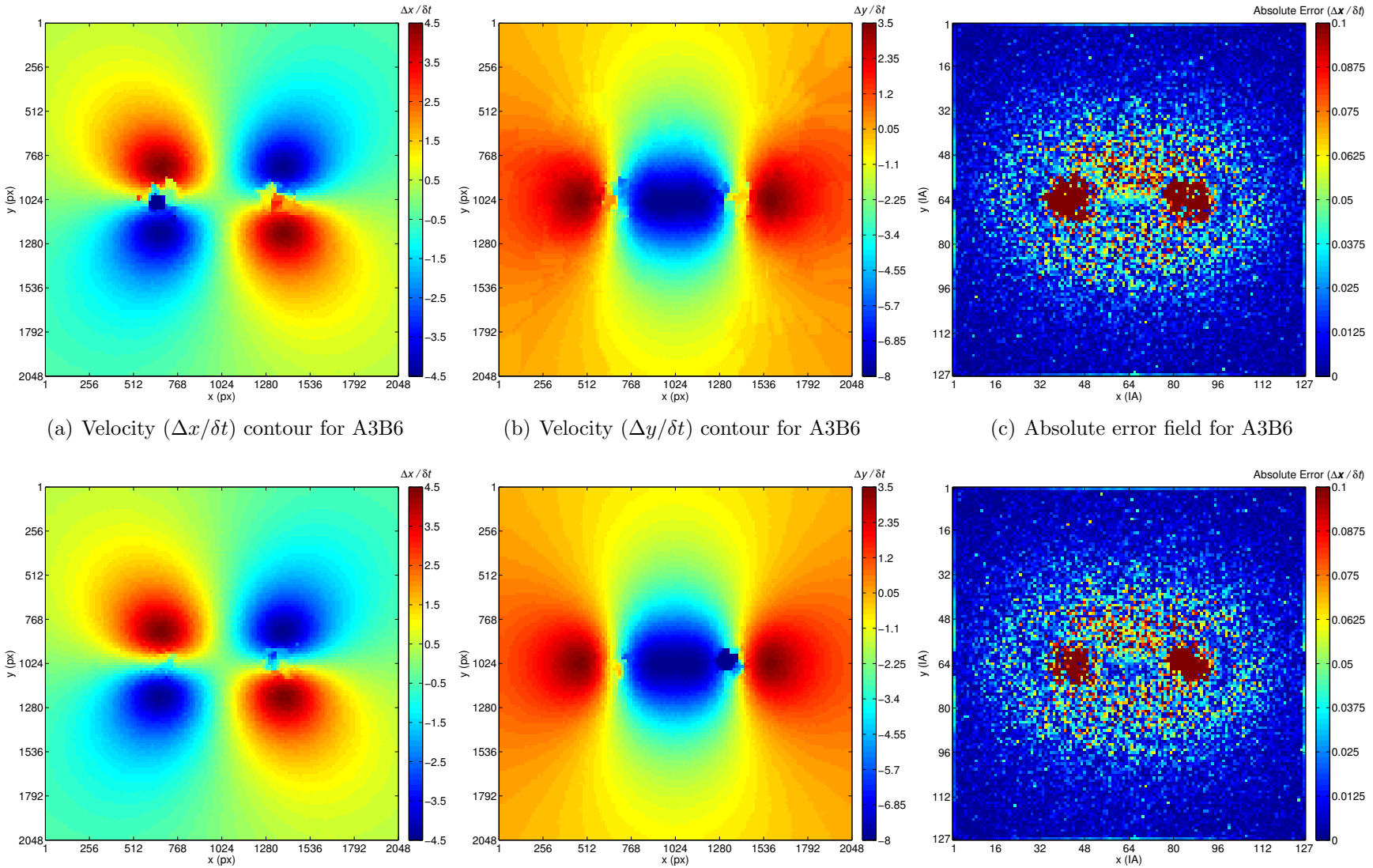

(a) Velocity ($\Delta x/\delta t$) contour for A3B6

(b) Velocity ($\Delta y/\delta t$) contour for A3B6

(c) Absolute error field for A3B6

(d) Velocity ($\Delta x/\delta t$) contour for A4B5

(e) Velocity ($\Delta y/\delta t$) contour for A4B5

(f) Absolute error field for A4B5

Figure D.3: Velocity field and absolute error results for the image pairs spanning $11\,\delta t$ (top) and $9\,\delta t$ (bottom).

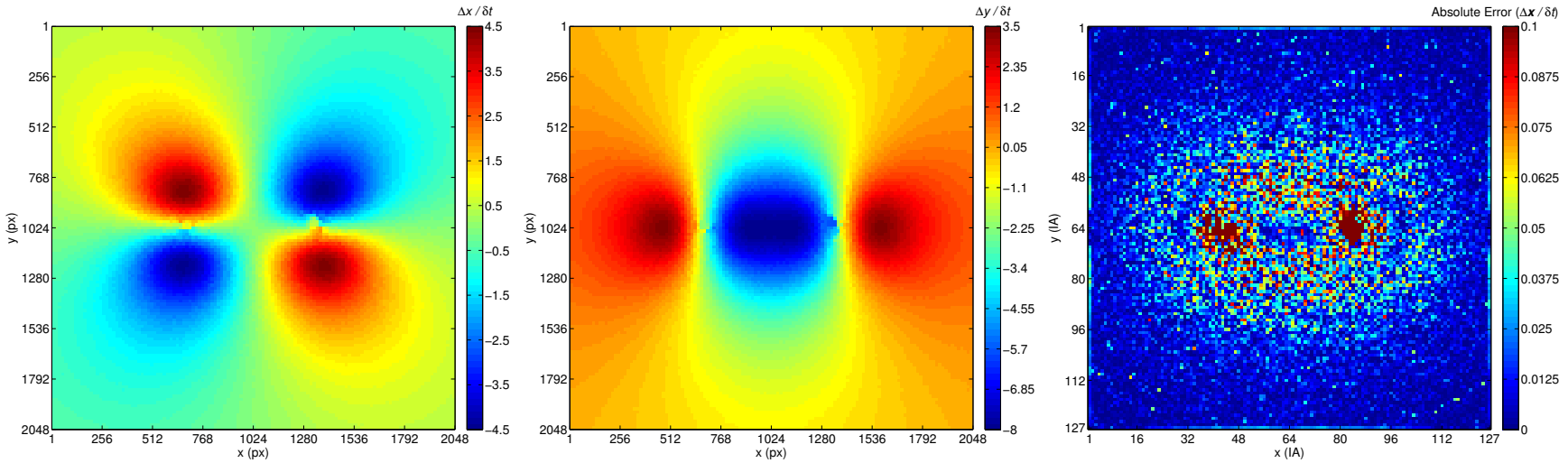

(a) Velocity ($\Delta x/\delta t$) contour for A5B4 (b) Velocity ($\Delta y/\delta t$) contour for A5B4 (c) Absolute error field for A5B4

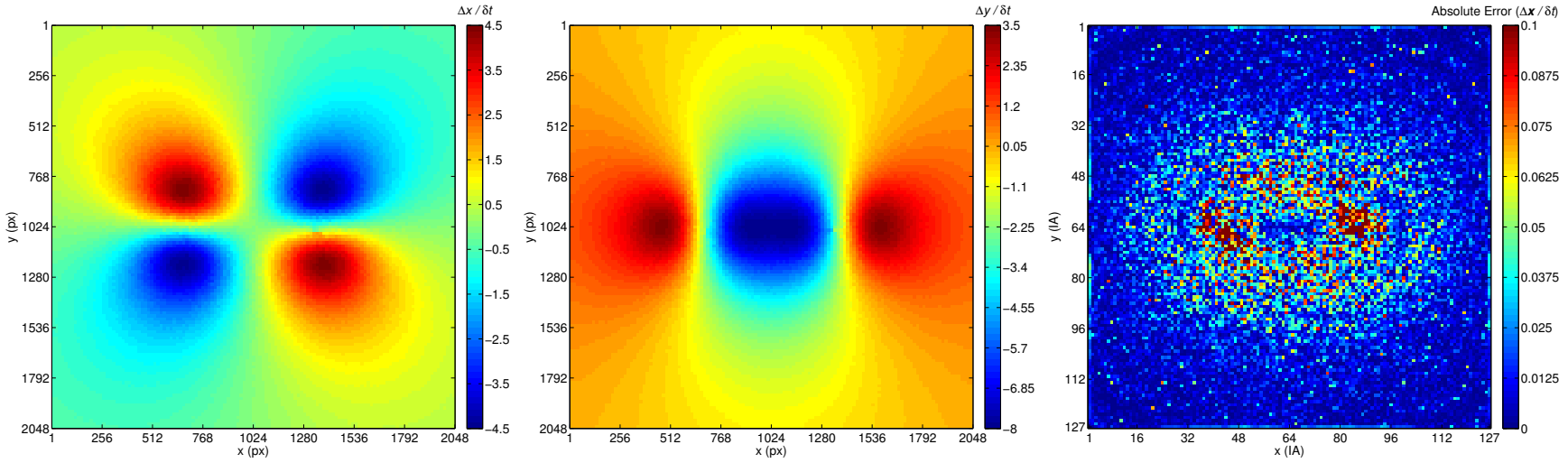

(d) Velocity ($\Delta x/\delta t$) contour for A6B3 (e) Velocity ($\Delta y/\delta t$) contour for A6B3 (f) Absolute error field for A6B3

Figure D.4: Velocity field and absolute error results for the image pairs spanning $7\,\delta t$ (top) and $5\,\delta t$ (bottom).

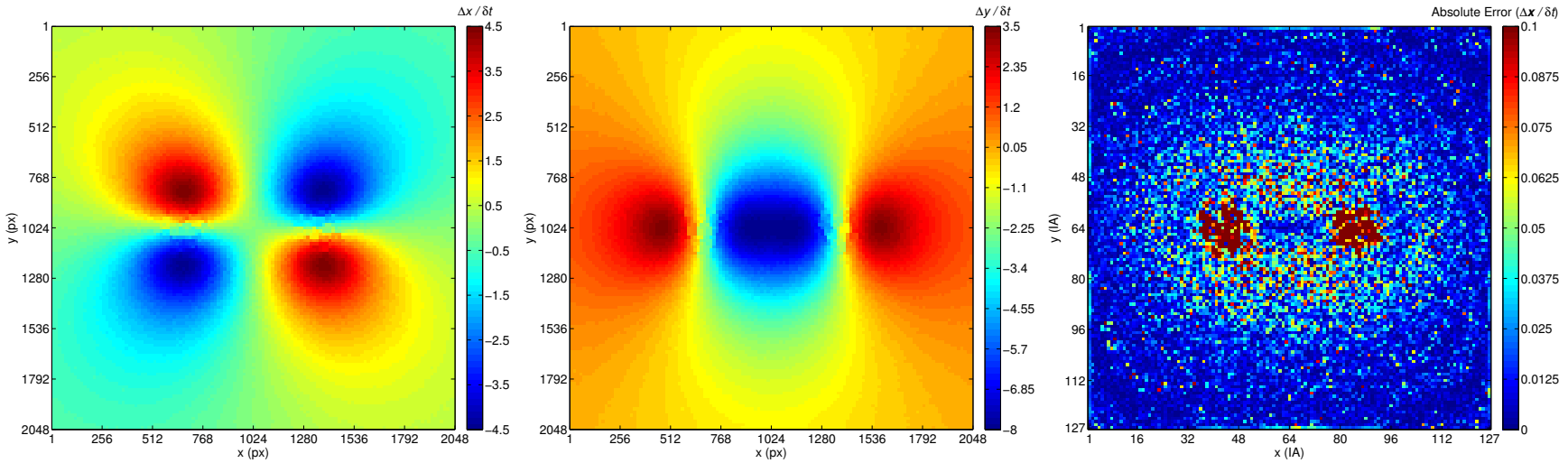

(a) Velocity ($\Delta x/\delta t$) contour for A7B2 (b) Velocity ($\Delta y/\delta t$) contour for A7B2 (c) Absolute error field for A7B2

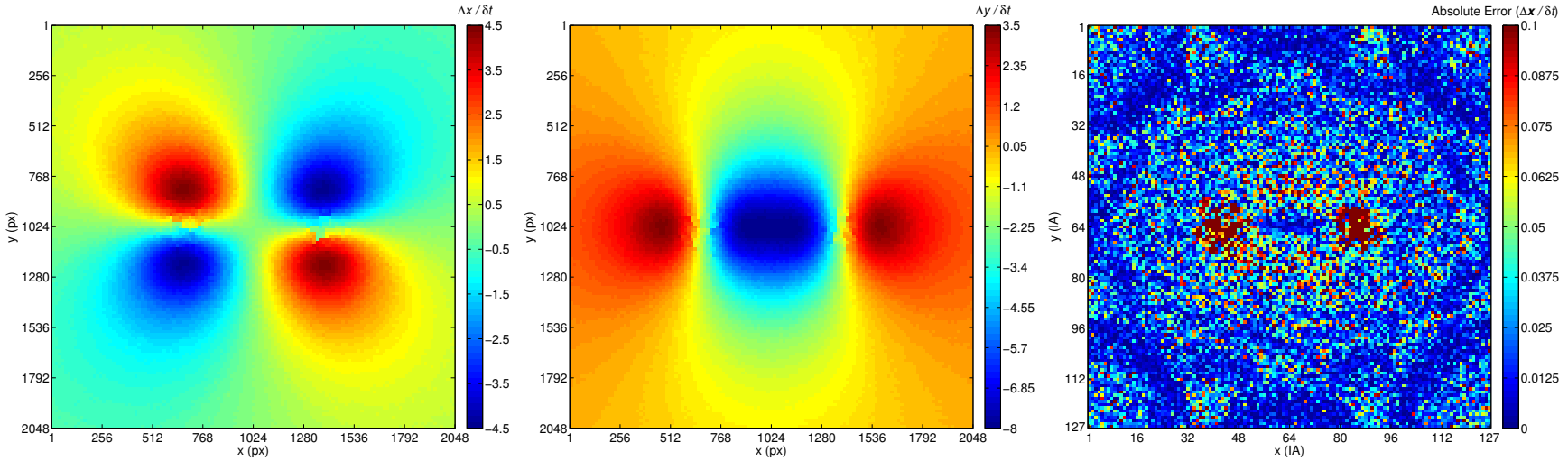

(d) Velocity ($\Delta x/\delta t$) contour for A8B1 (e) Velocity ($\Delta y/\delta t$) contour for A8B1 (f) Absolute error field for A8B1

Figure D.5: Velocity field and absolute error results for the image pairs spanning $3\,\delta t$ (top) and δt (bottom).

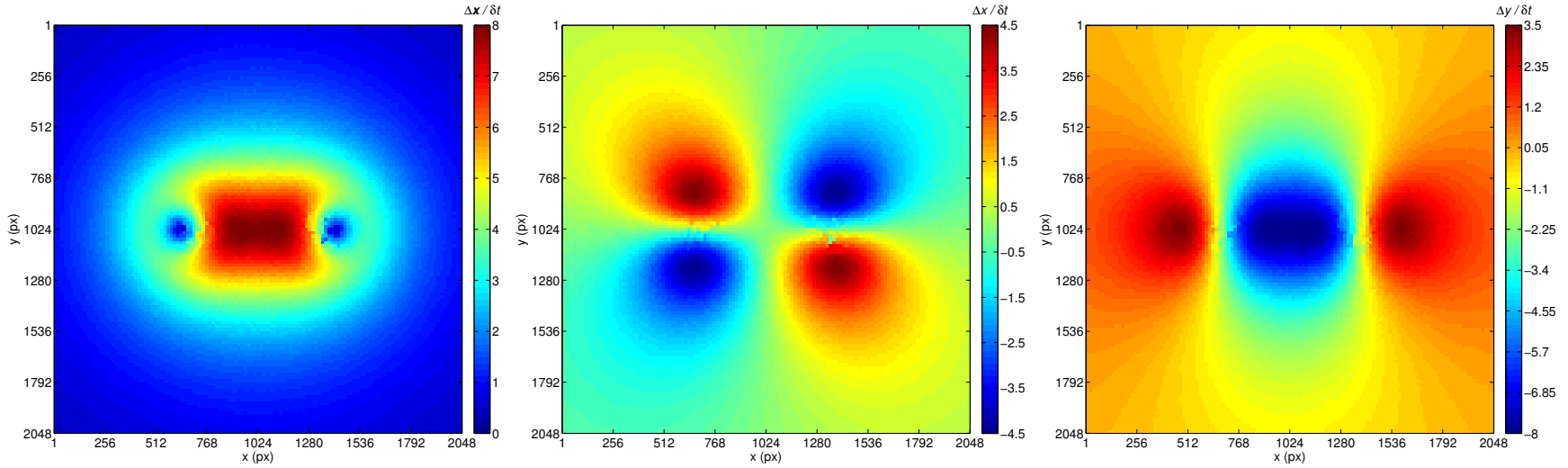

(a) Velocity magnitude for the HDR result (b) Velocity ($\Delta x/\delta t$) for the HDR result (c) Velocity ($\Delta y/\delta t$) for the HDR result

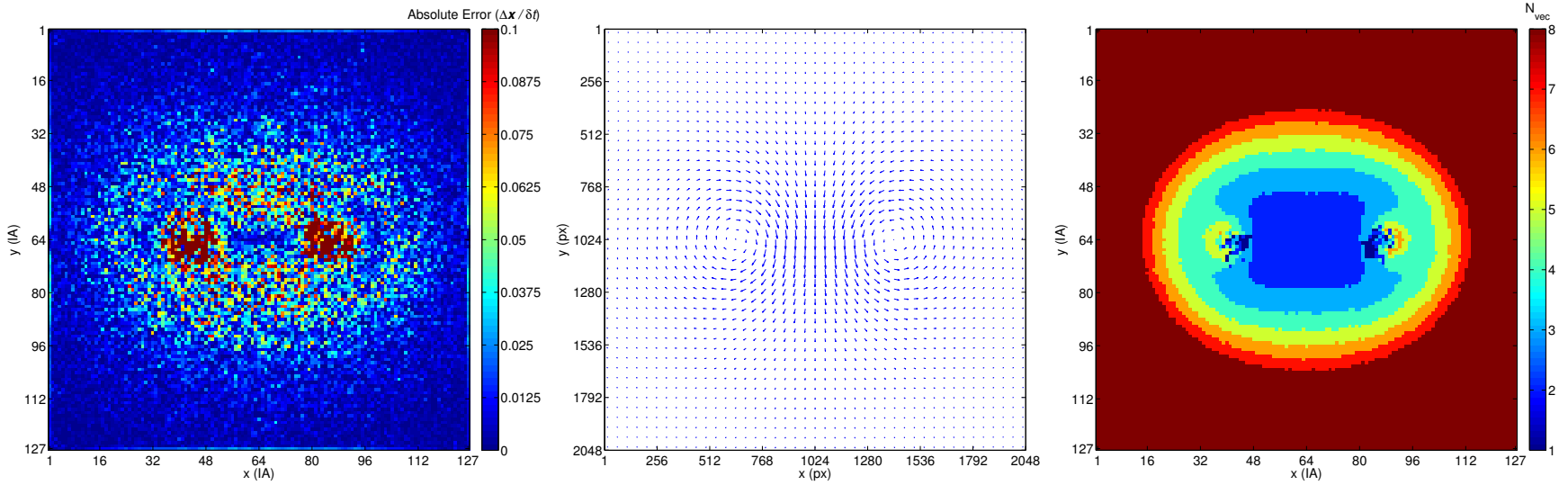

(d) Absolute error field for the HDR result (e) Vector plot for the HDR result (f) Vectors considered per spatial location

Figure D.6: HDR results for the synthetically generated Hamel-Oseen vortex pair.

Appendix E

Synthetic Jet Plots: Nozzle Exit

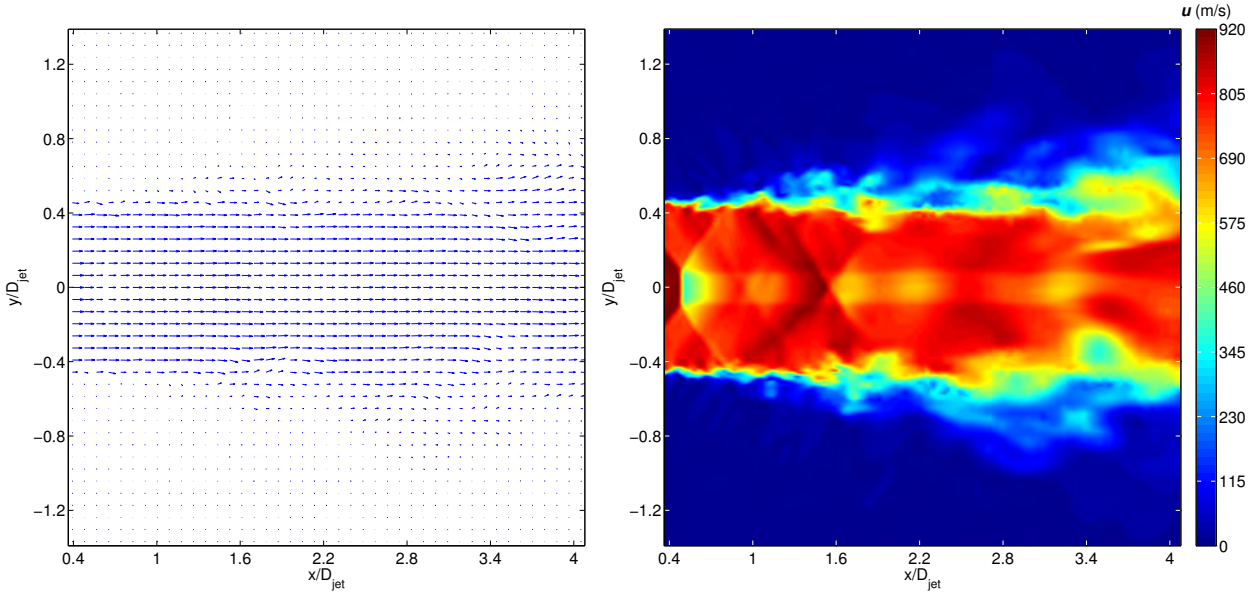

(a) Vector plot for the analytical solution

(b) Velocity magnitude for the analytical solution

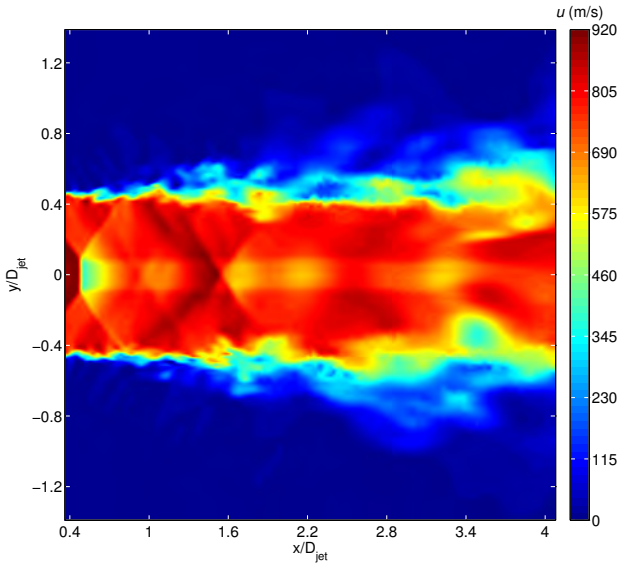

(c) Streamwise velocity for the analytical solution

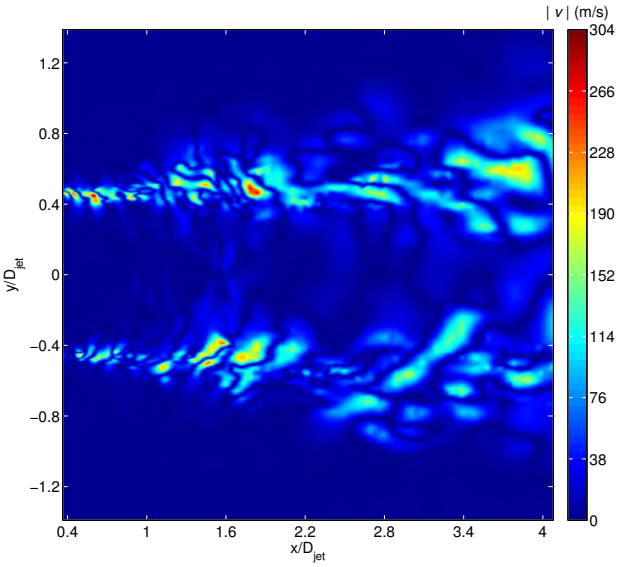

(d) Radial velocity for the analytical solution

Figure E.1: Analytical results for the nozzle exit region of the synthetically generated jet.

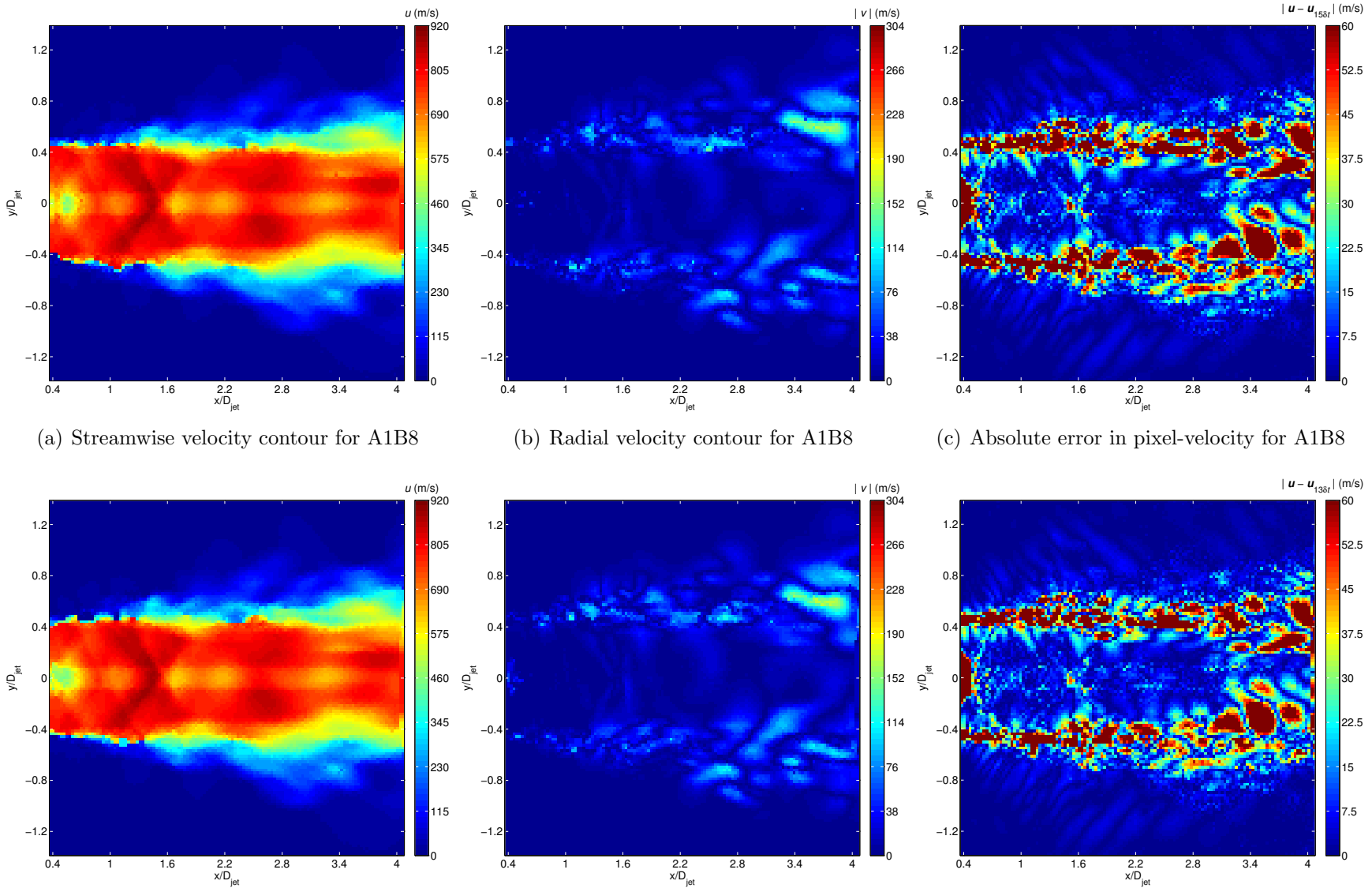

(a) Streamwise velocity contour for A1B8

(b) Radial velocity contour for A1B8

(c) Absolute error in pixel-velocity for A1B8

(d) Streamwise velocity contour for A2B7

(e) Radial velocity contour for A2B7

(f) Absolute error in pixel-velocity for A2B7

Figure E.2: Velocity field and absolute error results for the image pairs spanning $15\,\delta t$ (top) and $13\,\delta t$ (bottom).

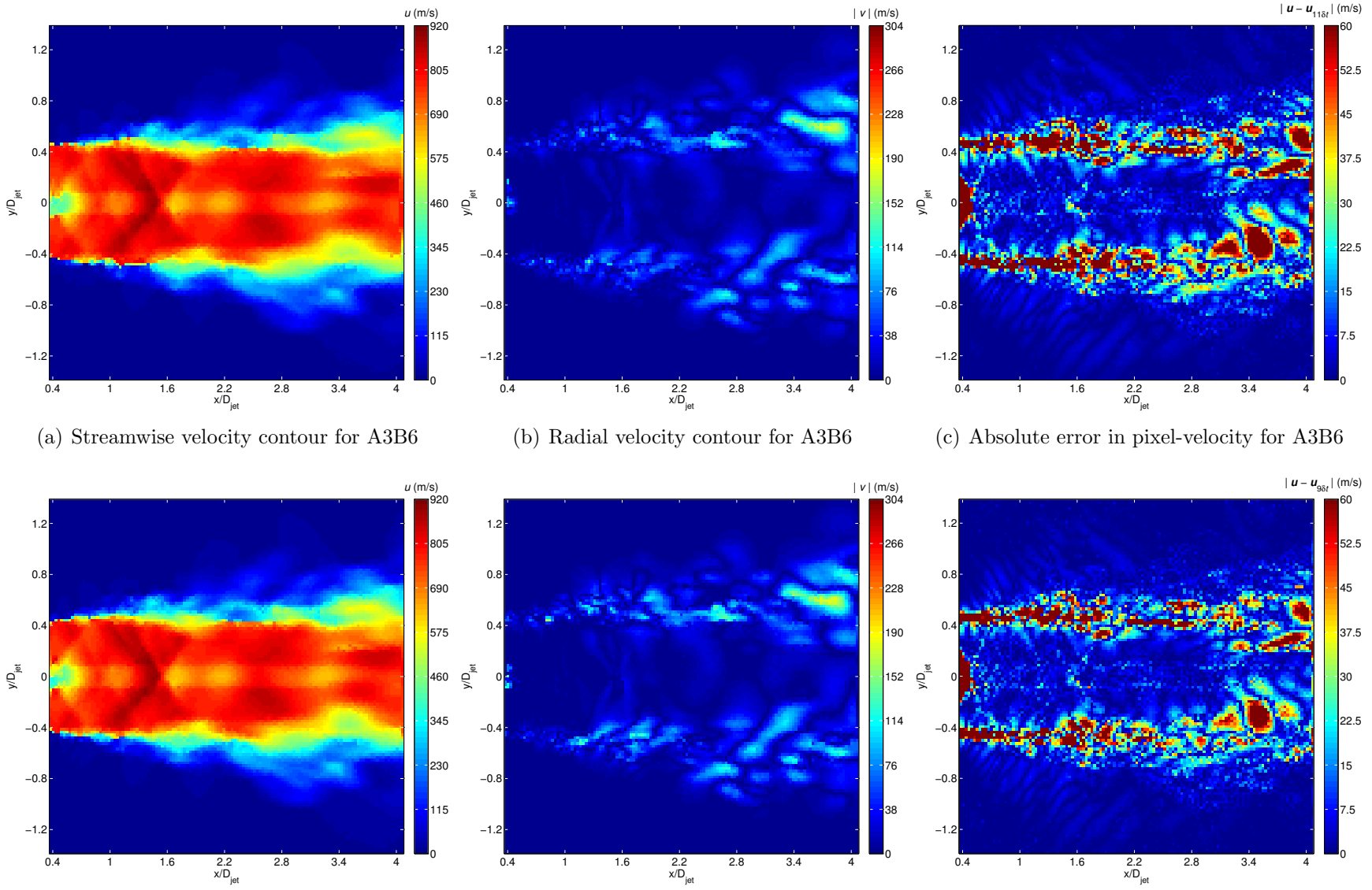

(a) Streamwise velocity contour for A3B6

(b) Radial velocity contour for A3B6

(c) Absolute error in pixel-velocity for A3B6

(d) Streamwise velocity contour for A4B5

(e) Radial velocity contour for A4B5

(f) Absolute error in pixel-velocity for A4B5

Figure E.3: Velocity field and absolute error results for the image pairs spanning 11 δt (top) and 9 δt (bottom).

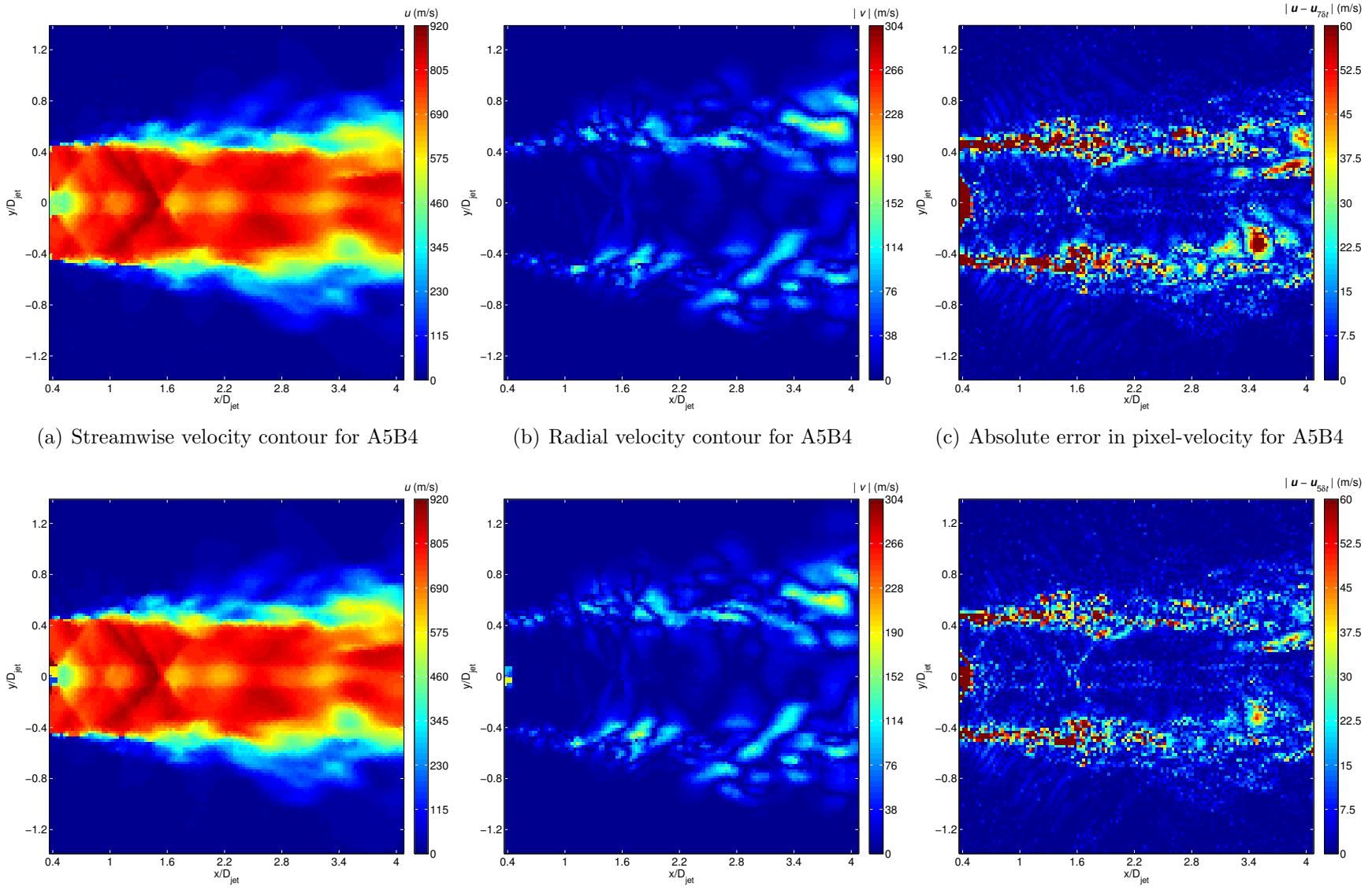

(a) Streamwise velocity contour for A5B4

(b) Radial velocity contour for A5B4

(c) Absolute error in pixel-velocity for A5B4

(d) Streamwise velocity contour for A6B3

(e) Radial velocity contour for A6B3

(f) Absolute error in pixel-velocity for A6B3

Figure E.4: Velocity field and absolute error results for the image pairs spanning $7\,\delta t$ (top) and $5\,\delta t$ (bottom).

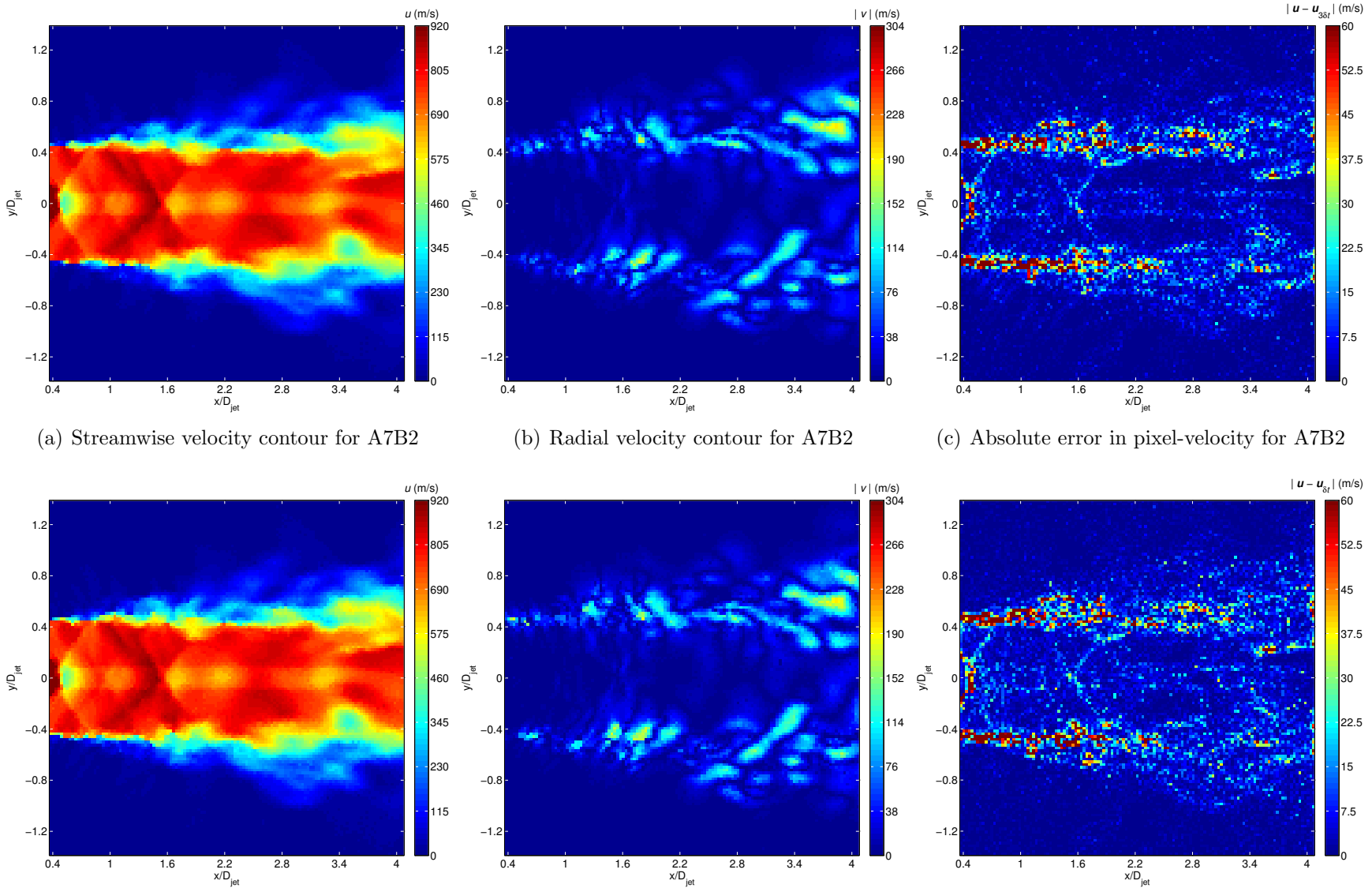

(a) Streamwise velocity contour for A7B2

(b) Radial velocity contour for A7B2

(c) Absolute error in pixel-velocity for A7B2

(d) Streamwise velocity contour for A8B1

(e) Radial velocity contour for A8B1

(f) Absolute error in pixel-velocity for A8B1

Figure E.5: Velocity field and absolute error results for the image pairs spanning $3\,\delta t$ (top) and δt (bottom).

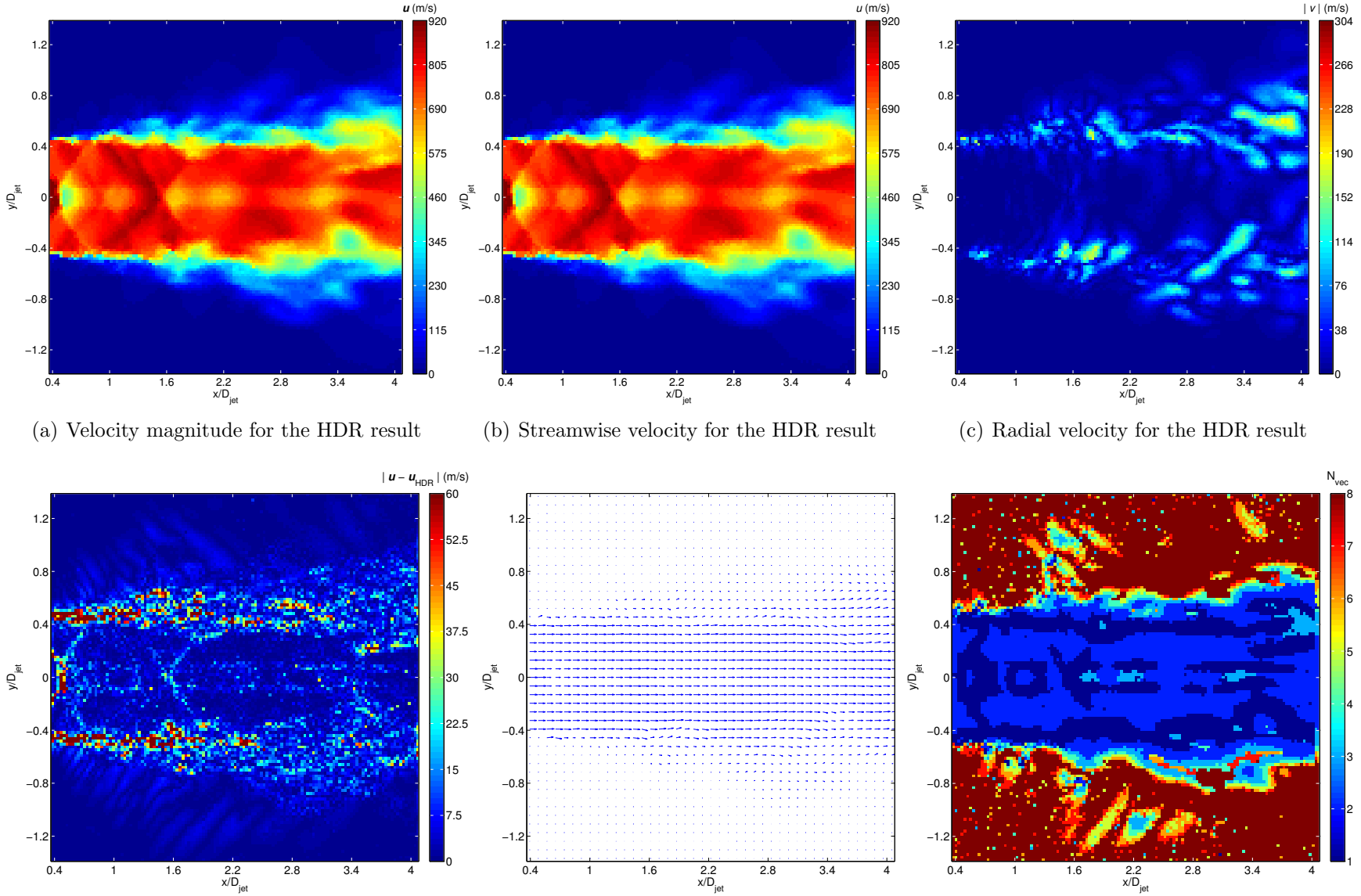

(a) Velocity magnitude for the HDR result

(b) Streamwise velocity for the HDR result

(c) Radial velocity for the HDR result

(d) Absolute error field for the HDR result

(e) Vector plot for the HDR result

(f) Vectors considered per spatial location

Figure E.6: HDR results for the nozzle exit region of the synthetically generated jet.

Appendix F

Synthetic Jet Plots: Potential Core Collapse

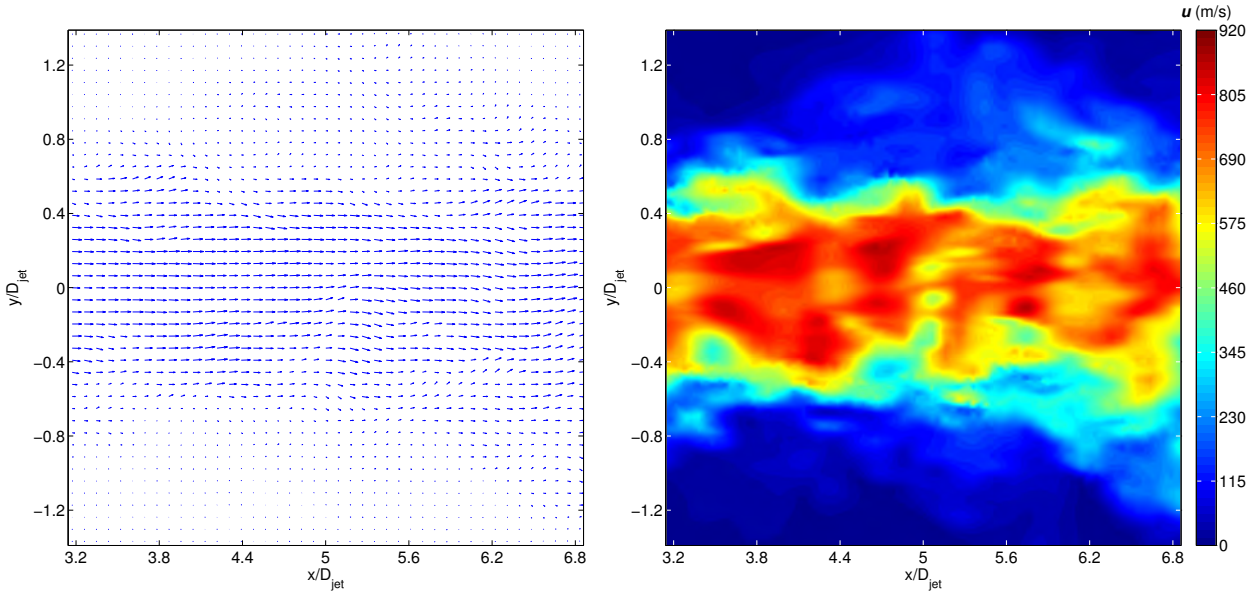

(a) Vector plot for the analytical solution

(b) Velocity magnitude for the analytical solution

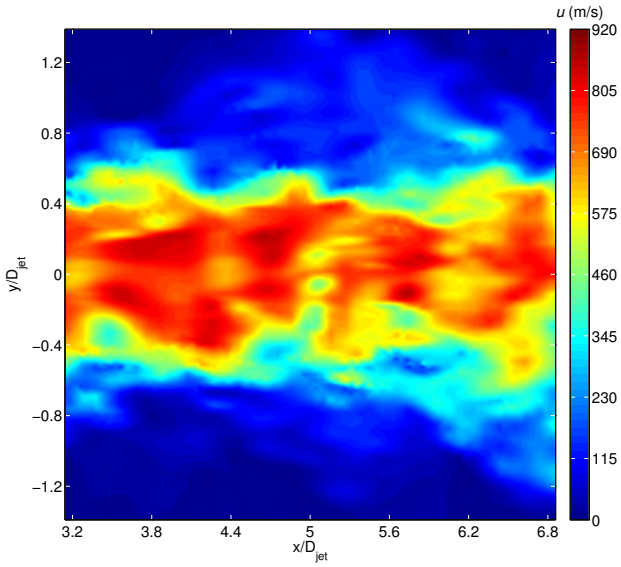

(c) Streamwise velocity for the analytical solution

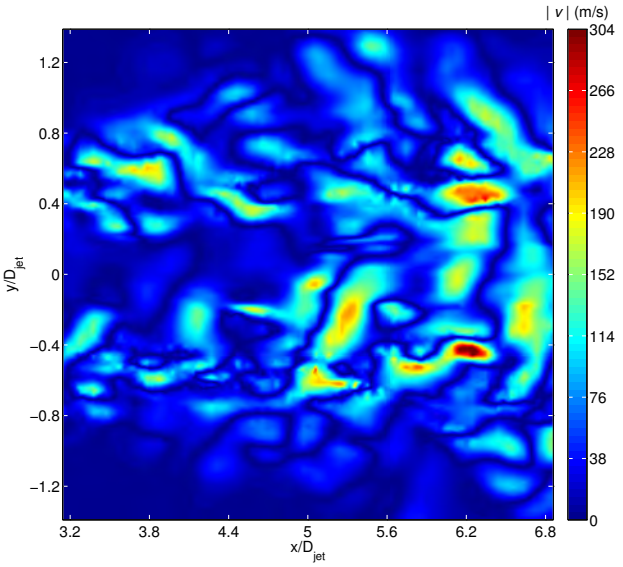

(d) Radial velocity for the analytical solution

Figure F.1: Analytical results for the potential core region of the synthetically generated jet.

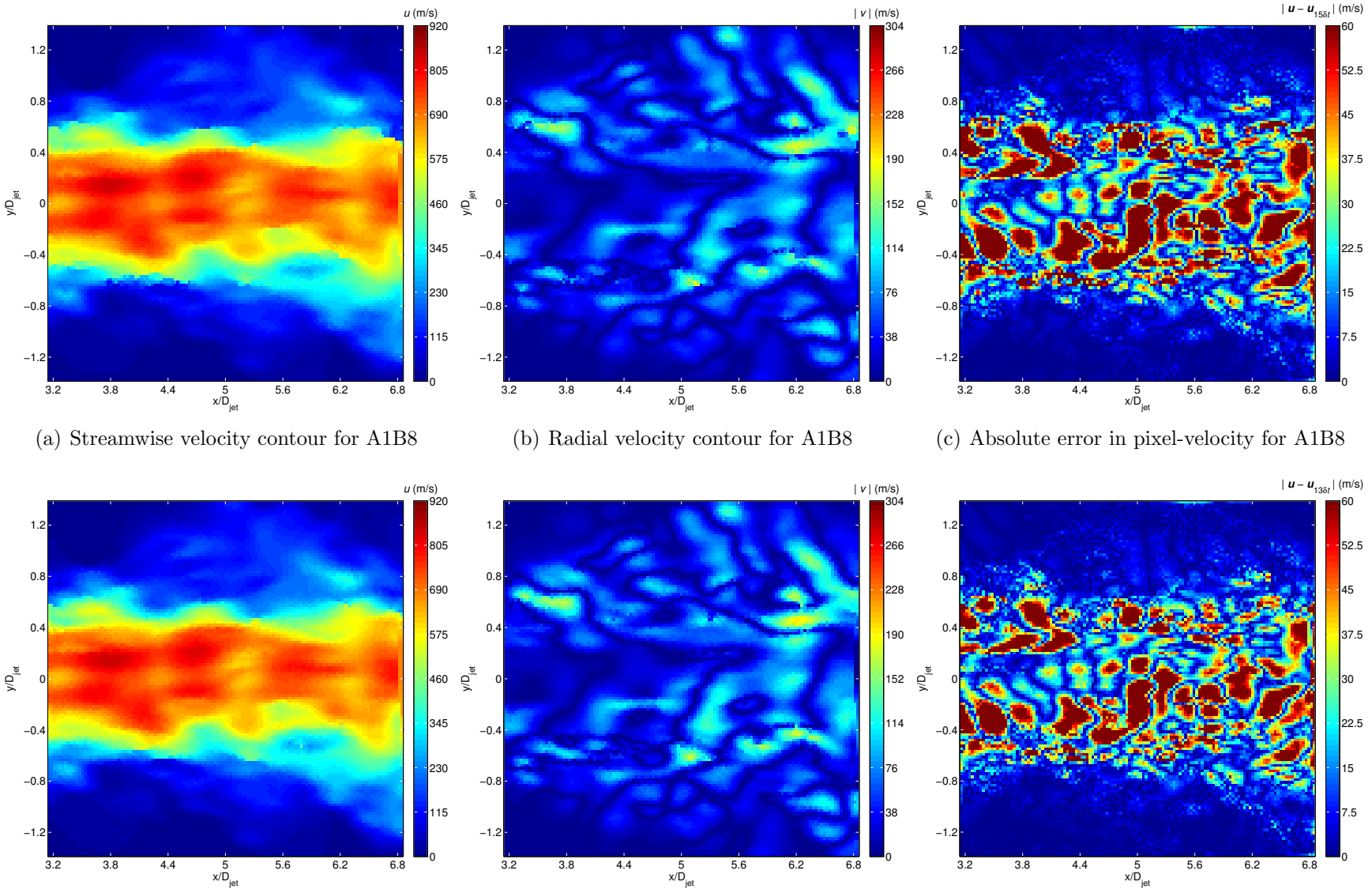

(a) Streamwise velocity contour for A1B8 (b) Radial velocity contour for A1B8 (c) Absolute error in pixel-velocity for A1B8

(d) Streamwise velocity contour for A2B7 (e) Radial velocity contour for A2B7 (f) Absolute error in pixel-velocity for A2B7

Figure F.2: Velocity field and absolute error results for the image pairs spanning $15\,\delta t$ (top) and $13\,\delta t$ (bottom).

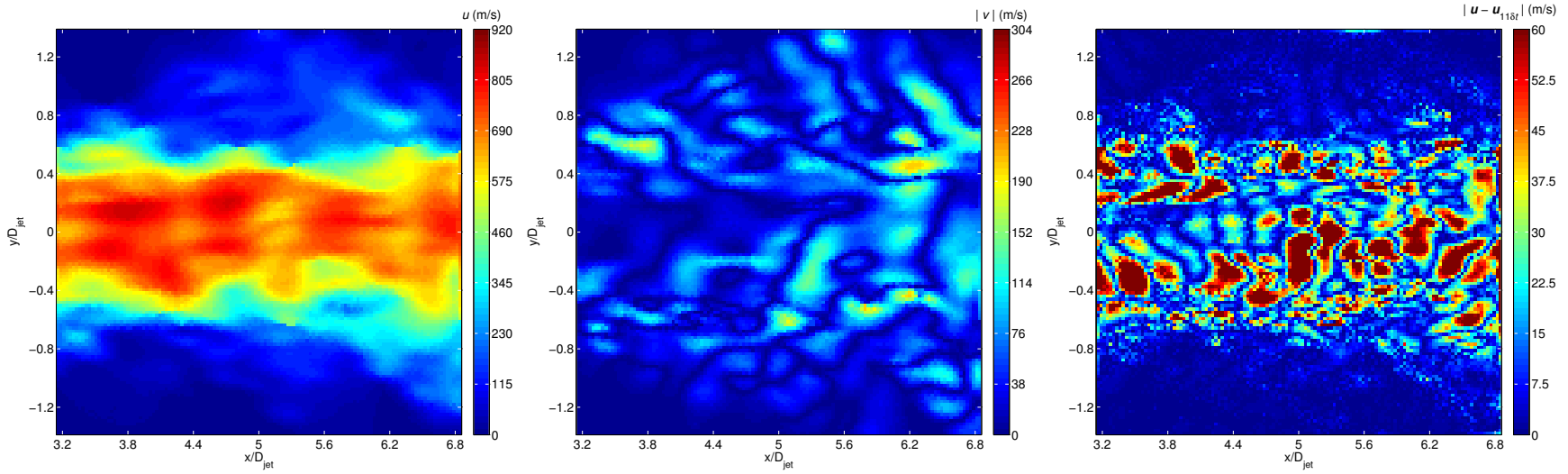

(a) Streamwise velocity contour for A3B6 (b) Radial velocity contour for A3B6 (c) Absolute error in pixel-velocity for A3B6

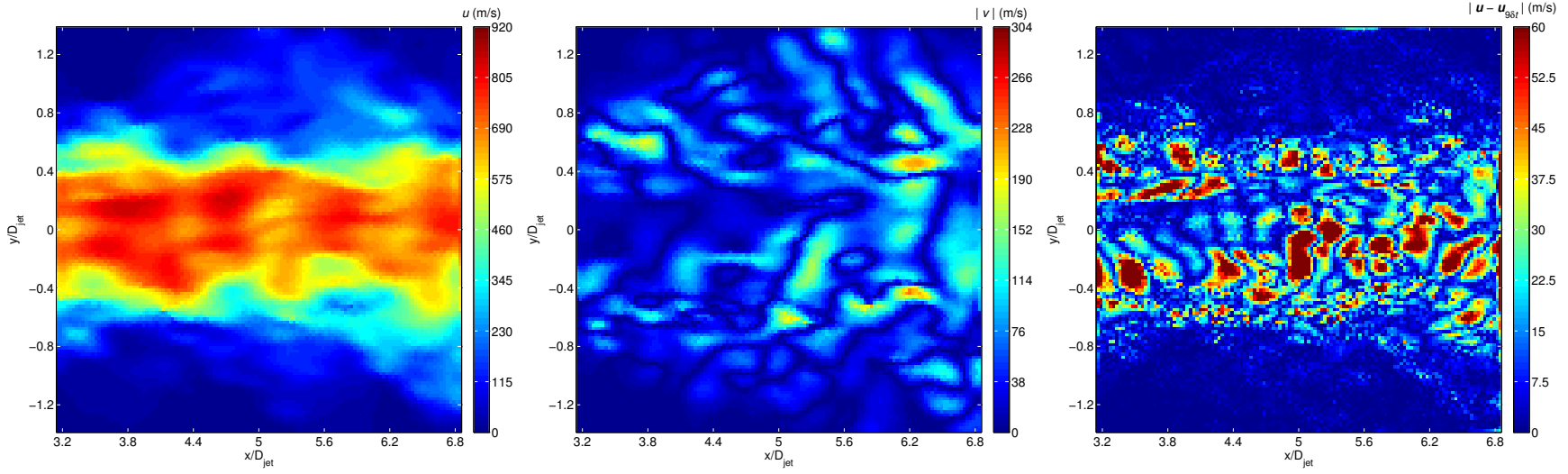

(d) Streamwise velocity contour for A4B5 (e) Radial velocity contour for A4B5 (f) Absolute error in pixel-velocity for A4B5

Figure F.3: Velocity field and absolute error results for the image pairs spanning 11 δt (top) and 9 δt (bottom).

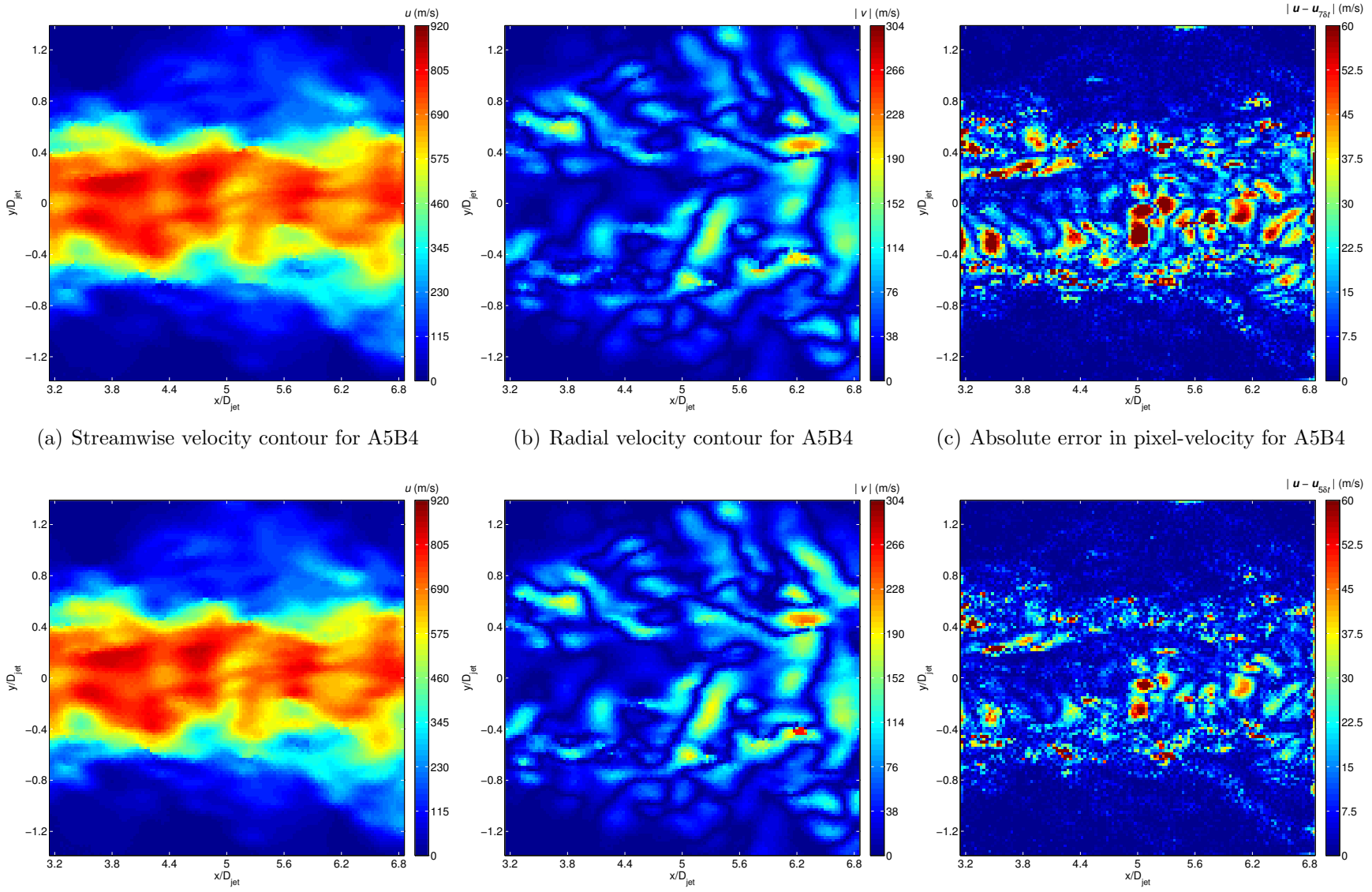

(a) Streamwise velocity contour for A5B4

(b) Radial velocity contour for A5B4

(c) Absolute error in pixel-velocity for A5B4

(d) Streamwise velocity contour for A6B3

(e) Radial velocity contour for A6B3

(f) Absolute error in pixel-velocity for A6B3

Figure F.4: Velocity field and absolute error results for the image pairs spanning $7\,\delta t$ (top) and $5\,\delta t$ (bottom).

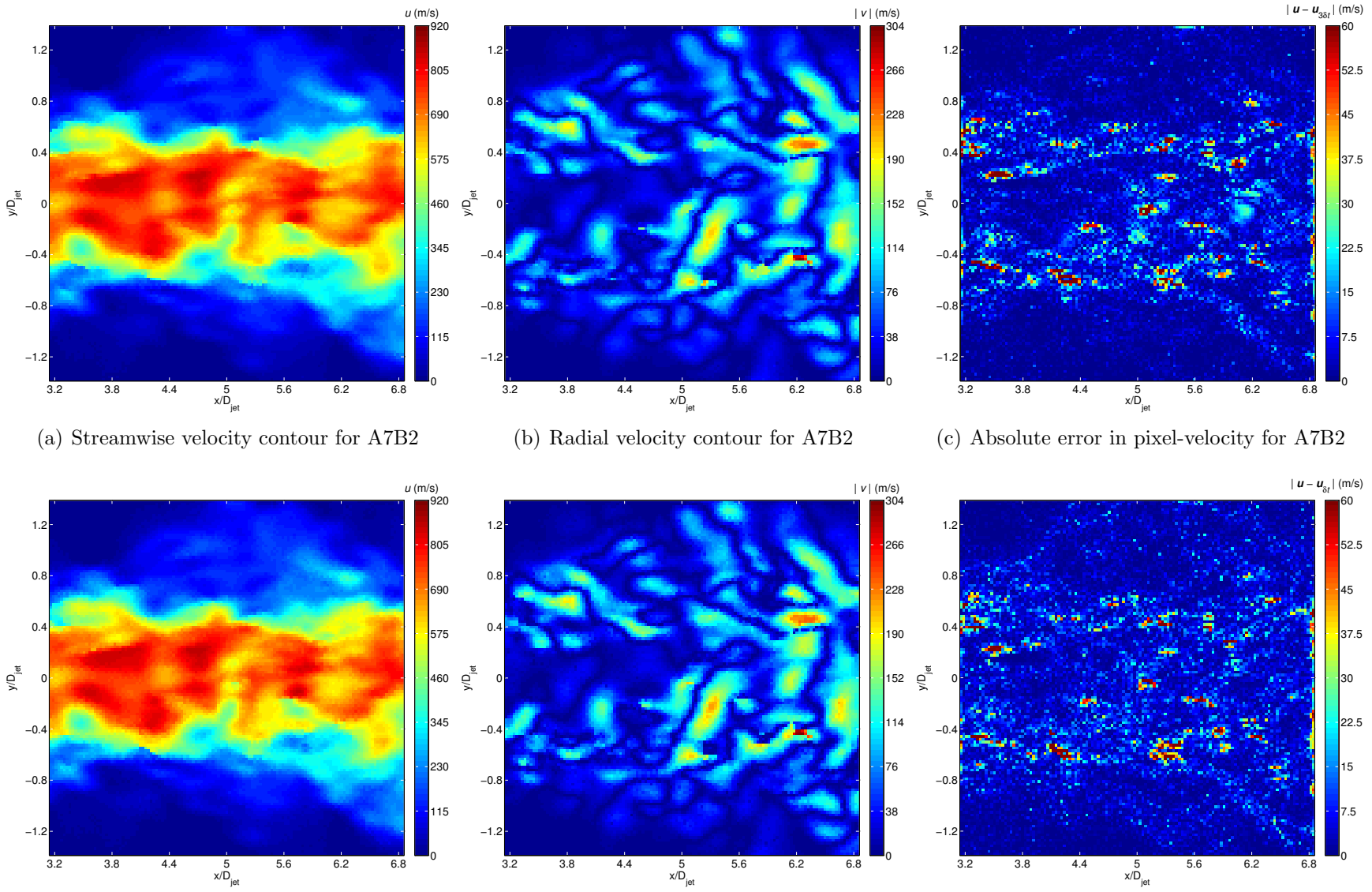

(a) Streamwise velocity contour for A7B2

(b) Radial velocity contour for A7B2

(c) Absolute error in pixel-velocity for A7B2

(d) Streamwise velocity contour for A8B1

(e) Radial velocity contour for A8B1

(f) Absolute error in pixel-velocity for A8B1

Figure F.5: Velocity field and absolute error results for the image pairs spanning $3\,\delta t$ (top) and δt (bottom).

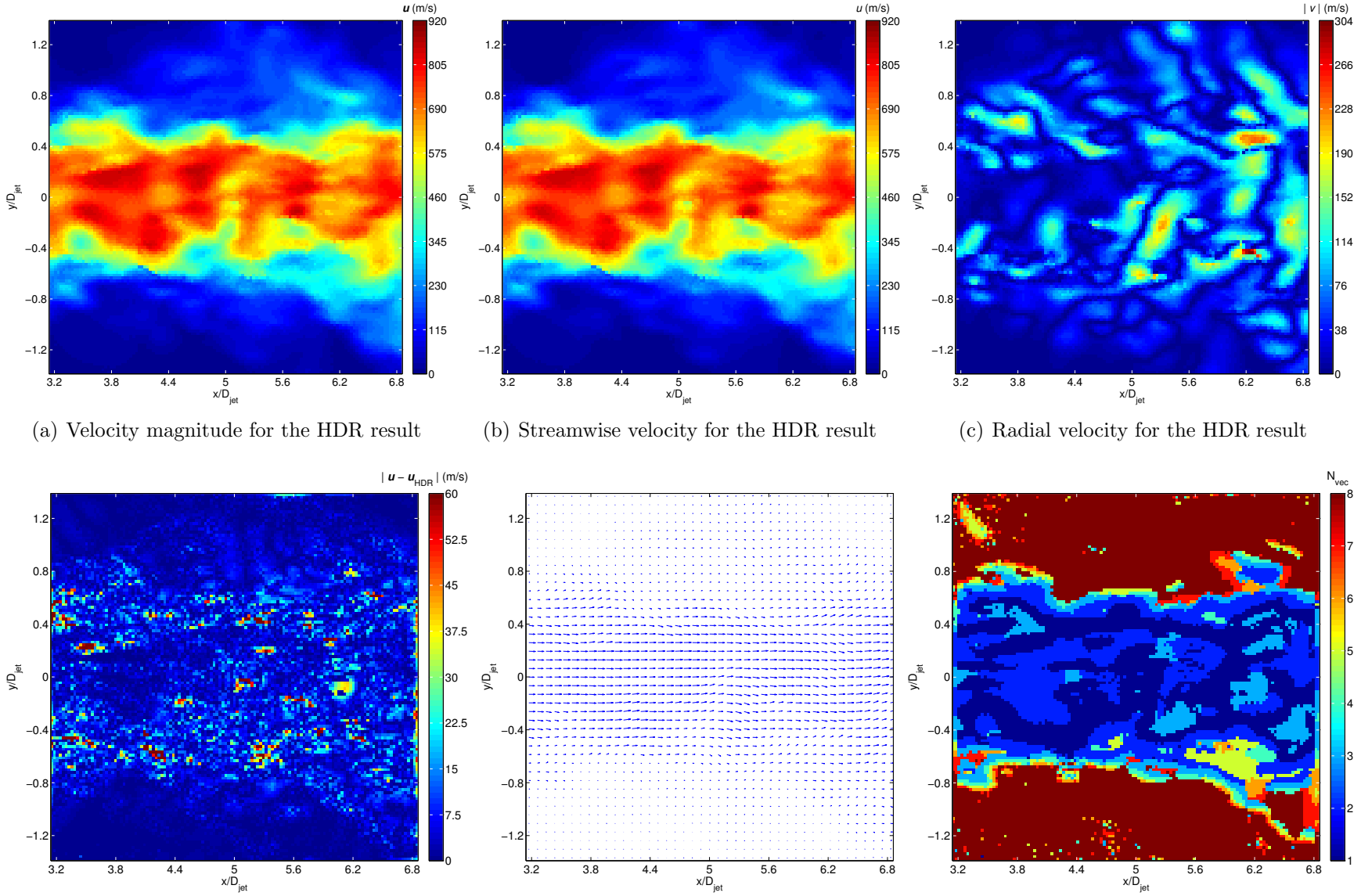

(a) Velocity magnitude for the HDR result

(b) Streamwise velocity for the HDR result

(c) Radial velocity for the HDR result

(d) Absolute error field for the HDR result

(e) Vector plot for the HDR result

(f) Vectors considered per spatial location

Figure F.6: HDR results for the potential core region of the synthetically generated jet.

Appendix G

Experimental Error Analysis Plots

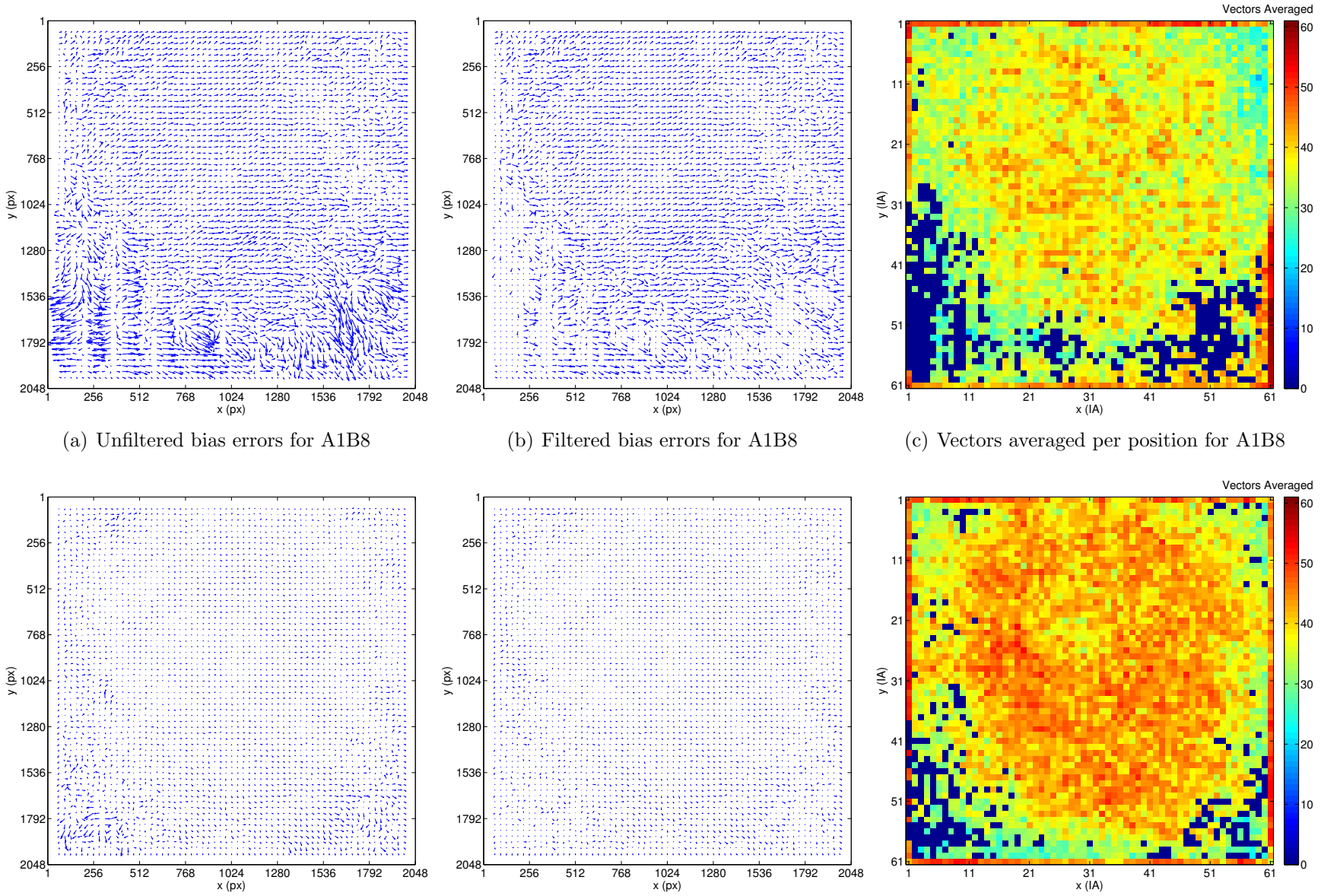

(a) Unfiltered bias errors for A1B8

(b) Filtered bias errors for A1B8

(c) Vectors averaged per position for A1B8

(d) Unfiltered bias errors for A2B7

(e) Filtered bias errors for A2B7

(f) Vectors averaged per position for A2B7

Figure G.1: Local bias error results for the image pairs spanning $15\,\delta t$ (top) and $13\,\delta t$ (bottom).

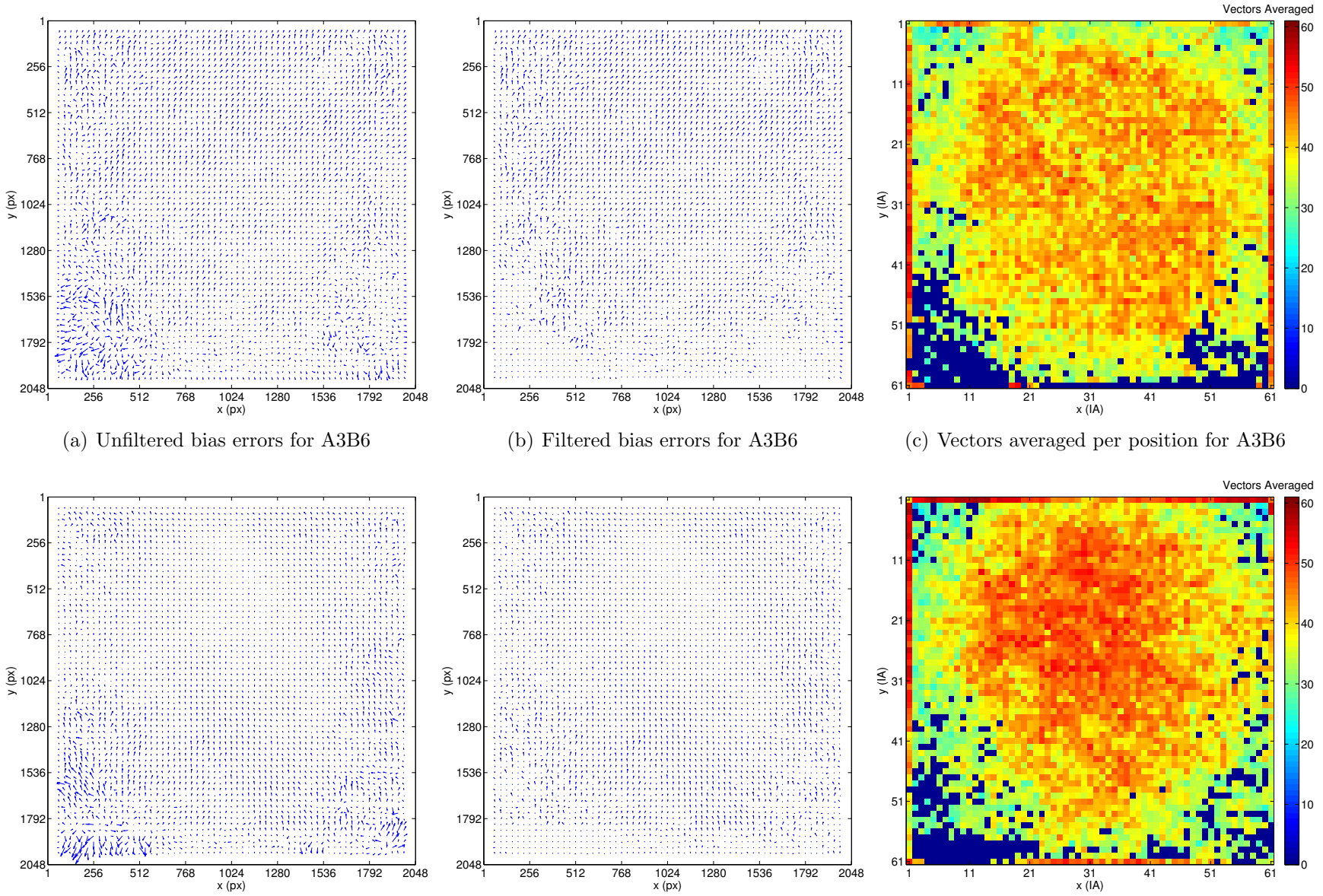

(a) Unfiltered bias errors for A3B6

(b) Filtered bias errors for A3B6

(c) Vectors averaged per position for A3B6

(d) Unfiltered bias errors for A4B5

(e) Filtered bias errors for A4B5

(f) Vectors averaged per position for A4B5

Figure G.2: Local bias error results for the image pairs spanning 11 δt (top) and 9 δt (bottom).

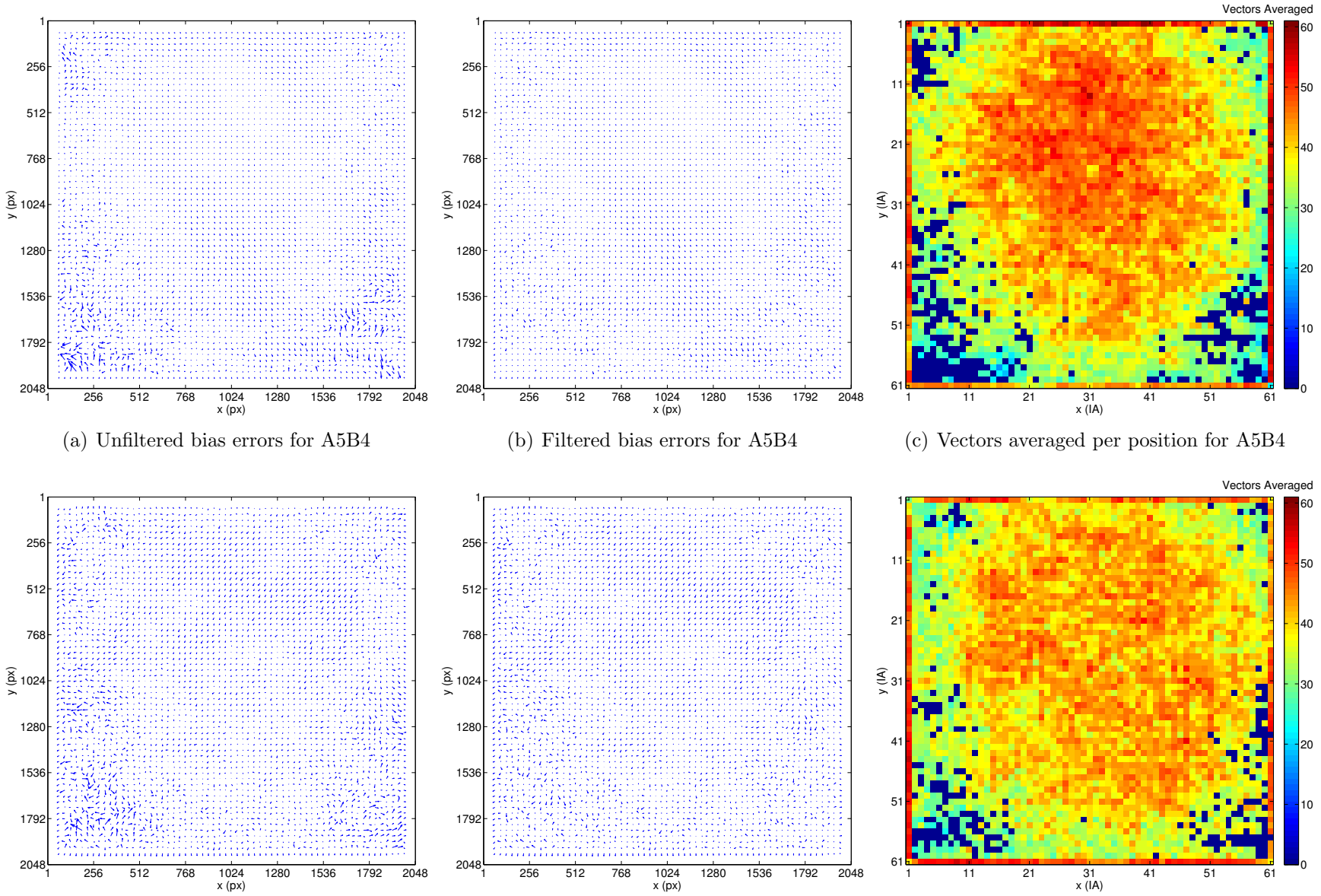

(a) Unfiltered bias errors for A5B4 (b) Filtered bias errors for A5B4 (c) Vectors averaged per position for A5B4

(d) Unfiltered bias errors for A6B3 (e) Filtered bias errors for A6B3 (f) Vectors averaged per position for A6B3

Figure G.3: Local bias error results for the image pairs spanning $7\,\delta t$ (top) and $5\,\delta t$ (bottom).

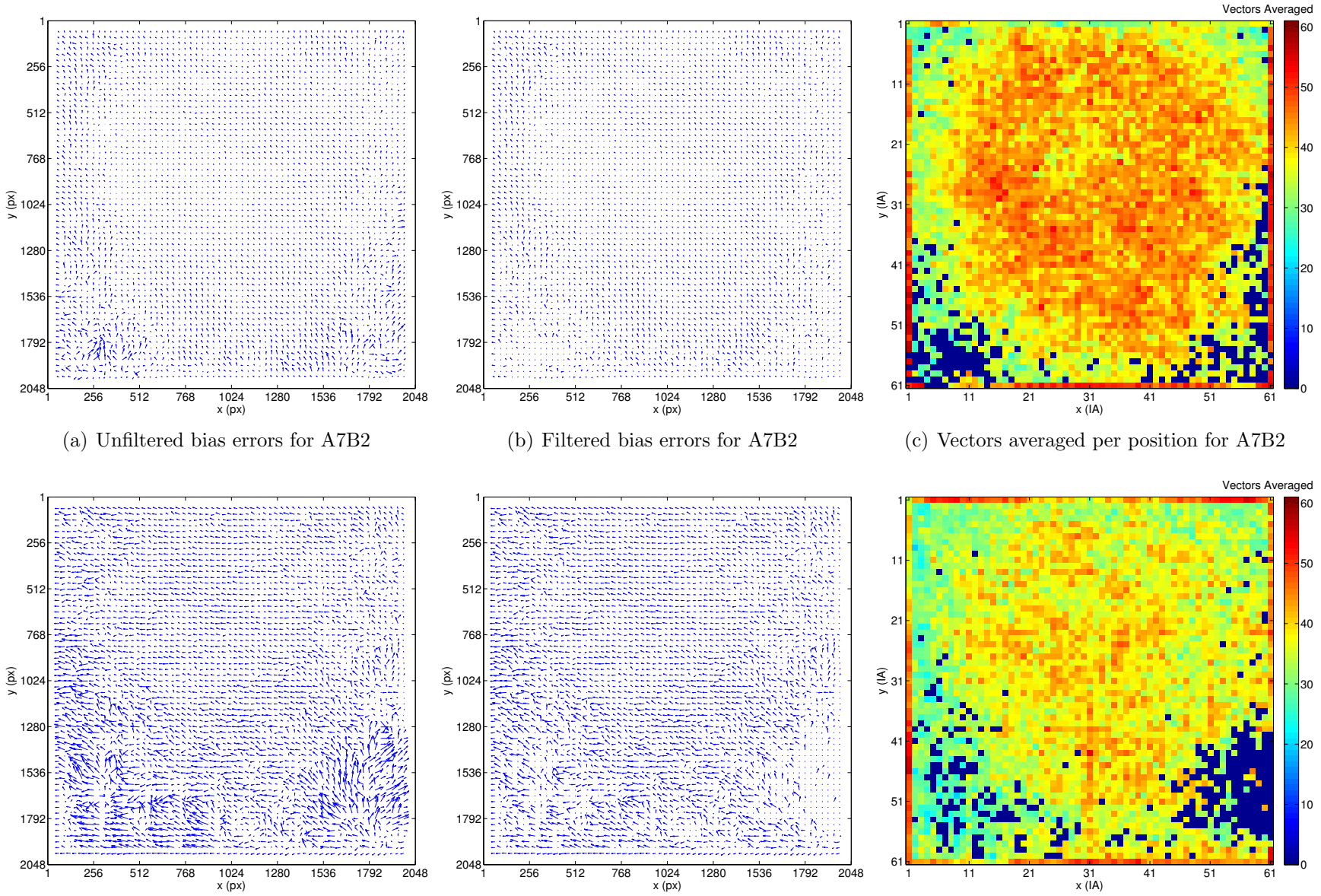

(a) Unfiltered bias errors for A7B2 (b) Filtered bias errors for A7B2 (c) Vectors averaged per position for A7B2

(d) Unfiltered bias errors for A8B1 (e) Filtered bias errors for A8B1 (f) Vectors averaged per position for A8B1

Figure G.4: Local bias error results for the image pairs spanning $3\,\delta t$ (top) and δt (bottom).